

# **An Experimental Study on the Entropy Generation during Fatigue of Fiber-Reinforced Thermoplastic Composites**

**Sara da Costa Pessoa**

Thesis to obtain the Master of Science Degree in

## **Aerospace Engineering**

Supervisors: Prof. Afzal Suleman  
Prof. Mehmet Yıldız

### **Examination Committee**

Chairperson: Prof. Filipe Szolnoky Ramos Pinto Cunha  
Supervisor: Prof. Afzal Suleman  
Member of the Committee: Prof. Aurélio Lima Araújo

**July 2022**



---

## Acknowledgments

Firstly, my words of gratitude are addressed to my supervisors, Prof. Dr. Afzal Suleman and Prof. Dr. Mehmet Yıldız, for the opportunity they provided and the support throughout this work. Their valuable insights and motivation allowed me to successfully complete my academic journey.

The financial and infrastructural support provided by Sabanci University - Integrated Manufacturing Technologies Research and Application Center, Sabanci University - Kordsa Composite Technologies Center of Excellence, and the individual research grant are greatly appreciated.

I would also like to express my immense gratitude to Ricardo Marques for his constant support from the very first day of this thesis until the last. I had the pleasure of working with someone who takes great pride in the correctness and critical thinking needed for a meaningful research work, and who always motivated me to do my best. Without all the effort he has put into this work, the patience and the never-ending zoom calls, the final outcome would definitely not be the same.

I am also thankful to all the PhD students, PostDocs and technicians working at SU-IMC who guided me through the world of experimental solid mechanics and provided help from the manufacturing process to the mechanical testing, sometimes even with a language barrier. My appreciation goes to Qasim Ali, Isa Tabrizi, Gökhan Inan, Pouya Yousefi, Bora Gönül and Aryan Kheyabani. *Çok teşekkür ederim*. Also, I cannot disregard the professional discussions and help with day-to-day life in Istanbul from Naqib Rahimi.

Lastly, a heartfelt thank you to all my friends and family who were always there for me throughout the last 6 years, without whom this journey would have not been possible.



## Resumo

A previsão de vida à fadiga é um tópico recorrente em engenharia devido à natureza catastrófica das falhas por fadiga. O surgimento de abordagens baseadas na geração de entropia constitui um avanço promissor em relação aos métodos mais convencionais de previsão, uma vez que permitem obter informação acerca dos fenómenos dissipativos presentes durante o carregamento cíclico de materiais. A entropia acumulada no momento de falha, entropia de fractura em fadiga (EFF), é descrita como sendo independente das condições de carregamento ou sequência de empilhamento. Contudo, os trabalhos existentes estão limitados a metais ou compósitos termoendurecíveis, e, no actual conhecimento da autora, a formulação de EFF ainda não foi estendida com sucesso a compósitos de matriz termoplástica.

Este trabalho apresenta um estudo sobre os efeitos da carga e frequência aplicada na entropia acumulada devido a deformação plástica e transferência de calor por condução durante fadiga, recorrendo à desigualdade de Clausius-Duhem. Testes de fadiga foram realizados em provetes de fibra de carbono/PEKK com configuração angular e quase-isotrópica, em quatro condições de carregamento (dois níveis de carga e duas frequências). Medições do campo de temperatura foram feitas com uma câmara térmica, enquanto o campo de deslocamento foi medido com um sistema de correlação digital de imagem de baixo custo.

Os resultados desta tese sugerem que, contrariamente à literatura relacionada, a EFF não é constante para todas as condições de carregamento, comprometendo assim a sua utilização como critério de falha para termoplásticos. Uma formulação teórica é proposta para considerar a influência de outros fenómenos dissipativos na entropia acumulada.

**Palavras-chave:** Materiais Compósitos Termoplásticos, Geração de Entropia, Previsão de Vida à Fadiga, Correlação Digital de Imagem.



## Abstract

Fatigue life prediction has always been a topic of interest in engineering due to the inherently catastrophic nature of fatigue failure. Entropy-based approaches started to emerge as a promising alternative to more conventional methods, where information about the dissipative phenomena encountered in cyclic loading of components is captured. The accumulated entropy at the time of failure, fracture fatigue entropy (FFE), is said to be independent of the loading condition or stacking sequence. However, existing works are limited to metals and thermoset-based composites, and to the best of the author's knowledge, the formulation of FFE has not yet been successfully extended to thermoplastic composites.

The present work delivers a study on the effects of stress and frequency in the accumulated generated entropy due to plastic deformation and heat flux by conduction during fatigue using the Clausius-Duhem inequality. Fatigue tests were conducted on carbon fiber/PEKK dog-bone specimens with angle-ply and quasi-isotropic configurations at four test conditions comprising two stress levels and two loading frequencies. Full-field temperature measurements were obtained using an infrared thermal camera, while full-field in-plane strains were measured with a "low-cost" digital image correlation system.

The results in this thesis suggest that, unlike the related literature, FFE is not constant across all loading conditions, thus compromising its usefulness as a failure criteria for thermoplastic composites. A theoretical formulation is proposed to account for the influence of other dissipative terms on the total accumulated entropy.

**Keywords:** Thermoplastic Composites, Entropy Generation, Fatigue Life Prediction, Digital Image Correlation.





# Contents

|  |           |
|--|-----------|
| Acknowledgments . . . . .  | iii       |
| Resumo . . . . .   | v         |
| Abstract . . . . .   | vii       |
| List of Tables . . . . .   | xi        |
| List of Figures . . . . .  | xiii      |
| Nomenclature . . . . .   | xv        |
| <b>1 Introduction</b>  | <b>1</b>  |
| 1.1 Thermoplastic Composites in Aerospace . . . . .                      | 1         |
| 1.2 The Fatigue Problem . . . . .  | 2         |
| 1.2.1 Frequency and Temperature Effects . . . . .                        | 2         |
| 1.3 Entropy as a Failure Criterion . . . . .                             | 3         |
| 1.4 Motivation and Objectives . . . . .                                  | 5         |
| 1.5 Thesis Outline . . . . .   | 6         |
| <b>2 Theoretical Background</b>  | <b>7</b>  |
| 2.1 Introduction . . . . .   | 7         |
| 2.2 Kinematics of deformation . . . . .                                  | 8         |
| 2.2.1 Finite deformations . . . . .                                      | 8         |
| 2.2.2 Infinitesimal viscoelastic deformations . . . . .                  | 9         |
| 2.2.3 Infinitesimal viscoelastic and viscoplastic deformations . . . . . | 9         |
| 2.3 Thermodynamic balance laws of continuum mechanics . . . . .          | 10        |
| 2.3.1 Balance of energy . . . . .  | 10        |
| 2.3.2 Balance of mechanical energy . . . . .                             | 10        |
| 2.3.3 Balance of thermal energy . . . . .                                | 10        |
| 2.3.4 Second law of thermodynamics . . . . .                             | 11        |
| 2.4 Helmholtz Free Energy . . . . .                                      | 12        |
| 2.4.1 Restrictions to constitutive laws . . . . .                        | 12        |
| 2.4.2 Application to the dissipation inequality . . . . .                | 13        |
| <b>3 Manufacture and Material Characterization</b>                       | <b>17</b> |
| 3.1 Material Description . . . . .                                       | 17        |

|          |   |           |
|----------|---|-----------|
| 3.2      | Composite Plate Manufacturing . . . . .         | 17        |
| 3.2.1    | Automated Fiber Placement . . . . .             | 18        |
| 3.2.2    | Autoclave . . . . .                             | 19        |
| 3.2.3    | Abrasive water jet machining . . . . .          | 20        |
| 3.3      | Material Characterization . . . . .             | 21        |
| 3.3.1    | Thermal Conductivity . . . . .                  | 21        |
| 3.3.2    | Emissivity . . . . .                            | 22        |
| 3.3.3    | Static Mechanical Properties . . . . .          | 27        |
| 3.3.4    | Preliminary fatigue life tests . . . . .        | 27        |
| <b>4</b> | <b>Methodology</b>                              | <b>31</b> |
| 4.1      | Experimental setup . . . . .                    | 31        |
| 4.1.1    | Digital Image Correlation . . . . .             | 31        |
| 4.1.2    | Thermal camera . . . . .                        | 34        |
| 4.1.3    | Servo-hydraulic machine . . . . .               | 35        |
| 4.2      | Test procedure . . . . .                        | 36        |
| 4.2.1    | Load levels and frequencies . . . . .           | 36        |
| 4.2.2    | Intervals for data acquisition . . . . .        | 36        |
| 4.3      | Data processing procedure . . . . .             | 37        |
| <b>5</b> | <b>Results and Discussion</b>                   | <b>39</b> |
| 5.1      | Angle-ply . . . . .                             | 39        |
| 5.1.1    | Fatigue Behavior . . . . .                      | 39        |
| 5.1.2    | Hysteresis Entropy . . . . .                    | 44        |
| 5.1.3    | Thermal Dissipation Entropy . . . . .           | 45        |
| 5.1.4    | Accumulated Entropy . . . . .                   | 46        |
| 5.1.5    | Infinitesimal vs Finite Strain Theory . . . . . | 47        |
| 5.2      | Quasi-isotropic . . . . .                       | 49        |
| 5.2.1    | Fatigue Behavior . . . . .                      | 49        |
| 5.2.2    | Hysteresis Entropy . . . . .                    | 50        |
| 5.2.3    | Thermal Dissipation Entropy . . . . .           | 53        |
| 5.2.4    | Accumulated Entropy . . . . .                   | 53        |
| 5.3      | Entropy as a failure criterion . . . . .        | 55        |
| <b>6</b> | <b>Conclusions</b>                              | <b>61</b> |
| 6.1      | Achievements . . . . .                          | 61        |
| 6.2      | Future Work . . . . .                           | 62        |
|          | <b>Bibliography</b>                             | <b>63</b> |

# List of Tables

|     |  |    |
|-----|--|----|
| 3.1 | Physical properties of TC1320 [38]. . . . .                        | 17 |
| 3.2 | Process parameters for the manufactured plates. . . . .            | 19 |
| 3.3 | Process parameters for the abrasive water jet machining. . . . .   | 21 |
| 3.4 | Thermal conductivity results. . . . .                              | 22 |
| 3.5 | Results of the emissivity tests. . . . .                           | 26 |
| 3.6 | Static tensile properties of AP and QI specimens. . . . .          | 27 |
| 3.7 | Fatigue loading conditions for the AP laminate. . . . .            | 29 |
| 3.8 | Fatigue loading conditions for the QI laminate. . . . .            | 29 |
| 4.1 | DIC parameters. . . . .  | 33 |
| 4.2 | Fatigue loading conditions for the AP and QI laminates. . . . .    | 36 |
| 5.1 | Fibers orientation after fatigue. . . . .                          | 40 |
| 5.2 | FFE and fatigue life of AP specimens. . . . .                      | 46 |
| 5.3 | FFE calculated with infinitesimal vs finite strain theory. . . . . | 49 |
| 5.4 | FFE and fatigue life of QI specimens. . . . .                      | 54 |



# List of Figures

|      |  |    |
|------|--|----|
| 2.1  | Schematic representation of different body configurations, respective system of axes and deformation gradients . . . . . | 7  |
| 3.1  | AFP system. . . . .  | 18 |
| 3.2  | Composite plates manufactured using AFP. . . . .   | 19 |
| 3.3  | Setup for autoclave consolidation. . . . .   | 20 |
| 3.4  | Autoclave processing cycle for consolidation of carbon fiber/PEKK. . . . .   | 20 |
| 3.5  | Composite plates after consolidation in autoclave. . . . .   | 20 |
| 3.6  | Setup for the TPS method. . . . .  | 21 |
| 3.7  | Global and lamina coordinate systems. . . . .  | 22 |
| 3.8  | Specimen coated with different materials. . . . .  | 24 |
| 3.9  | Setup for the emissivity tests. . . . .  | 25 |
| 3.10 | Screenshot of the ResearchIR window for one measurement. . . . .   | 27 |
| 3.11 | Stress-strain curves of AP and QI specimens under static loading. . . . .  | 28 |
| 3.12 | Geometry and dimensions of the specimens used for mechanical testing. . . . .  | 29 |
| 4.1  | Fatigue tests experimental setup. . . . .  | 31 |
| 4.2  | Schematic of the DIC working principle. . . . .  | 32 |
| 4.3  | Strain measurement methods and their limitations. . . . .  | 33 |
| 4.4  | Schematic of the experimental DIC process. . . . .   | 34 |
| 4.5  | Time intervals for stress and strain data acquisition. . . . .   | 37 |
| 4.6  | Schematic representation of the experimental data processing. . . . .  | 37 |
| 5.1  | Post-mortem optical microscopy analysis in AP specimens. . . . .   | 40 |
| 5.2  | Mean strain evolution with normalized cycles for the different test conditions in AP specimens. . . . .                  | 41 |
| 5.3  | Hysteresis loops for the AP specimens (loops for the first 10 cycles and every 10 cycles are depicted). . . . .          | 42 |
| 5.4  | Hysteresis energy and temperature evolution for the AP specimens. . . . .  | 44 |
| 5.5  | Entropy generated due to hysteresis in AP specimens. . . . .   | 45 |
| 5.6  | Temperature profile of the AP_70%_10Hz case for $N/N_f=0.9$ . . . . .  | 45 |
| 5.7  | Entropy generated due to heat transfer for the AP_70%_10Hz case. . . . .   | 46 |

|      |   |    |
|------|---|----|
| 5.8  | Accumulated entropy through the cycles in AP specimens. . . . .   | 47 |
| 5.9  | Normalized accumulated entropy through the fatigue life in AP specimens. . . . .  | 48 |
| 5.10 | Time evolution of Green-Lagrange and engineering strain. . . . .  | 48 |
| 5.11 | Post-mortem optical microscopy analysis in QI specimens. . . . .  | 50 |
| 5.12 | Mean strain evolution for the different test conditions in QI specimens. . . . .  | 51 |
| 5.13 | Hysteresis loops for the QI specimens. . . . .  | 51 |
| 5.14 | Hysteresis energy and temperature evolution for the QI specimens. . . . .   | 52 |
| 5.15 | Entropy generated due to hysteresis in QI specimens. . . . .  | 52 |
| 5.16 | Temperature profile of the QI_95%_10Hz case for $N/N_f=0.9$ . . . . .   | 53 |
| 5.17 | Entropy generated due to heat transfer in the QI_95%_10Hz case. . . . .   | 53 |
| 5.18 | Accumulated entropy through the cycles in QI specimens. . . . .   | 54 |
| 5.19 | Normalized accumulated entropy through the fatigue life in QI specimens. . . . .  | 55 |
| 5.20 | FFE vs. fatigue life of the performed tests. . . . .  | 56 |
| 5.21 | FFE vs. fatigue life of the tests performed by Naderi and Khonsari [23]. . . . .  | 56 |
| 5.22 | Accumulated entropy through the cycles in QI specimens with (dashed line) and without<br>(solid line) the contribution of IF. . . . . | 58 |
| 5.23 | FFE vs. fatigue life of the tests performed by Huang et al. [29]. . . . .   | 59 |
| 5.24 | Fatigue modulus concept. . . . .  | 60 |
| 5.25 | Fatigue modulus evolution with cycles. . . . .  | 60 |

# Nomenclature

## Abbreviations

AFP Automated Fiber Placement.

AP Angle-Ply.

DIC Digital Image Correlation.

DSLR Digital Single-Lens Reflex.

FFE Fracture Fatigue Entropy.

FOV Field-of-view.

IF Internal Friction.

PEEK Polyetheretherketone.

PEKK Polyetherketoneketone.

PID Proportional-Integral-Derivative.

PMC Polymer Matrix Composite.

PPS Polyphenylene Sulfide.

QI Quasi-Isotropic.

RHS Right-hand Side.

ROI Region-of-Interest.

SD Standard Deviation.

SHM Structural Health Monitoring.

TP Thermoplastic.

TPS Transient Plane Source.

UD Unidirectional.

UTS Ultimate Tensile Strength.

## **Greek symbols**

|                 |   |
|-----------------|---|
| $\alpha$        | Kinematic hardening.  |
| $\beta$         | Fiber orientation angle.  |
| $\delta$        | Phase angle between stress and strain.                                |
| $\eta$          | Entropy per unit mass and unit volume.                                |
| $\Gamma$        | Viscoplastic Helmholtz free energy internal variables and parameters. |
| $\gamma$        | Generated entropy per unit mass and unit volume.                      |
| $\Lambda$       | Viscoelastic Helmholtz free energy internal variables and parameters. |
| $\psi$          | Helmholtz free energy.  |
| $\rho$          | Density.  |
| $\sigma$        | Infinitesimal stress.   |
| $\sigma_0$      | Infinitesimal stress amplitude.                                       |
| $\theta$        | Absolute temperature.   |
| $\varepsilon$   | Infinitesimal strain.   |
| $\varepsilon_0$ | Infinitesimal strain amplitude.                                       |

## **Roman symbols**

|          |                                      |
|----------|--------------------------------------|
| <b>b</b> | Internal body force per unit mass.   |
| <b>D</b> | Rate of deformation tensor.          |
| <b>E</b> | Green-Lagrange strain tensor.        |
| <b>e</b> | Eulerian strain tensor.              |
| <b>F</b> | Deformation gradient tensor.         |
| <b>H</b> | Displacement gradient tensor.        |
| <b>L</b> | Velocity gradient tensor.            |
| <b>P</b> | First Piola-Kirchoff stress tensor.  |
| <b>q</b> | Heat flux vector.                    |
| <b>S</b> | Second Piola-Kirchoff stress tensor. |
| <b>T</b> | Cauchy stress tensor.                |
| <b>t</b> | Traction vector.                     |



|              |                                |
|--------------|--------------------------------|
| $\mathbf{u}$ | Displacement vector.           |
| $\mathbf{v}$ | Material point's velocity.     |
| $D$          | Damage parameter.              |
| $e$          | Emissivity.                    |
| $F$          | Fatigue modulus.               |
| $f$          | Test frequency.                |
| $J$          | Jacobian-determinant.          |
| $k$          | Thermal conductivity.          |
| $N$          | Cycle number.                  |
| $N_f$        | Number of cycles to failure.   |
| $r$          | Heat supply per unit mass.     |
| $s$          | Material's past time.          |
| $t$          | Time.                          |
| $T_g$        | Glass transition temperature.  |
| $T_m$        | Melting temperature.           |
| $T_p$        | Processing temperature.        |
| $u$          | Internal energy per unit mass. |

### **Subscripts**

|           |                       |
|-----------|-----------------------|
| $x, y, z$ | Cartesian components. |
| L         | Longitudinal.         |
| T         | Transverse.           |
| ve        | Viscoelastic.         |
| vp        | Viscoplastic.         |

### **Superscripts**

|   |                            |
|---|----------------------------|
| T | Transpose.                 |
| t | Material's time histories. |



# Chapter 1

## Introduction

### 1.1 Thermoplastic Composites in Aerospace

Composite materials currently play a fundamental role in the aerospace industry owing to the continuous pursuit of increased performance at lower costs. The shift from the extensive use of conventional materials, such as aluminum alloys, to composite materials can be explained by the improved mechanical properties of the latter, such as higher strength-to-weight ratios, higher stiffness, higher resistance to creep, fatigue, and environmental degradation. The usage of composites yields considerable savings in weight, thereby leading to lower fuel consumption and costs, which would not have been possible to achieve otherwise [1]. Fiber-reinforced polymer matrix composites are considered state-of-the-art materials, making up a high percentage in weight of most Airbus' and Boeing's recent models [2], as well as being preponderant in the rotary-wing industry and military aircraft [3].

The aerospace industry has been employing almost exclusively thermoset resins such as epoxies in its composite parts. However, the chemical nature of thermosets may lead to problems in handling, manufacturing, and service. Examples of drawbacks of epoxy-based composites are low-temperature storage and still limited shelf-life, health hazards during processing, slow manufacturing process, degradation in wet environments, and poor impact behavior [3]. These shortcomings motivated the development of advanced composites systems with new matrix types that could overcome the mentioned limitations.

Thermoplastic (TP) materials, namely high-performance plastics such as polyetheretherketone (PEEK), polyetherketoneketone (PEKK), and polyphenylene sulfide (PPS), are a viable alternative to thermosets. They present considerable advantages, such as high impact toughness, higher damage tolerance, low moisture absorption, unlimited shelf life at ambient temperature, faster production cycles, and the ability to be melted and reshaped, allowing for recycling [2, 3]. However, the widespread implementation of thermoplastics in the aerospace sector has been precluded by the well-established knowledge in thermosets which have proven capabilities in delivering structural components for safe flight operations at lower costs.

Although the use of thermoplastics in aerospace is still in its early stages, their future is promising

as they have already been successfully included in control surfaces. Note-worthy examples are the fixed-wing leading edge of both Airbus A340 and A380 made of fiberglass reinforced PPS [4], and Gulfstream 650's carbon fiber/PPS rudder and elevator [5]. Furthermore, there are ongoing research and development projects led by Airbus on thermoplastic fuselages [6].

## 1.2 The Fatigue Problem

One of the most critical situations affecting the structural integrity of components in engineering is fatigue. Fatigue is defined as the degradation of mechanical properties leading to failure of a material or component under cyclic loads whose maximum amplitude would be insufficient for failure under a static scenario [1]. Aircraft are subjected to cyclic loads arising from gusts, maneuvers, and pressurization during their service life, making them highly susceptible to fatigue damage and failure [7].

Fatigue is considered a complex phenomenon that can be influenced by several parameters, such as material properties (ductility and toughness), loading and environmental conditions (amplitude, frequency, temperature, and humidity), and inherent defects of the material [8]. This complexity becomes even more evident when it concerns composite materials due to their heterogeneity and anisotropy. Damage accumulation in composites is characterized by multiple damage modes (matrix cracking, interfacial debonding, fiber fracture, transverse-ply cracking, and delamination), unlike isotropic materials, where it occurs by formation and propagation of a single crack [1]. Thus, the well-consolidated knowledge of metal fatigue behavior and the application of conventional approaches, such as linear elastic fracture mechanics (LEFM), is insufficient and inadequate. Therefore, a proper understanding of the fatigue mechanisms is of the utmost importance so that accurate models can be built and catastrophic situations prevented.

### 1.2.1 Frequency and Temperature Effects

In polymer matrix composites (PMCs), especially in matrix-dominated stacking sequences, the matrix is usually the strength limiting component and may control the overall fatigue behavior. The polymeric matrices exhibit time-dependent behavior (viscoelasticity and viscoplasticity), thus the strain rate and, consequently, the frequency will naturally have a significant impact on their fatigue response [3]. Examples can be found in the works of Saff [9], Curtis et al. [10], and Lee and Jen [11], concluding that the loading frequency has minimal effect on  $0^\circ$  unidirectional, cross-ply, and quasi-isotropic laminates, whereas it was a detrimental factor for fatigue life in angle-ply laminates whose behavior is said to be matrix-dominated due to the absence of  $0^\circ$  plies.

Thermoset and thermoplastic matrices can be approached in many cases as one group of polymeric materials. However, the differences in their molecular structure cannot be ignored since the effects of crystallinity, ductility, and processing may be enhanced in thermoplastic fatigue behavior [12]. The higher ductility and toughness of thermoplastic matrices under static conditions are expected to provide an increased capacity to resist damage initiation and failure under fatigue [8]. However, studies have revealed

that more ductile and tough matrices show more extensive damage and shorter fatigue lives than brittle epoxy-based composites [13, 14]. This higher fatigue sensitivity of thermoplastics can be explained by the presence of more pronounced hysteretic effects. When the material is subjected to loading, strain energy is stored and should be released upon unloading. Yet, due to viscoelasticity, there are energy losses each cycle - hysteresis - that manifest in internal heat generation, which should be transferred to the surface by conduction, convection, and radiation. However, the low thermal conductivity of polymers leads to a rapid increase in temperature within the material, also known as autogenous heating. This phenomenon is enhanced at high strain rates since the heat cannot dissipate at the same rate as it is being created, thus making TP-based composites more prone to damage under higher frequencies. The entrapped heat can cause thermal softening and degradation of the mechanical properties, consequently affecting the fatigue life [8].

For epoxy-based composites, Reifsnider et al. [15] found that increasing the loading frequency from 1Hz to 30Hz led to longer fatigue lives. Sun and Chan [16], and Saff [9] were able to obtain similar results, although they also verified that the increase in fatigue life ceased for higher stress levels when sharp temperature rises happened. Contrarily, several authors observed that fatigue life consistently decreased as frequency increased in thermoplastic composites. Curtis et al. [10] tested carbon fiber/PEEK specimens for a frequency range of 0.5-5Hz, and their results showed a decrease in fatigue strength as frequency increased. Significant temperature rises were recorded at higher frequencies, which explains the reduction in fatigue life. Lin et al. [17] used the same material, and their results corroborated the previously mentioned experiments.

Nonetheless, in more recent studies, some authors started observing a beneficial effect of increased frequencies in thermoplastic composites. Eftekhari and Fatemi [18] studied several thermoplastics for a range of frequencies between 0.125Hz and 20Hz and concluded that fatigue life increases with increasing frequency up to a certain limit and then decreases for most loading conditions and materials. That is due to the fact that at higher frequencies, autogenous heating surpasses the beneficial effect of frequency that is usually attributed to crack-tip blunting caused by creep and consequent retardation of crack growth. An insightful literature review on works that demonstrate the aforementioned effect on thermoplastics is also provided in Ref. [18]. Furthermore, it is suggested that time-dependent behaviors of the matrix, such as creep and stress relaxation, may also be affected by autogenous heating and interfere with the overall fatigue performance, but the effect of frequency has not been properly studied [19].

### **1.3 Entropy as a Failure Criterion**

The estimation of fatigue life has always been a topic of interest of many researchers so that, over the years, several experimental methods and theoretical models have been developed. One of the earliest works concerning fatigue life prediction on composites was performed by Hashin and Rotem [20], who proposed a stress-based failure criterion using conventional stress-life (S-N) curves. However, S-N methods are sensitive to the loading conditions and depend on the choice of the reference curve.

Energy-based approaches started to emerge as a more consistent alternative by considering both stress and strain into failure predictions but may still show a large scatter of data. One example of such is the work of Shokrieh and Taheri-Behrooz [21] that developed a strain energy-based model for polymer composite laminates under different stress ratios and off-axis loading.

The efforts to have a more unified fatigue failure criterion culminated in entropy-based approaches, as proposed by Naderi et al. [22]. The premise of their work is that fatigue damage accumulation is accompanied by irreversible energy dissipation, and such process generates entropy in accordance with the second law of thermodynamics. Moreover, the concept of fracture fatigue entropy (FFE) is introduced as the cumulative entropy production up to the fracture point, and results have shown that it is independent of loading amplitude, frequency, and geometry for metallic materials. By performing tests on different metals and measuring the generated entropy, the authors also suggest that FFE is a unique material property. Naderi and Khonsari [23] compared stress-, energy- and entropy-based failure criteria for different stress ratios and loading directions and concluded that only the entropic approach yielded unified results for all combinations of loading conditions. Naderi and Khonsari [24] calculated the FFE of glass/epoxy composites for tension-tension and bending fatigue, with several load amplitudes, frequencies, load ratios, and fiber angles. The authors were able to conclude that FFE was constant for all loading conditions in composite materials likewise.

In more recent studies, it was recognized that the entropy due to heat generation could originate in both non-damaging (internal friction) and damaging processes, and only the latter affected fatigue life. Liakat and Khonsari [25] compared experimental results of entropy generation on metals with finite-element method (FEM) simulations of those experiments, concluding that a match in the FFE values was only possible if the effects of internal friction were removed. Similar conclusions were inferred by Jang and Khonsari [26] and Nourian-Avval and Khonsari [27]. Mehdizadeh et al. [28] performed torsional fatigue tests as well as standard tensile fatigue tests for comparison, and by eliminating internal friction, showed that FFE is even independent of loading type, indicating that it should be considered a material constant. Huang et al. [29] investigated the effects of internal friction in carbon/epoxy laminates with different stacking sequences and concluded that it is more prevalent in matrix-dominated composites such as angle-ply laminates. Additionally, they demonstrated that traditional S-N curves could be obtained in a considerably shorter time using FFE.

Despite the satisfactory results obtained for FFE, not all sources of entropy are contemplated in most cases. All the previously mentioned works do not consider the role of damage for energy and entropy calculations, on the premise that it is a negligible source of energy in metals. However, such simplification is not expected to be suitable for composite materials due to the plethora of damage mechanisms present during fatigue. Gamstedt et al. [30] and Naderi and Khonsari [31] used an approach based on the first law of thermodynamics to conclude that damage energy is significant in composite materials and should be included in the entropy calculation. Mohammadi and Mahmoudi [32] predicted the damage energy with a continuum damage mechanics (CDM)-based constitutive model proposed by Mohammadi et al. [33] and managed to compute FFE for both fibers and matrix with the contribution of damage. The quantification of damage energy is still a challenge for researchers, evidenced by the small number of

works dealing with it, and to date, no well-established approach seems to exist.

If a constant value of FFE for a given material is attained, entropy can be used as a fatigue life prediction method. By calculating the accumulated entropy,  $\gamma$ , at cycle  $N$ , and assuming a linear relationship between the normalized accumulated entropy and normalized fatigue life, the number of cycles to failure,  $N_f$ , can be predicted as,

$$N_f = N \cdot \frac{FFE}{\gamma}. \quad (1.1)$$

The concept of FFE can also be implemented as a stopping criterion in the real-time monitoring of fatigue tests. Naderi and Khonsari [34] performed a study on this regard, where the entropy generated during the fatigue of machinery components was calculated as the test progressed. The authors managed to successfully prevent failure by defining a safety margin of 10%, i.e., when the value of  $\frac{\gamma}{FFE}$  approached 0.9 the fatigue testing machine was programmed to shut down.

The previously cited works illustrate the potential of entropy-based techniques to provide a better understanding of fatigue damage, as well as to prevent catastrophic failure situations. However, FFE is a recent concept, and naturally, the literature on the topic is still limited. Most studies deal with metal fatigue and few are focused on thermosets, but to the best of the author's knowledge, no study has been conducted on thermoplastic laminates.

## 1.4 Motivation and Objectives

The present work is motivated by the increasing popularity of thermoplastic matrix composites in aerospace, accompanied by the still limited research on the topic. The novelty of this work resides in combining the study of the fatigue behavior under different loading conditions with the concept of entropy applied to thermoplastic composites, while using an unprecedented experimental apparatus.

The main objectives to be fulfilled are enumerated:

- Provide a thorough literature review on the effects of loading frequency in the fatigue life of composites and existing experimental work considering entropy as a failure criterion parameter;
- Manufacture thermoplastic composite laminates using automated fiber placement (AFP);
- Conduct thermal-mechanical and static tests to characterize the material;
- Monitor the influence of fatigue loading at low and high frequencies in the spatial distributions of temperature and strain in the tested material;
- Compute the cycle-by-cycle entropy generated due to fatigue with the experimental data, incorporating structural health monitoring (SHM) techniques;
- Quantify the influence of different stacking sequences and loading conditions in the fatigue behavior and generated entropy;
- Identify the damage mechanisms involved in the material failure using optical microscopy.

## 1.5 Thesis Outline

The present thesis is structured in six chapters, whose contents are now briefly described:

### **Chapter 1 - Introduction**

An introduction to the increasing relevance of thermoplastic composites in the aerospace industry is presented, as well as the fatigue problem in composites. Also, the motivation behind studying the entropy generation is introduced by means of an extensive literature review on the matter.

### **Chapter 2 - Theoretical Background**

In this chapter, fundamental concepts of solid mechanics regarding finite and infinitesimal deformations are firstly introduced. Then, the thermodynamic background necessary for the derivation of the entropy equation with experimentally measurable quantities is given. Finally, a formulation for the constitutive law of a viscoelastic-viscoplastic material is developed in order to obtain the remaining terms in the dissipation inequality.

### **Chapter 3 - Manufacture and Material Characterization**

The manufacturing and specimen preparation processes are described in this chapter. Tests performed for thermal and mechanical characterization as well as preliminary fatigue life tests are also thoroughly explained.

### **Chapter 4 - Methodology**

The experimental setup is shown and a detailed explanation about the techniques used for data capturing is provided. The steps and precautions for the development of a new "low-cost" digital image correlation system are documented in this chapter. Lastly, the procedure for data processing is also described.

### **Chapter 5 - Results and Discussion**

The results of the fatigue tests for the two stacking sequences are discussed in great detail in this chapter. Considerations regarding strain evolution, damage and hysteretic behavior are made, as well as an analysis about the entropy generation and fracture fatigue entropy. The usefulness of entropy as a failure criterion is assessed in the last section with comments about the related literature and suggestions to improve the results.

### **Chapter 6 - Conclusion**

A summary of the conclusions derived from the developed work and future work topics following this thesis are stated in the final chapter.



# Chapter 2

## Theoretical Background

### 2.1 Introduction

In a more general case of large deformations, all vector- and tensor-based measures of deformation and stress present in thermodynamic balance laws can be described from different standpoints. Therefore, it is important to first clarify the notions of *reference*, *intermediate* and *current* configurations.

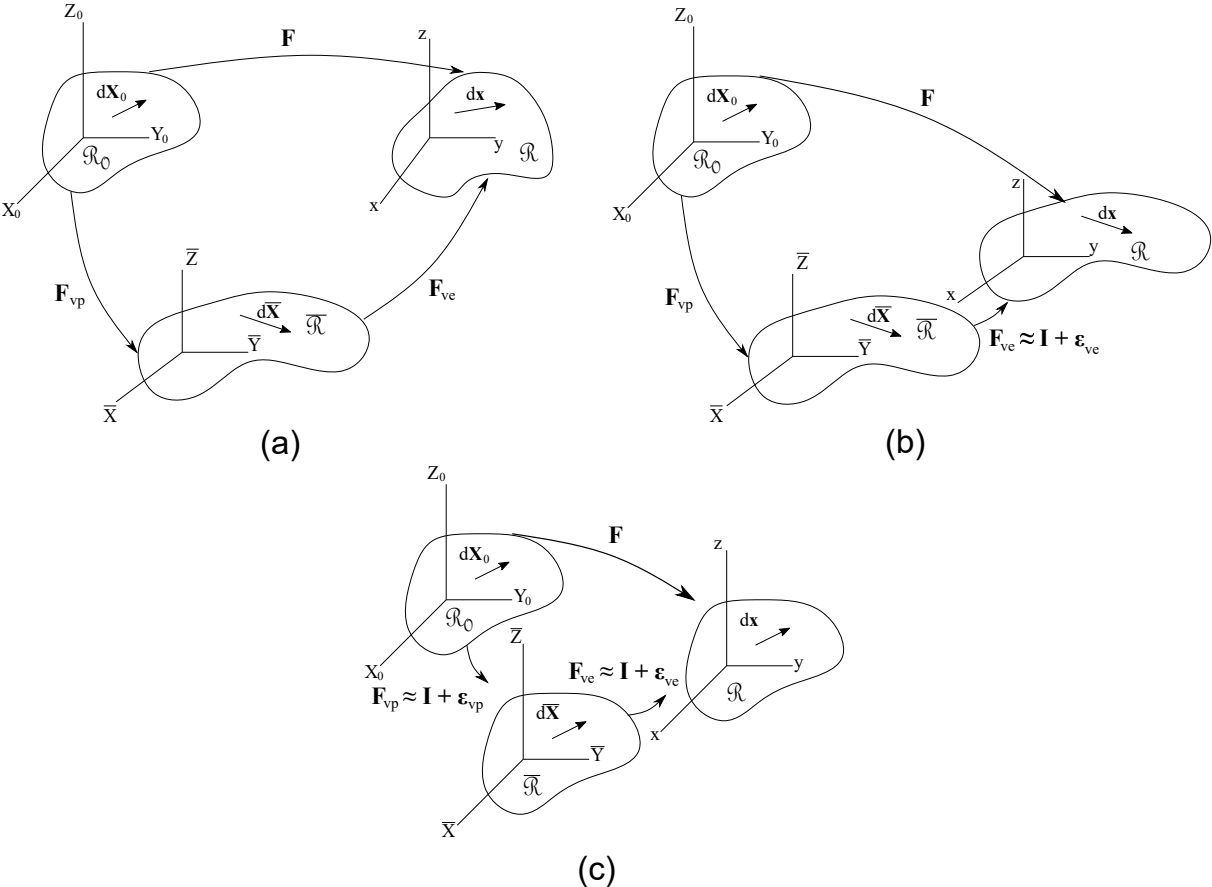


Figure 2.1: Schematic representation of different body configurations, respective system of axes and deformation gradients

Figures 2.1(a)-(c) represent the mapping of a body  $\mathcal{B}$  with boundary  $\partial\mathcal{B}$  between the three above mentioned configurations quantified by deformation gradients,  $\mathbf{F}$  with different orders of magnitude. Scenario (a) consists of the most general case of finite viscoelastic and viscoplastic deformations, while the remaining cases assume, either infinitesimal viscoelastic deformations only (case (b)) or infinitesimal deformations across the full material behaviour spectrum (case (c)). This section will start introducing relevant deformation and stress variables from the most general finite deformation point-of-view and incorporate the necessary simplifications to obtain the infinitesimal deformation cases.

## 2.2 Kinematics of deformation

### 2.2.1 Finite deformations

In this work, the material of interest is assumed to undergo elastic and plastic deformations of the viscous type. Therefore, the deformation gradient  $\mathbf{F}$  is defined by the *Lee-decomposition* [35] as,

$$\mathbf{F} = \frac{d\mathbf{x}}{d\mathbf{X}_0} = \mathbf{F}_{ve}\mathbf{F}_{vp} = \frac{d\mathbf{x}}{d\bar{\mathbf{X}}} \frac{d\bar{\mathbf{X}}}{d\mathbf{X}_0}, \quad (2.1)$$

where the subscripts ve and vp stand for viscoelastic and viscoplastic, respectively.  $\mathbf{F}$  is a mixed second-order tensor, meaning it is quantified with respect to two different right-hand orthonormal bases. Another representation of  $\mathbf{F}$  is given as a function of the displacement gradient,  $\mathbf{H}$ ,

$$\mathbf{F} = \mathbf{I} + \frac{\partial \mathbf{u}}{\partial \mathbf{X}} = \mathbf{I} + \mathbf{H} \quad (2.2)$$

The velocity gradient,  $\mathbf{L}$  is defined in the *current* configuration as,

$$\begin{aligned} \mathbf{L} &= \dot{\mathbf{F}}\mathbf{F}^{-1} = \left( \overline{\dot{\mathbf{F}}_{ve}\mathbf{F}_{vp}} \right) (\mathbf{F}_{ve}\mathbf{F}_{vp})^{-1} = \left( \dot{\mathbf{F}}_{ve}\mathbf{F}_{vp} + \mathbf{F}_{ve}\dot{\mathbf{F}}_{vp} \right) [\mathbf{F}_{vp}^{-1}\mathbf{F}_{ve}^{-1}] = \\ &= \dot{\mathbf{F}}_{ve}\mathbf{F}_{vp}\mathbf{F}_{vp}^{-1}\mathbf{F}_{ve}^{-1} + \mathbf{F}_{ve}\dot{\mathbf{F}}_{vp}\mathbf{F}_{vp}^{-1}\mathbf{F}_{ve}^{-1} = \\ &= \mathbf{L}_{ve} + \mathbf{F}_{ve}\bar{\mathbf{L}}_{vp}\mathbf{F}_{ve}^{-1}. \end{aligned} \quad (2.3)$$

The symmetric component of  $\mathbf{L}$  is the rate of deformation,  $\mathbf{D}$ , also defined in the *current* configuration as,

$$\begin{aligned} \mathbf{D} &= \frac{1}{2} (\mathbf{L} + \mathbf{L}^T) = \frac{1}{2} \left[ (\mathbf{L}_{ve} + \mathbf{F}_{ve}\bar{\mathbf{L}}_{vp}\mathbf{F}_{ve}^{-1}) + (\mathbf{L}_{ve} + \mathbf{F}_{ve}\bar{\mathbf{L}}_{vp}\mathbf{F}_{ve}^{-1})^T \right] \\ &= \mathbf{D}_{ve} + \frac{1}{2} \left[ (\mathbf{F}_{ve}\bar{\mathbf{L}}_{vp}\mathbf{F}_{ve}^{-1}) + (\mathbf{F}_{ve}\bar{\mathbf{L}}_{vp}\mathbf{F}_{ve}^{-1})^T \right]. \end{aligned} \quad (2.4)$$

Two strain tensors will be introduced in this work. The Lagrangian strain,  $\mathbf{E}$ , is a *reference* tensor defined as,

$$\mathbf{E} = \frac{1}{2} (\mathbf{F}^T\mathbf{F} - \mathbf{I}) = \frac{1}{2} \left[ \mathbf{F}_{vp}^T\mathbf{F}_{ve}^T\mathbf{F}_{ve}\mathbf{F}_{vp} - \mathbf{I} \right], \quad (2.5)$$

whereas the Eulerian strain,  $\mathbf{e}$ , is a spatial tensor expressed as,

$$\begin{aligned}
\mathbf{e} &= \frac{1}{2} \left[ \mathbf{I} - \left( \mathbf{F}\mathbf{F}^T \right)^{-1} \right] = \frac{1}{2} \mathbf{I} - \frac{1}{2} \left( \mathbf{F}_{ve} \mathbf{F}_{vp} \mathbf{F}_{vp}^T \mathbf{F}_{ve}^T \right)^{-1} \\
&= \frac{1}{2} \mathbf{I} - \frac{1}{2} \left( \mathbf{F}_{ve} \mathbf{F}_{vp} \mathbf{F}_{vp}^T \mathbf{F}_{ve}^T \right)^{-1} + \frac{1}{2} \left( \mathbf{F}_{ve} \mathbf{F}_{ve}^T \right)^{-1} - \frac{1}{2} \left( \mathbf{F}_{ve} \mathbf{F}_{ve}^T \right)^{-1} \\
&= \frac{1}{2} \mathbf{I} + \frac{1}{2} \mathbf{F}_{ve}^{-T} \mathbf{F}_{ve}^{-1} - \frac{1}{2} \left( \mathbf{F}_{ve} \mathbf{F}_{ve}^T \right)^{-1} - \frac{1}{2} \mathbf{F}_{ve}^{-T} \left( \mathbf{F}_{vp} \mathbf{F}_{vp}^T \right)^{-1} \mathbf{F}_{ve}^{-1} \quad (2.6) \\
&= \frac{1}{2} \left[ \mathbf{I} - \left( \mathbf{F}_{ve} \mathbf{F}_{ve}^T \right)^{-1} \right] + \frac{1}{2} \mathbf{F}_{ve}^{-T} \left[ \mathbf{I} - \left( \mathbf{F}_{vp} \mathbf{F}_{vp}^T \right)^{-1} \right] \mathbf{F}_{ve}^{-1} \\
&= \mathbf{e}_{ve} + \mathbf{F}_{ve}^{-T} \mathbf{e}_{vp} \mathbf{F}_{ve}^{-1},
\end{aligned}$$

## 2.2.2 Infinitesimal viscoelastic deformations

For the case of small viscoelastic and large viscoplastic deformations (Figure 2.1(b)), the order of magnitude of the displacement gradient,  $\varepsilon_{ve}$  can be considered negligible with respect to the identity matrix [36], i.e.

$$\mathbf{F}_{ve} = \mathbf{I} + \varepsilon_{ve} \approx \mathbf{I} \quad (2.7)$$

Hence, the velocity gradient of equation 2.3 can be rewritten as,

$$\mathbf{L} = \mathbf{L}_{ve} + \mathbf{L}_{vp}. \quad (2.8)$$

Using the above results, the rate of deformation tensor can be now decomposed in a sum of viscoelastic and viscoplastic components,

$$\mathbf{D} = \mathbf{D}_{ve} + \mathbf{D}_{vp}. \quad (2.9)$$

This decomposition enables constitutive laws to be defined for  $\mathbf{D}_{ve}$  and  $\mathbf{D}_{vp}$ , the former being associated to the Hypoelasticity theory. However, a similar decomposition of the Lagrangian strain does not hold valid for this particular case, i.e.,

$$\mathbf{E} \neq \mathbf{E}_{ve} + \mathbf{E}_{vp}. \quad (2.10)$$

## 2.2.3 Infinitesimal viscoelastic and viscoplastic deformations

The most simple case of deformation - schematically shown in Figure 2.1(c) - corresponds to small deformations in both viscoelastic and viscoplastic domains, which is deemed valid for strains below 10%. In this assumption, differences in geometry between configurations are negligible, and the summation of viscoelastic and viscoplastic components is admissible if second order terms are neglected, i.e.,

$$\mathbf{E} = \mathbf{e} = \varepsilon = \varepsilon_{ve} + \varepsilon_{vp}, \quad (2.11)$$

where  $\varepsilon$  is the infinitesimal strain tensor.

## 2.3 Thermodynamic balance laws of continuum mechanics

### 2.3.1 Balance of energy

The first law of thermodynamics quantifies the conversion between mechanical and thermal energies. It is postulated as follows,

$$\frac{d}{dt} \int_{\mathcal{B}} \left[ \frac{1}{2} \rho \mathbf{v} \cdot \mathbf{v} + \rho u \right] dv = \int_{\mathcal{B}} \rho \mathbf{b} \cdot \mathbf{v} dv + \int_{\partial \mathcal{B}} \mathbf{t} \cdot \mathbf{v} da + \int_{\mathcal{B}} \rho r dv - \int_{\partial \mathcal{B}} \mathbf{q} \cdot \mathbf{n} da, \quad (2.12)$$

where:

- $u$  is the internal energy per unit mass;
- $\rho$  is the material density;
- $\mathbf{v}$  is the material point's velocity;
- $\mathbf{q}$  is the heat flux vector per unit area;
- $\mathbf{b}$  is the internal body force per unit mass;
- $\mathbf{t}$  is the traction vector;
- $r$  is the heat supply per unit mass.

The terms on the left-hand side of equation 2.12 represent the rate of change in kinetic and internal energies. On the right-hand side of equation 2.12, the first two terms represent the mechanical power due to internal body forces and externally-applied forces, whereas the last two terms represent internal heat generation and energy flowing through the boundaries of  $\mathcal{B}$ .

### 2.3.2 Balance of mechanical energy

From a purely mechanical perspective, the balance of energy can be defined by the following terms,

$$\frac{d}{dt} \int_{\mathcal{B}} \frac{1}{2} \rho \mathbf{v} \cdot \mathbf{v} dv + \int_{\mathcal{B}} \mathbf{T} \cdot \mathbf{D} dv = \int_{\mathcal{B}} \rho \mathbf{b} \cdot \mathbf{v} dv + \int_{\partial \mathcal{B}} \mathbf{t} \cdot \mathbf{v} da. \quad (2.13)$$

The new term on the left-hand side of equation 2.13 represents the mechanical power of the internal body stresses, where  $\mathbf{T}$  is the Cauchy stress tensor and  $\mathbf{D}$  is the rate-of-deformation tensor.

### 2.3.3 Balance of thermal energy

By subtracting the contributions for the mechanical energy balance (equation 2.13) from the total energy balance (equation 2.12), only the thermal contributions remain,

$$\frac{d}{dt} \int_{\mathcal{B}} \rho u dv - \int_{\mathcal{B}} \mathbf{T} \cdot \mathbf{D} dv = \int_{\mathcal{B}} \rho r dv - \int_{\partial \mathcal{B}} \mathbf{q} \cdot \mathbf{n} da, \quad (2.14)$$

Using the localization theorem, equation 2.14 can be written as,

$$\rho \dot{u} = \mathbf{T} \cdot \mathbf{D} + \rho r - \text{div } \mathbf{q}. \quad (2.15)$$

In practical terms, equation 2.15 states the rate of internal energy ( $\rho \dot{u}$ ) is the sum of the mechanical power component ( $\mathbf{T} \cdot \mathbf{D}$ ), the rate of heat supply per unit volume ( $\rho r$ ), and heat exchanged with the surroundings via conduction, convection and radiation ( $\text{div } \mathbf{q}$ ). The mechanical power term is only associated to the deformation of a continuum, whereas the additional rate of work acts as an internal source of energy to represent irreversible phenomena in discontinuous regions of the domain (damage formation and friction).

Based on the decomposition of  $\mathbf{D}$  valid for small viscoelastic deformations presented in equation 2.9, the balance of energy can also be written as,

$$\rho \dot{u} = \mathbf{T} \cdot (\mathbf{D}_{ve} + \mathbf{D}_{vp}) + \rho r - \text{div } \mathbf{q}. \quad (2.16)$$

All terms in equation 2.16 are quantified with respect to the *current* configuration. However, updating the geometry of a solid body undergoing large deformations is challenging. Therefore, other mixed and referential tensors should be considered when quantifying stress and strain in the balance laws. Another admissible form of equation 2.16 can be expressed as,

$$\rho_0 \dot{u} = (J^{-1} \mathbf{P} \mathbf{F}^T) \cdot (\mathbf{D}_{ve} + \mathbf{D}_{vp}) + \rho_0 r - \text{Div } \mathbf{q}_0, \quad (2.17)$$

where  $\mathbf{P}$  is the First Piola-Kirchoff stress (more commonly referred to as engineering stress) and  $J$  is the Jacobian-determinant of  $\mathbf{F}$ . It is important to highlight that all terms in equation 2.17 are measured with respect to the *reference* configuration except for the mechanical power component ( $(J^{-1} \mathbf{P} \mathbf{F}^T) \cdot (\mathbf{D}_{ve} + \mathbf{D}_{vp})$ ). This does not yield any inconsistency given that any scalar term is reference-invariant.

Another useful way of presenting equation 2.17 takes advantage of a work conjugate consisting of the second Piola-Kirchoff stress tensor,  $\mathbf{S}$ , and the Lagrangian strain rate,  $\dot{\mathbf{E}}$ .

$$\rho_0 \dot{u} = \mathbf{S} \cdot \dot{\mathbf{E}} + \rho_0 r - \text{Div } \mathbf{q}_0. \quad (2.18)$$

For the case of infinitesimal deformations, equation 2.18 can be rewritten as,

$$\rho \dot{u} = \sigma \cdot \dot{\epsilon} + \rho r - \nabla \cdot \mathbf{q}, \quad (2.19)$$

where  $\sigma$  is the infinitesimal stress tensor.

### 2.3.4 Second law of thermodynamics

In order to fully determine the direction and validity of thermodynamic processes, the balance of entropy is introduced. In this work, the Clausius statement is considered which states that heat and

entropy flow in the same direction, and neither can vanish without the other. The local form of the second law of thermodynamics can be expressed as,

$$\rho_0 \theta \dot{\eta} \geq \rho_0 r - \text{Div } \mathbf{q}_0 + \mathbf{q}_0 \cdot \frac{\text{Grad } \theta}{\theta}. \quad (2.20)$$

By replacing the thermal energy balance (2.18) in equation 2.20, one obtains,

$$\rho_0 \theta \dot{\eta} \geq \rho_0 \dot{u} - \mathbf{S} \cdot \dot{\mathbf{E}} + \mathbf{q}_0 \cdot \frac{\text{Grad } \theta}{\theta}. \quad (2.21)$$

The Helmholtz free energy per unit mass,  $\psi$ , is now defined as,

$$\psi = u - \eta \theta, \quad (2.22)$$

and its time derivative is expressed as,

$$\dot{\psi} = \dot{u} - \theta \dot{\eta} - \dot{\theta} \eta. \quad (2.23)$$

By replacing the above expression in equation 2.21 and considering isochoric behaviour, one obtains

$$\mathbf{S} \cdot \dot{\mathbf{E}} - \rho_0 (\dot{\psi} + \dot{\theta} \eta) - \mathbf{q}_0 \cdot \frac{\text{Grad } \theta}{\theta} \geq 0. \quad (2.24)$$

The above equation can be rewritten for experimental convenience, since only the engineering stress,  $\mathbf{P}$ , is measured, yielding

$$\mathbf{F}^{-1} \mathbf{P} \cdot \dot{\mathbf{E}} - \rho_0 (\dot{\psi} + \dot{\theta} \eta) - \mathbf{q}_0 \cdot \frac{\text{Grad } \theta}{\theta} \geq 0. \quad (2.25)$$

The respective representation for infinitesimal deformations yields,

$$\boldsymbol{\sigma} \cdot \dot{\boldsymbol{\varepsilon}} - \rho (\dot{\psi} + \dot{\theta} \eta) - \mathbf{q} \cdot \frac{\nabla \theta}{\theta} \geq 0. \quad (2.26)$$

## 2.4 Helmholtz Free Energy

### 2.4.1 Restrictions to constitutive laws

A total of 5 equations are obtained, one from the conservation of mass, three from linear momentum and one from energy. However, these equations are functions of 15 variables:  $\mathbf{v}(\mathbf{x}, t)$  or  $\chi(\mathbf{X}, t)$  (3),  $\theta(\mathbf{x}, t)$  (1),  $\rho(\mathbf{x}, t)$  (1),  $\mathbf{T}$  (6),  $\mathbf{q}$  (3) and  $u$  (1). Therefore, a set of constitutive equations must be proposed in order to fully close the system. Their validity must be assessed through the second law of thermodynamics, and common practice is to propose a constitutive law for the Helmholtz Free Energy. This section will assume infinitesimal deformations to be valid.

Under the assumption of viscoelastic-viscoplastic behavior of a fiber reinforced polymer, the Helmholtz

free energy is defined as the sum of viscoelastic and viscoplastic contributions,

$$\psi(t) = \psi_{ve}(t) + \psi_{vp}(t). \quad (2.27)$$

Both components will be a function of both observable and internal variables and parameters. The former consist of the *infinitesimal strain tensor*,  $\varepsilon$ , and *temperature*,  $\theta$ , while the latter comprise a *scalar damage variable*,  $D$ , and *kinematic hardening*,  $\alpha$ .

Due to the viscous behavior of the polymeric material, the Helmholtz free energy at the current time,  $t$ , must be a function of the current and past histories of the variables in the argument which can be quantified using functional theory,

$$\psi_{ve}(t) = \tilde{\psi}_{s=0}^{\infty} \{ \varepsilon_{ve}(t-s), \theta(t-s), D(t-s) \}, \quad (2.28)$$

where  $s \leq t$  represent the material's past time, i.e., increasing  $s$  is equivalent to searching further back in the material's past history. In other words, the Helmholtz free energy depends on all values taken by  $\mathbf{E}_{ve}(t)$ ,  $\theta(t)$  and  $D(t)$  in the intervals  $t \in [0, \infty]$ . A more compact notation will be used to represent the time histories,  $\Lambda^t(s) = \Lambda(t-s)$ ,

$$\psi_{ve}(t) = \tilde{\psi}_{s=0}^{\infty} \{ \Lambda^t(s) \}, \quad (2.29)$$

where  $\Lambda^t(s) = \{ \varepsilon_{ve}^t(s), \theta^t(s), D^t(s) \}$ . Alternatively, the Helmholtz Free Energy can be represented as a function of the difference histories,  $\Lambda_d^t(s) = \Lambda(t-s) - \Lambda(t)$  and current values,  $\Lambda(t)$ ,

$$\psi_{ve}(t) = \tilde{\psi}_{s=0}^{\infty} \{ \Lambda_d^t(s); \Lambda(t) \} = \int_0^{\infty} f(\Lambda_d^t(s); \Lambda(t)) ds, \quad (2.30)$$

where the semi-colon separates variables (on the left) from known parameters (on the right). This constitutive law is associated to a simple material.

On the other hand,  $\psi_{vp}$  can be represented as,

$$\psi_{vp}(t) = \tilde{\psi}_{s=0}^{\infty} \{ \theta(t-s), \alpha(t-s) \} = \tilde{\psi}_{s=0}^{\infty} \{ \theta_d^t(s), \alpha_d^t(s); \theta(t), \alpha(t) \} = \tilde{\psi}_{s=0}^{\infty} \{ \Gamma_d^t(s); \Gamma(t) \}, \quad (2.31)$$

where  $\Gamma_d^t(s) = \{ \theta_d^t(s), \alpha_d^t(s) \}$ . The viscoplastic infinitesimal strain tensor,  $\varepsilon_{vp}$ , will not be included in the list of arguments of the Helmholtz free energy since it can be represented as a function of the hardening variables. The next sections will be focused on the mathematical background necessary to develop expressions for  $\psi_{ve}$  and  $\psi_{vp}$ .

## 2.4.2 Application to the dissipation inequality

The balance of entropy presented in equation 2.26 should be applicable to any continuum. Therefore, the balance of entropy imposes a natural restriction to the validity of the proposed constitutive law.

The step-by-step differentiation of the Helmholtz Free Energy with respect to time,  $\dot{\psi}(t)$ , will be provided in the following paragraphs. In a more general sense,  $\dot{\psi}(t)$  can be partitioned in time derivatives

with respect to the viscoelastic and viscoplastic components of the Helmholtz Free energy,

$$\dot{\psi}(t) = \frac{d\psi(t)}{dt} = \frac{d\psi_{ve}(t)}{dt} + \frac{d\psi_{vp}(t)}{dt}. \quad (2.32)$$

The general form of the derivative of the Helmholtz Free Energy functional with respect to time is given by,

$$\frac{d\psi(t)}{dt} = \frac{d}{dt} \int_0^\infty f(\Lambda_d^t(s); \Lambda(t)) ds. \quad (2.33)$$

Since the integral limits are not a function of  $t$ , the differential can directly operate on the function  $f$ ,

$$\frac{d\psi(t)}{dt} = \int_0^\infty \frac{d}{dt} f(\Lambda_d^t(s); \Lambda(t)) ds. \quad (2.34)$$

The well-known chain rule from real calculus can be also applied to  $f$  which is a function of one variable ( $\Lambda_d^t(s)$ ) and one known parameter ( $\Lambda(t)$ ). The notation used by Coleman [37] will be considered in this work:

$$\int_0^\infty \frac{d}{dt} f(\Lambda_d^t(s); \Lambda(t)) ds = \int_0^\infty \delta f(\Lambda_d^t(s); \Lambda(t)) \dot{\Lambda}_d^t(s) + \partial_\Lambda f(\Lambda_d^t(s); \Lambda(t)) \cdot \dot{\Lambda}(t) ds. \quad (2.35)$$

The time derivative of  $\dot{\Lambda}_d^t(s)$  can be alternatively expressed as,

$$\dot{\Lambda}_d^t(s) = -\frac{d}{ds} \Lambda^t(s) - \dot{\Lambda}(t). \quad (2.36)$$

Replacing 2.36 in 2.35 yields,

$$\dot{\psi}(t) = \int_0^\infty \delta f(\Lambda_d^t(s); \Lambda(t)) \left[ -\frac{d}{ds} \Lambda^t(s) - \dot{\Lambda}(t) \right] + \partial_\Lambda f(\Lambda_d^t(s); \Lambda(t)) \cdot \dot{\Lambda}(t) ds. \quad (2.37)$$

Given that  $\dot{\Lambda}(t)$  is independent of  $s$ , it can be removed from the integral as a constant, hence one can rewrite equation 2.37 as,

$$\dot{\psi}(t) = \delta \int_{s=0}^\infty \psi(\Lambda_d^t(s); \Lambda(t)) \left[ -\frac{d}{ds} \Lambda^t(s) \right] + \left[ \partial_\Lambda \int_{s=0}^\infty \psi(\Lambda_d^t(s); \Lambda(t)) - \nabla \int_{s=0}^\infty \psi(\Lambda_d^t(s); \Lambda(t)) \right] \cdot \dot{\Lambda}(t). \quad (2.38)$$

Expansion of equation 2.38 for the case of viscoelastic and viscoplastic components yields,

$$\begin{aligned} \dot{\psi}_{ve}(t) = & \delta \int_{s=0}^\infty \psi(\Lambda_d^t(s); \Lambda(t)) \left[ -\frac{d}{ds} \varepsilon_{ve}^t(s) \right] + \left[ \partial_{\varepsilon_{ve}} \int_{s=0}^\infty \psi(\Lambda_d^t(s); \Lambda(t)) - \nabla_{(\varepsilon_{ve})^t} \int_{s=0}^\infty \psi(\Lambda_d^t(s); \Lambda(t)) \right] \cdot \dot{\varepsilon}_{ve}(t) + \\ & \delta \int_{s=0}^\infty \psi(\Lambda_d^t(s); \Lambda(t)) \left[ -\frac{d}{ds} \theta^t(s) \right] + \left[ \partial_\theta \int_{s=0}^\infty \psi(\Lambda_d^t(s); \Lambda(t)) - \nabla_{\theta^t} \int_{s=0}^\infty \psi(\Lambda_d^t(s); \Lambda(t)) \right] \dot{\theta}(t) + \\ & \delta \int_{s=0}^\infty \psi(\Lambda_d^t(s); \Lambda(t)) \left[ -\frac{d}{ds} D^t(s) \right] + \left[ \partial_D \int_{s=0}^\infty \psi(\Lambda_d^t(s); \Lambda(t)) - \nabla_{D^t} \int_{s=0}^\infty \psi(\Lambda_d^t(s); \Lambda(t)) \right] \dot{D}(t), \end{aligned} \quad (2.39)$$

$$\begin{aligned} \dot{\psi}_{vp}(t) = & \delta \int_{s=0}^\infty \psi(\Gamma_d^t(s); \Gamma(t)) \left[ -\frac{d}{ds} \alpha^t(s) \right] + \left[ \partial_\alpha \int_{s=0}^\infty \psi(\Gamma_d^t(s); \Gamma(t)) - \nabla_{\alpha^t} \int_{s=0}^\infty \psi(\Gamma_d^t(s); \Gamma(t)) \right] \dot{\alpha}(t) + \\ & \delta \int_{s=0}^\infty \psi(\Gamma_d^t(s); \Gamma(t)) \left[ -\frac{d}{ds} \theta^t(s) \right] + \left[ \partial_\theta \int_{s=0}^\infty \psi(\Gamma_d^t(s); \Gamma(t)) - \nabla_{\theta^t} \int_{s=0}^\infty \psi(\Gamma_d^t(s); \Gamma(t)) \right] \dot{\theta}(t). \end{aligned} \quad (2.40)$$



Replacing the above results into equation 2.26 yield the following constitutive relations for a material with memory,

$$\sigma = \rho \left[ \partial_{\varepsilon_{ve}} \overset{\infty}{\psi} (\Lambda_d^t(s); \Lambda(t)) - \nabla_{(\varepsilon_{ve})_d^t} \overset{\infty}{\psi} (\Lambda_d^t(s); \Lambda(t)) \right] \quad (2.41a)$$

$$\eta = \nabla_{\theta_d^t} \overset{\infty}{\psi} (\Lambda_d^t(s), \Gamma_d^t(s); \Lambda(t), \Gamma(t)) - \partial_{\theta} \overset{\infty}{\psi} (\Lambda_d^t(s), \Gamma_d^t(s); \Lambda(t), \Gamma(t)). \quad (2.41b)$$

Only dissipative terms will remain in the final form of the entropy balance, as follows,

$$\begin{aligned} & \rho \left( \delta \overset{\infty}{\psi} (\Lambda_d^t(s); \Lambda(t)) \Big| - \frac{d}{ds} \Lambda^t(s) + \delta \overset{\infty}{\psi} (\Gamma_d^t(s); \Gamma(t)) \Big| - \frac{d}{ds} \Gamma^t(s) \right) + \\ & \rho \left( \left[ \partial_{\alpha} \overset{\infty}{\psi} (\Gamma_d^t(s); \Gamma(t)) - \nabla_{\alpha_d^t} \overset{\infty}{\psi} (\Gamma_d^t(s); \Gamma(t)) \right] \dot{\alpha}(t) + \left[ \partial_D \overset{\infty}{\psi} (\Lambda_d^t(s); \Lambda(t)) - \nabla_{D_d^t} \overset{\infty}{\psi} (\Lambda_d^t(s); \Lambda(t)) \right] \dot{D}(t) \right) - \\ & \sigma \cdot \dot{\varepsilon}_{vp} + \mathbf{q} \cdot \frac{\nabla \theta}{\theta} \leq 0. \end{aligned} \quad (2.42)$$

In addition to plastic and heat dissipation terms ( $\sigma \cdot \dot{\varepsilon}_{vp}$  and  $\mathbf{q} \cdot \frac{\nabla \theta}{\theta}$ , respectively), damage generation, kinematic hardening and viscous effects are also accounted for in equation 2.42.

The generated entropy,  $\gamma$ , is obtained by integrating in time the previous equation, and is shown in a more compact notation in equation 2.43, where  $\eta_v$  is the entropy per unit mass generated due to viscous phenomena. The present thesis will focus on experimentally calculating entropy from the first two terms on the RHS of equation 2.43, in line with the approaches taken in previous works.

$$\gamma = \int_0^t \frac{\sigma \cdot \dot{\varepsilon}_{vp}}{\theta} - \mathbf{q} \cdot \frac{\nabla \theta}{\theta^2} - \frac{\rho}{\theta} \left( \dot{\eta}_v + \frac{\partial \psi_{vp}}{\partial \alpha} \cdot \dot{\alpha}(t) + \frac{\partial \psi_{ve}}{\partial D} \cdot \dot{D}(t) \right) dt \geq 0, \quad (2.43)$$



## Chapter 3

# Manufacture and Material Characterization

### 3.1 Material Description

The selection of the material used to conduct the present study was based on availability at the research center and applicability to the aerospace industry. The chosen material was Toray Cetex<sup>®</sup> TC1320, supplied in the form of unidirectional (UD) prepreg tapes of carbon/PEKK. This material is qualified for use in aerostructures, particularly in the eVTOL (electric vertical take-off and landing) and Urban Air Mobility market segments [38].

The physical properties of the UD tape are shown in Table 3.1, as taken from the manufacturing datasheet.

Table 3.1: Physical properties of TC1320 [38].

|   |           |
|---|-----------|
| Fiber areal weight (g/m <sup>2</sup> )              | 145       |
| Resin content by weight (%)                         | 34        |
| Consolidated ply thickness (mm)                     | 0.14      |
| Density (g/cm <sup>3</sup> )                        | 1.59      |
| Processing temperature, $T_p$ (°C)                  | 370 – 400 |
| Neat resin glass transition temperature, $T_g$ (°C) | 160       |
| Neat resin melting temperature, $T_m$ (°C)          | 337       |

### 3.2 Composite Plate Manufacturing

The stacking sequences under study should have meaningful research impact and applicability in the aerospace industry. Therefore, two stacking sequences were considered:

- Angle-ply (AP) [+45/-45]<sub>4s</sub>, whose response to frequency and self-heating effects are enhanced by its matrix dominated behavior as referred to in Section 1.2.1, presenting significant research

interest;

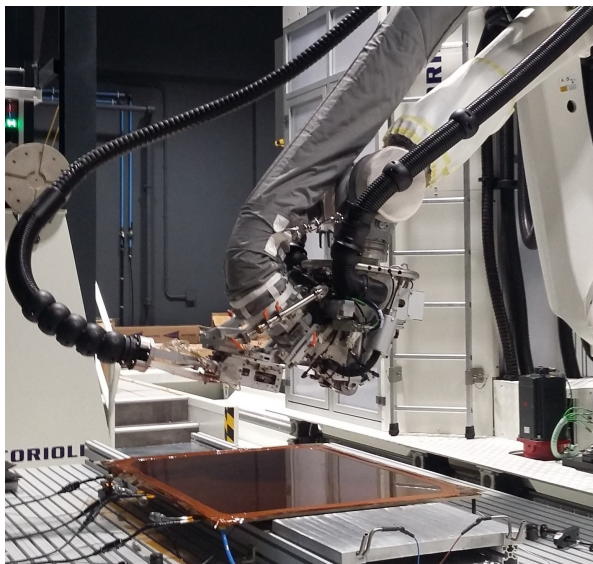
- Quasi-isotropic (QI)  $[0/+45/-45/90]_{2s}$ , which is a commonly used sequence in the aerospace industry, since it can evenly withstand loads applied along any direction [2].

Two plates of  $615\text{mm} \times 555\text{mm}$  with 16 plies were manufactured using the laser-assisted automated fiber placement (AFP) machine shown in Figure 3.1a).

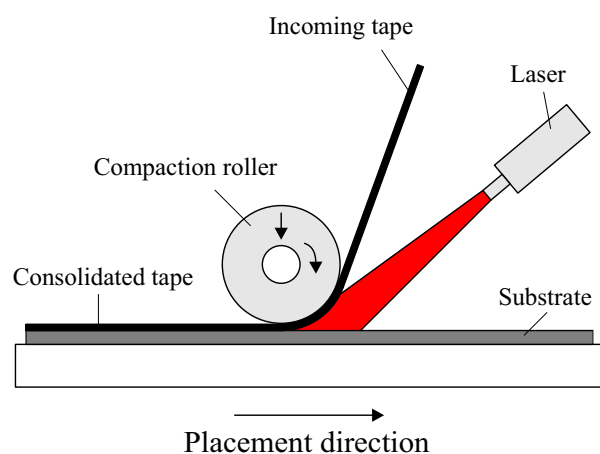
### 3.2.1 Automated Fiber Placement

AFP is an advanced method of manufacturing composites where narrow prepreg tapes, also called tows, are fed into a robotic fiber placement head and laid onto the substrate one layer at a time, undergoing *in situ* consolidation. This consolidation is achieved by means of a roller that applies a compaction force on the tape, while a heat source (laser, infra-red or hot gas) melts the thermoplastic material, bonding the tape to the substrate or the previous layer. The process is repeated tape-by-tape for each ply and ply-by-ply until the final stacking sequence and geometry are achieved. A schematic of this process is illustrated in Figure 3.1b).

The automated robotic machinery present in AFP provides high repeatability and consistency while providing increased lay-up speeds, essential for a cost-efficient manufacturing of large components. Also, the multi-axis articulating robot allows the manufacturing of complex-shaped parts, such as fuselages, wing covers, and spars. Many aerospace components are currently relying on AFP, some of the most notable examples being the empennages (vertical and horizontal stabilizer) of the Boeing 777, Airbus A340, and A380 [2].



(a) AFP machine at SU-IMC



(b) Schematic of the AFP process

Figure 3.1: AFP system.

The most important parameters to achieve a good consolidation are the compaction force, the lay-up speed, and the nip-point temperature, greatly influencing the quality of the laminates. For the present

study, the chosen parameters are given in Table 3.2.

Table 3.2: Process parameters for the manufactured plates.

|                            |     |
|----------------------------|-----|
| Compaction force (N)       | 400 |
| Lay-up speed (m/s)         | 0.2 |
| Nip-point temperature (°C) | 430 |

The AFP-manufactured plates are shown in Figure 3.2. For the AP laminate in Figure 3.2a), the photograph was taken halfway through the lay-up of one of the layers, so that the consolidated tapes of both fiber orientations (+45° and -45°) could be easily seen. Furthermore, a protuberance in the interface of consecutive tapes can be observed. This is caused by an intentional overlap of the tows, since it was necessary to ensure that there were no gaps between tows arising from robot precision errors that could lead to unreinforced regions.

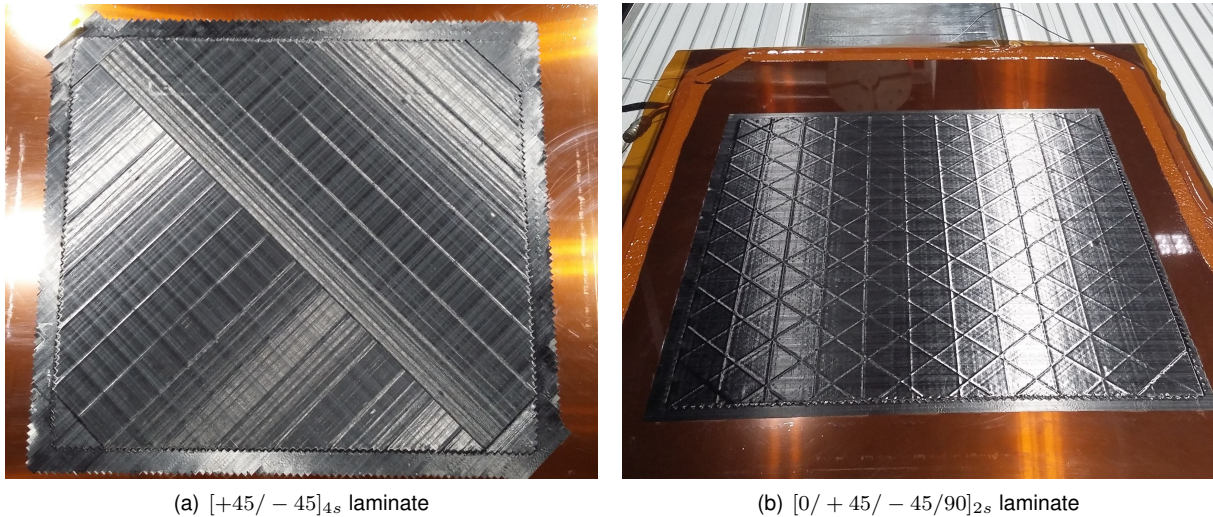


Figure 3.2: Composite plates manufactured using AFP.

### 3.2.2 Autoclave

Although AFP is considered an out-of-autoclave process for thermoplastic composites providing consolidated plates with good quality, the mechanical properties of the fabricated laminates can be improved by undergoing a post-consolidation treatment in the autoclave.

The AFP-manufactured composite plates were bagged and placed into the autoclave, as shown in Figure 3.3. Then, temperature and pressure were increased from ambient conditions to 378°C and 8bar, respectively. Both heating and cooling stages were conducted at the rate of 4°C/min. The temperature and pressure profiles of the processing cycle can be seen in Figure 3.4.

The final composite plates after consolidation in the autoclave are shown in Figure 3.5. An improvement in the surface quality of the plates is observed by presenting a more uniform thickness distribution. Both plates also have similar imprints of the fibers, making them indistinguishable to the naked eye. That is due to the fact that the high temperature and pressure applied by the autoclave enabled the movement



Figure 3.3: Setup for autoclave consolidation.

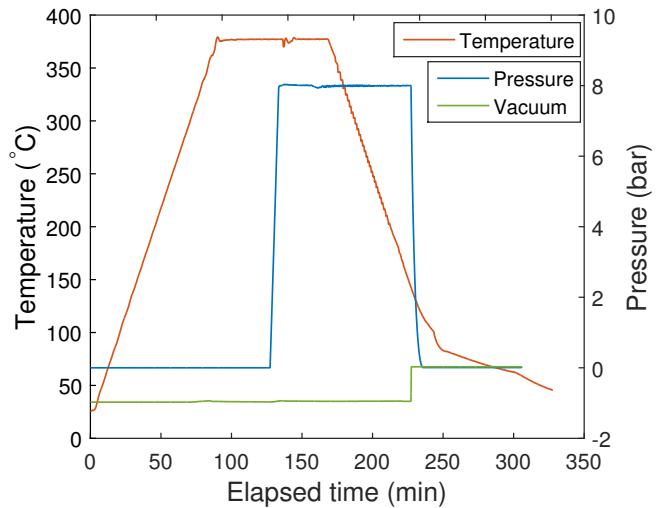
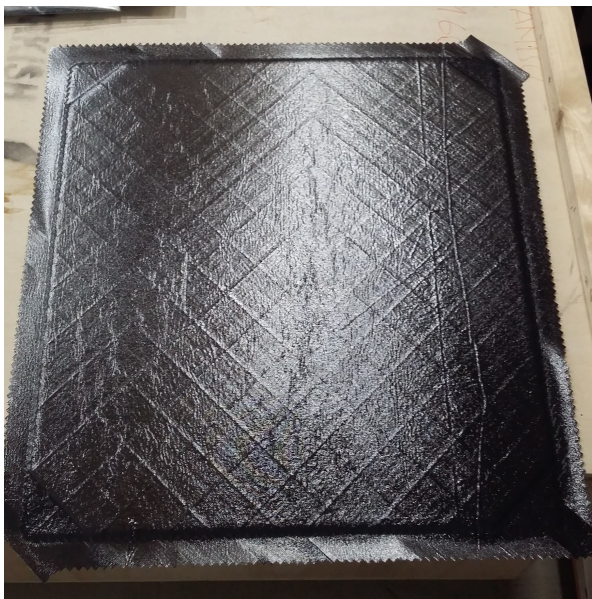
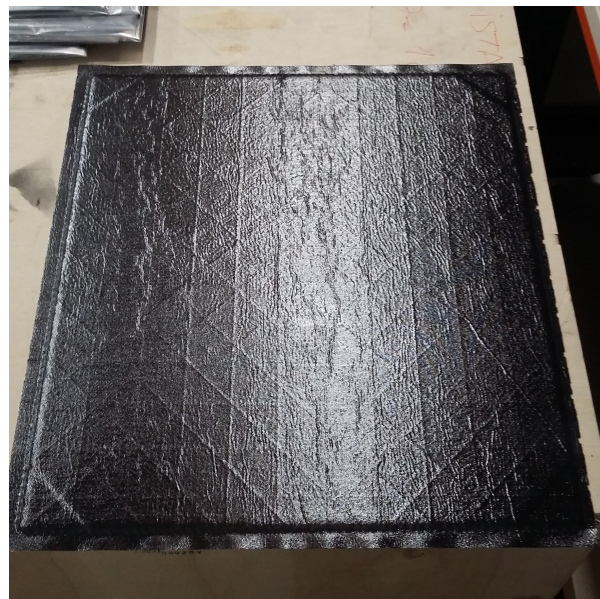


Figure 3.4: Autoclave processing cycle for consolidation of carbon fiber/PEKK.

of the polymer's molecular chains, reducing the void content and flattening the overlaps of the tows.



(a) [+45/-45]<sub>4s</sub> laminate



(b) [0/+45/-45/90]<sub>2s</sub> laminate

Figure 3.5: Composite plates after consolidation in autoclave.

### 3.2.3 Abrasive water jet machining

The specimen cutting process was performed using water jet machining with abrasive flow. While programming the machine, it was ensured that the specimens would not contain any material within 2cm from the edges since the AFP process might have induced some defects in that region. Also, the jet was set to initially strike the plate away from the actual specimen cutting line as extensive delaminations in the impact point were observed.

The abrasive water jet process parameters used for optimal surface quality are stated in Table 3.3.

Table 3.3: Process parameters for the abrasive water jet machining.

|                          |     |
|--------------------------|-----|
| Water jet pressure (MPa) | 300 |
| Jet diameter (mm)        | 0.8 |
| Feedrate (mm/min)        | 250 |
| Abrasive flow (g/min)    | 35  |

### 3.3 Material Characterization

#### 3.3.1 Thermal Conductivity

The last term on the RHS of the dissipation inequality (Eq. 2.26) features the entropy generated due to heat conduction in the specimen. As the value of thermal conductivity was not given by the manufacturer, tests were performed to experimentally determine it.

The method used was the transient plane heat source (TPS), as per the ISO 22007-2 [39]. This method consists in placing a probe of negligible heat capacity between two slabs of the material under study, which will act as a temperature sensor coupled with a heat source. Then, an electrical current is applied through the probe, translating into a heat pulse. The heat dissipation rate depends on the thermal properties of the specimens, hence, by monitoring the temperature increase as a function of time, thermal conductivity, thermal diffusivity, and specific heat capacity can be calculated. The setup used for the tests is shown in Figure 3.6.

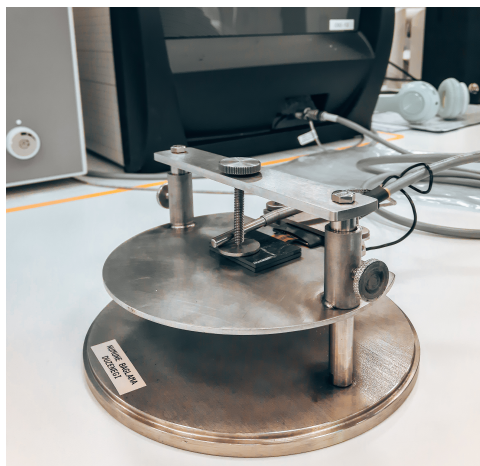


Figure 3.6: Setup for the TPS method.

The test was repeated for different temperatures to minimize the error arising from the heat generated during fatigue. Since the sample is not isotropic, thermal conductivity was measured longitudinally to the fiber direction,  $k_L$ , and along the transverse directions,  $k_T$ .

For composite laminates, the fiber orientation in each ply,  $\theta_i$ , varies, assuming an identical thickness and fiber fraction for all plies. The measurements were made in the  $x'y'z'$  axis (vide Figure 3.7), hence

not corresponding to the loading direction. In order to obtain a lamina's thermal conductivity tensor along the global coordinates of the specimen (xyz), a rotation transformation is performed, yielding:

$$\begin{cases} k_{x_i} = k_L \cos^2 \theta_i + k_T \sin^2 \theta_i \\ k_{y_i} = k_L \sin^2 \theta_i + k_T \cos^2 \theta_i \\ k_z = k_T \end{cases} \quad (3.1)$$

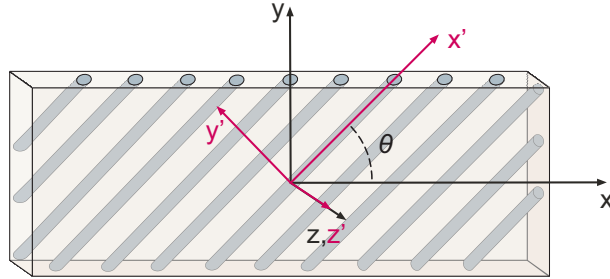


Figure 3.7: Global and lamina coordinate systems.

A model of parallel thermal resistances can be applied to infer the global thermal conductivity tensor of the composite material, with N stacked plies, as follows [40]:

$$k_d = \frac{1}{N} \left( \sum_{i=1}^N k_{d_i} \right)_{d=x,y} \quad (3.2)$$

The results are shown in Table 3.4 for the two laminates.

Table 3.4: Thermal conductivity results.

|           |       | $k_{x,y}$ (Wm/K) | $k_z$   |
|-----------|-------|------------------|---------|
| <b>AP</b> | 23°C  | 1.6482           | 0.54321 |
|           | 50°C  | 1.6871           | 0.71336 |
|           | 100°C | 1.6885           | 0.80323 |
| <b>QI</b> | 23°C  | 1.7497           | 0.51923 |
|           | 50°C  | 1.8131           | 0.59359 |

### 3.3.2 Emissivity

During the fatigue tests, a thermal camera was used to monitor the surface temperature of the specimen. The camera detects the infrared energy emitted by the body and calculates the temperature using the Stefan-Boltzmann law. Therefore, the accuracy of the measured temperature depends on the emissivity input value in the camera's software (ResearchIR). Since the specimen has a speckle pattern coating (random dots of black and white paint), the emissivity cannot be approximated to the one of a black or white body without significant loss of accuracy. Although this inhomogeneous emissivity on the



sample surface poses a challenge to thermographic measurements, no value for the speckle pattern was found in the literature, motivating the development of a measurement procedure.

## Procedure

In the present work, the emissivity of the speckle pattern was determined following a modification of the methodology described by Marques [41] and the camera's user manual [42]. In addition to the thermal camera, computer with ResearchIR software installed, and a furnace, the following set of materials was needed:

- Aluminum foil, crumpled to make the reflected radiation more diffuse;
- Electrical tape (3M type 35);
- White and black paint for speckle pattern coating;
- Clip to support the specimen vertically while in the furnace.

The specimen was coated using the mentioned materials, as shown in Figure 3.8. The use of black electrical tape is based on the fact that it is a material with known high emissivity, therefore providing a suitable reference value for the measurements. On the other hand, the aluminum foil is chosen assuming it is a perfect reflector, so its apparent temperature is equal to the reflected apparent temperature from the surroundings. However, the value of the emissivity for this region should be set to 1, which might seem contradictory as the well-known value for perfect reflectors is  $e = 0$ . The reason is that for calculation purposes using the software, a value of 0 would give an error. Instead, since the reflected radiation by the aluminum foil is said to represent all the radiation in the surroundings, it can be assumed to be equivalent to the radiation emitted by a perfect radiator, hence the use of  $e = 1$ .

The followed steps are listed below and the experimental setup is shown in Figure 3.9.

1. Place the specimen inside the furnace as further away from the door as possible. This guarantees almost negligible heat losses by convection to the environment once the door is open to take measurements with the thermal camera;
2. Increase the temperature up to a value 20K higher than the ambient temperature;
3. Once steady-state conditions have been reached, slightly open the door to take temperature measurements using the ResearchIR software in the following order:
  - Create a rectangular area in the aluminum foil region, set the emissivity to 1, and determine the average temperature measured in the box. This temperature will be hereinafter referred to as *background temperature*,  $T_b$ . Then, use the value of  $T_b$  as input in the "Reflected Temperature" field of the software. This parameter is used to compensate for the radiation reflected in the object from the surroundings;
  - Create boxes in the electrical tape and speckle pattern regions, set the emissivity of both to that of the electrical tape, and determine the respective average temperature of both. In the

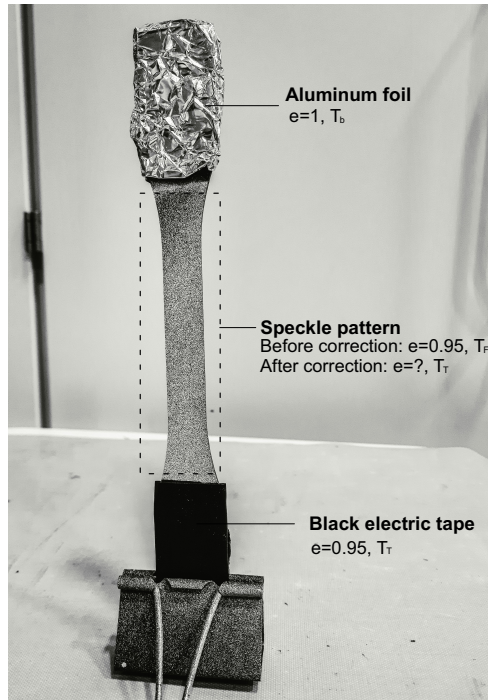


Figure 3.8: Specimen coated with different materials.

electrical tape region, the measured average temperature will be referred to as *true temperature*,  $T_T$ , since the value of its emissivity is correct, therefore yielding true temperature values. Analogously, for the speckle pattern region, the measured temperature will be referred to as *fake temperature*,  $T_F$ , since a false value of emissivity is assumed, therefore not producing an accurate measurement;

4. Close the door of the furnace and restart from step 4 until obtaining a reasonable number of data points;
5. Perform the following set of calculations:

- The total rate of energy detected by the thermal camera by radiation, i.e. radiosity ( $J$ ), is the sum of the emissive power ( $E$ ) and reflected irradiation ( $\rho G$ ) components,

$$J = E + \rho G, \quad (3.3)$$

where  $\rho$  is the reflectivity, and  $G$  is the irradiation. Considering the specimen to be negligibly small compared to the furnace dimensions which is kept at a constant temperature, any irradiation experienced by the specimen can be assumed to be emitted by a black body,

$$J = \epsilon \sigma T_S^4 + \rho \sigma T_b^4, \quad (3.4)$$

where  $\sigma$  is the Stefan Boltzmann's constant ( $= 5.67 \times 10^{-8}$ ) and  $T_S$  is the specimen surface's temperature.

- For an opaque body,  $\rho + \alpha = 1$ , where  $\alpha$  is the material's absorptivity. Therefore, equation 3.4 can be rearranged as,

$$J = e\sigma T_S^4 + \sigma T_b^4 - \alpha\sigma T_b^4, \quad (3.5)$$

- Under a thermodynamic equilibrium, the Kirchoff's law of thermal radiation applies, i.e.  $\alpha = e$ . Although this assumption only remains valid when  $T_S = T_b$ , the IR camera's user manual reports this assumption to be considered for any temperature measurements. Therefore, equation 3.5 can be simplified as,

$$J = e\sigma(T_S^4 - T_b^4) + \sigma T_b^4, \quad (3.6)$$

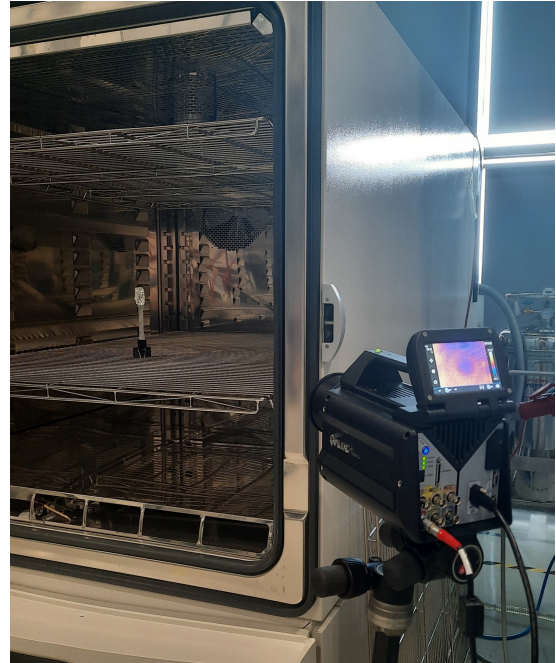
- At this stage, only the temperature on the black tape is accurately known since  $e$  was set to the one of the black tape ( $e_{BT}$ ). This temperature should be uniform throughout the specimen. Moreover, the combination of temperature and emissivity settings for the speckle pattern region should always yield the same value of  $J$ . Based on these pieces of information, the true emissivity of the speckle pattern,  $e_{SP}$ , can be determined,

$$J = \text{cte} \Leftrightarrow e_{BT}\sigma(T_F^4 - T_b^4) = e_{SP}\sigma(T_T^4 - T_b^4) \quad (3.7)$$

$$e_{SP} = \frac{e_{BT}(T_F^4 - T_b^4)}{(T_T^4 - T_b^4)}$$



(a)



(b)

Figure 3.9: Setup for the emissivity tests.

The procedure listed above differs from the one present in the camera's user manual in the last step, i.e., the determination of the emissivity. Originally, the manual describes a trial-and-error approach, where several emissivity values are used as an input until a match of both temperatures is observed. In

this work, a calculation-based approach is suggested which is expected to give faster and more reliable results.

The measurement function used by the camera to obtain the temperature in each region is an average of the temperature of all points within the defined box, and their individual values might present a significant difference. To access how much this deviation can affect the final emissivity value, an expression is developed for the variance of  $e_{SP}$  as a function of the variances and mean values of the temperature in each region (given by the software) [43]:

$$var\{f(x_1, x_2, \dots, x_n)\} \equiv \sum \sum \left( \frac{\partial f}{\partial x_i} \right) \left( \frac{\partial f}{\partial x_j} \right) cov(x_i, x_j) \quad (3.8)$$

$$e_{SP} = f(T_F, T_T, T_b) = e_{BT} \frac{T_F^4 - T_b^4}{T_T^4 - T_b^4} \quad (3.9)$$

$$var(e_{SP}) = e_{BT}^2 \cdot \left[ \left( \frac{\partial f}{\partial T_F} \right)^2 var(T_F) + \left( \frac{\partial f}{\partial T_T} \right)^2 var(T_T) + \left( \frac{\partial f}{\partial T_b} \right)^2 var(T_b) \right] \quad (3.10)$$

## Results

The temperature inside the furnace was raised to 45°C and a set of ten measurements was performed to ensure good repeatability. Additionally, the temperature was raised to 55°C to account for any significant dependence of the emissivity on that range of temperatures, and a new set of ten measurements was carried out. Table 3.5 displays the results of the average emissivity and standard deviation (from Eq. 3.10) for the two cases.

|      | $\bar{e}_{SP}$ | $SD(e_{SP})$ |
|------|----------------|--------------|
| 45°C | <b>0.83</b>    | 0.07         |
| 55°C | 0.82           | 0.10         |

Table 3.5: Results of the emissivity tests.

The high standard deviation in each measurement is mostly due to the variance of temperature in the aluminum foil region (Box 1), as seen in Figure 3.10. After experimenting with other pieces of aluminum foil, it was concluded that it must be very well crumpled, otherwise the standard deviation in that region would be up to ten times larger. In such case, the background temperature ( $T_b$ ) was not accurate and consequently the emissivity values were highly scattered and far from a normal distribution. At 55°C, there are larger temperature gradients due to convection when opening the door, which leads to an increased error if the measurements are not taken quickly.

Nonetheless, the obtained emissivity values for the two temperatures do not present a considerable difference, especially when considering the challenges and the inherent sources of error of this method. Therefore, it will be assumed that the emissivity is constant in the range of temperatures experienced during fatigue, and the value of  $e = 0.83$  is chosen as the input for the subsequent thermographic measurements.

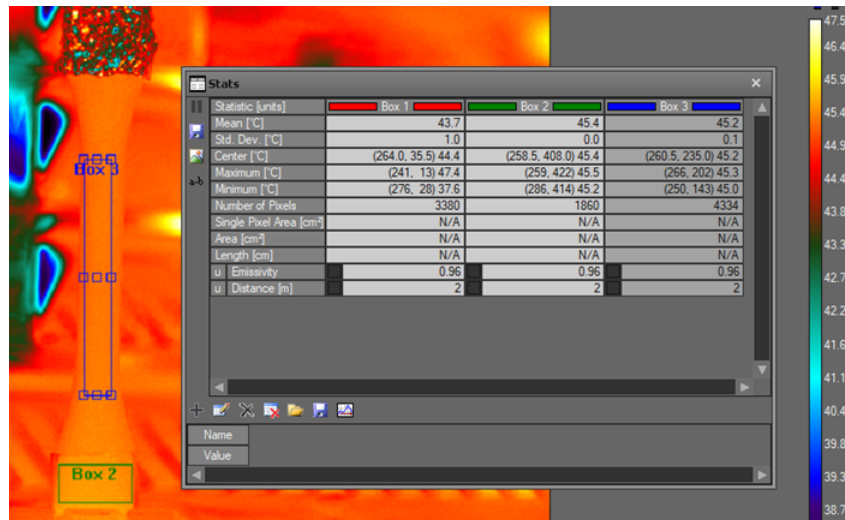


Figure 3.10: Screenshot of the ResearchIR window for one measurement.

### 3.3.3 Static Mechanical Properties

In order to perform the desired fatigue tests, the ultimate tensile strength (UTS) of the materials must be determined. For such purpose, tensile tests were conducted under the ASTM D3039 standard test method [44] at a rate of 2mm/min. To ensure repeatability, five specimens from each stacking sequence were tested. The tests were performed using an Instron 8803 servo-hydraulic machine with a 250 kN load cell and the strain measurements were provided by a video-extensometer.

The test results for the AP and QI specimens are given in Table 3.6 and their stress-strain behavior under static loading is revealed in Figure 3.11. The matrix-dominated nature of the AP specimens is evidenced by the higher strain at failure and by the resemblance to the typical stress-strain curve of polymers. On the other hand, QI specimens present an expected curve for a composite material dominated by carbon fibers.

Table 3.6: Static tensile properties of AP and QI specimens.

|           |         | Dimensions (mm) |           | Maximum Load (kN) | Ultimate Strength (MPa) | Failure Strain (%) |
|-----------|---------|-----------------|-----------|-------------------|-------------------------|--------------------|
|           |         | Width           | Thickness |                   |                         |                    |
| <b>AP</b> | Average | 24.99           | 2.36      | 25.33             | <b>428.98</b>           | 22.81              |
|           | S.D.    | 0.04            | 0.03      | 0.65              | 15.35                   | 0.67               |
| <b>QI</b> | Average | 25.04           | 2.40      | 37.90             | <b>630.75</b>           | 1.30               |
|           | S.D.    | 0.01            | 0.03      | 0.99              | 18.70                   | 0.03               |

### 3.3.4 Preliminary fatigue life tests

Preliminary fatigue tests to determine the fatigue life under different loading conditions are needed to optimize the data capturing in subsequent tests, which will be further explained in Section 4.2.

Regarding the geometry of the specimens, no consensus has yet been reached for fatigue testing of composites. Several researchers reported that the rectangular geometry proposed by the ASTM

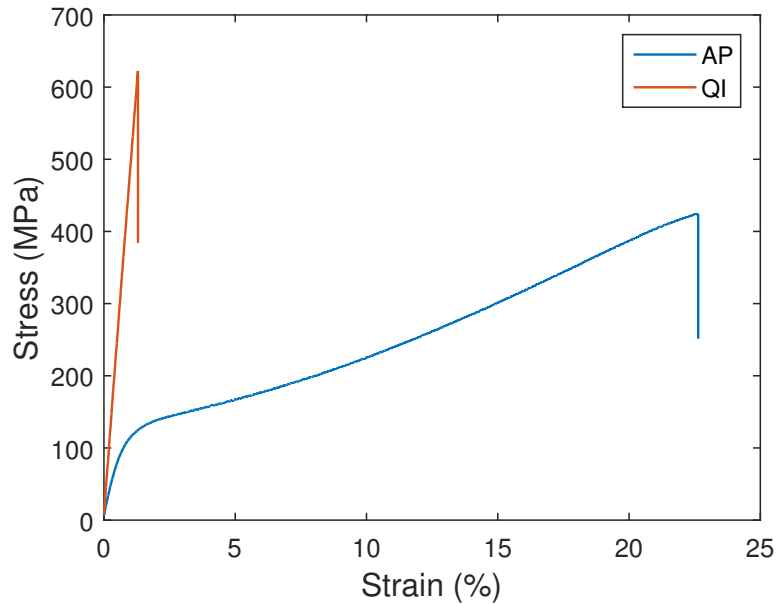


Figure 3.11: Stress-strain curves of AP and QI specimens under static loading.

D3479/D3479M [45] standard test method for tension-tension fatigue of PMCs (Figure 3.12(a)) might not be adequate [10, 46]. Curtis et al. [10] observed that rectangular specimens tested at frequencies above 5Hz failed near or within the gripping area, giving unsatisfactory results. Such observations can be explained by the stress concentrations that exist in the gripping area due to the clamping of the specimen. To overcome this problem, the proposed solution consists of forcing the stress concentrations to happen in the central region. This can be achieved by means of a specimen with area reduction (dog-bone), which is translated into an increase in the effective stress, making failure more likely to occur in that region. Since the present work aims to study the fatigue behavior also at high frequencies, dog-bone specimens become a necessity. With the lack of acceptable standardized guidelines for composite materials in fatigue, the final geometry and dimensions of the test specimens were adapted from the ASTM D638 standard test method for tensile properties of plastics [47], as the fatigue behavior is expected to be dominated by the thermoplastic matrix, and are shown in Figure 3.12(b).

Tension-tension fatigue tests were conducted using an Instron 8803 servo-hydraulic machine with a 250 kN load cell in load control mode. It is important to note that a single test per loading condition was performed, since the goal is to have a rough estimate of fatigue life without the need for repeatability. Several conditions were tested in order to find the best combination of loads and frequencies that would allow the test to finish within a typical workday (8h). Fatigue life results for the AP and QI laminates are presented in Table 3.7 and Table 3.8, respectively.

Initially, a considerable number of specimens were discarded while trying to achieve a proper dynamic response, especially at the highest frequencies (8-10Hz). The main problems encountered were over- and undershooting in the load amplitude and high instability in the loading sine-wave, revealing a poor frequency response, and preventing the tests from starting or running smoothly.

The first approach to overcome those issues consisted of decreasing the frequency and the max-

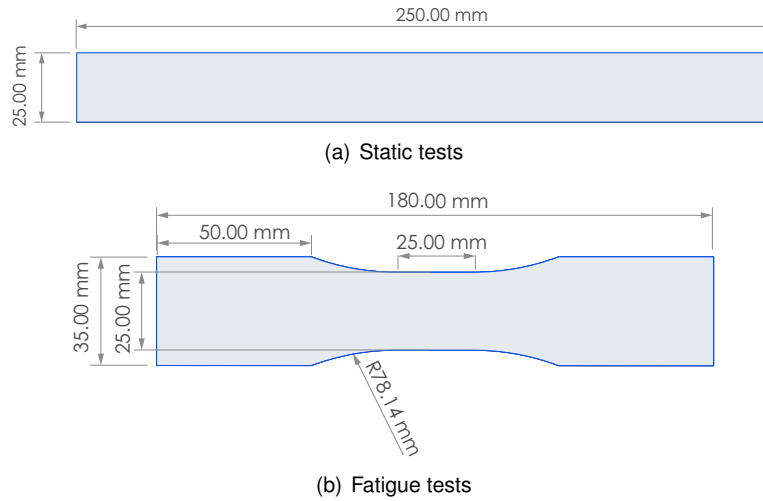


Figure 3.12: Geometry and dimensions of the specimens used for mechanical testing.

Table 3.7: Fatigue loading conditions for the AP laminate.

| % UTS | Frequency (Hz) | Load Ratio ( $\frac{\sigma_{min}}{\sigma_{max}}$ ) | Cycles to Failure |
|-------|----------------|--|-------------------|
| 65    | 5              | 0.25   | >126 340*         |
| 80    | 8              | 0.25   | 110 536           |
| 70    | 10             | 0.1  | 407               |
| 70    | 2              | 0.1  | 56 851            |

\*test paused before failure.

Table 3.8: Fatigue loading conditions for the QI laminate.

| % UTS | Frequency (Hz) | Load Ratio( $\frac{\sigma_{min}}{\sigma_{max}}$ ) | Cycles to Failure |
|-------|----------------|---|-------------------|
| 85    | 10             | 0.1   | 77 469            |
| 75    | 10             | 0.1   | >156 241*         |
| 95    | 10             | 0.1   | 3 205             |
| 95    | 2              | 0.1   | 7 238             |

\*test paused before failure.

imum load. However, the frequency with which the specimen presented a satisfactory response was below 1Hz, which would be prohibitive in terms of testing times. After extensive trial and error, the first successful test was achieved by increasing the load ratio from 0.1 to 0.25 (increasing the minimum load and decreasing amplitude). With such configurations, no more over- and undershooting happened, indicating that one could attempt higher frequencies and loads by keeping a high load ratio (first two rows of Table 3.7). However, the dynamic response was still not ideal and further attempts to improve it were made. By performing an adequate tuning (refer to Section 4.1.3 for detailed explanation), the specimen presented a smooth response without significant initial instabilities, which led to the decision of lowering the load ratio to 0.1 again, so that the number of cycles to failure would decrease, and consequently the testing times as well. This new approach allowed the test to run without issues and reasonable results were achieved. Additionally, it was verified that the fatigue life results for the current AP laminate (PEKK matrix) are similar to the ones obtained for an AP laminate with a PEEK matrix by Al-Hmouz [48].





# Chapter 4

## Methodology

### 4.1 Experimental setup

The experimental setup for the fatigue tests is shown in Figure 4.1. The equipment and methods used for performing the tests and capturing data are discussed in the following sections.

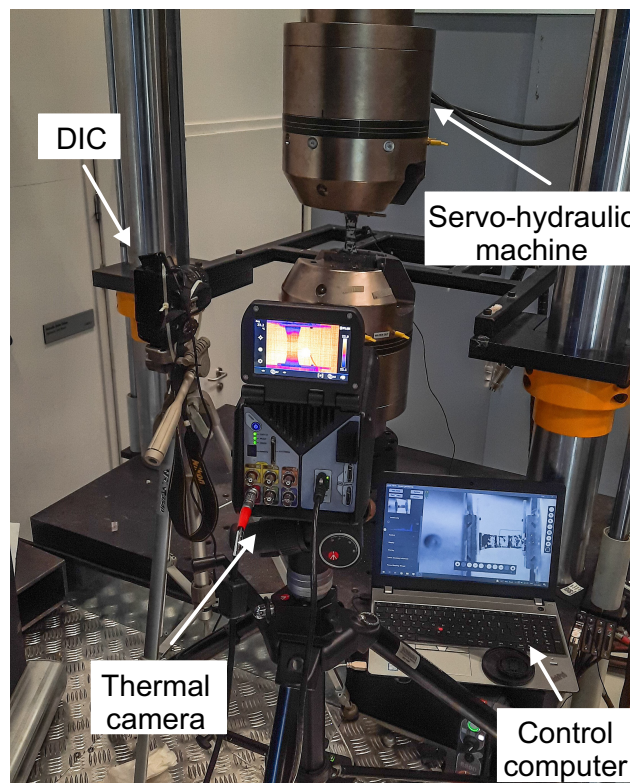


Figure 4.1: Fatigue tests experimental setup.

#### 4.1.1 Digital Image Correlation

Digital Image Correlation (DIC) is a class of non-contact methods and a non-destructive structural health monitoring technique that provides full-field deformation measurements. The experimental pro-

cedure consists of acquiring images of an object under deformation, storing them in digital form and performing an analysis to obtain the variables of interest (displacement, rotation, strain, etc...). The working principle is based on the comparison of a reference image (undeformed state) and a deformed state. To perform this comparison, the surface of the specimen must present a stochastic high contrast pattern, so that there is a unique correlation of pixels from one image to the other. After matching the elements, any change in their position is compared to the reference image, and the quantities related to the motion of the specimen can be computed. An illustration of this process is depicted in Figure 4.2.

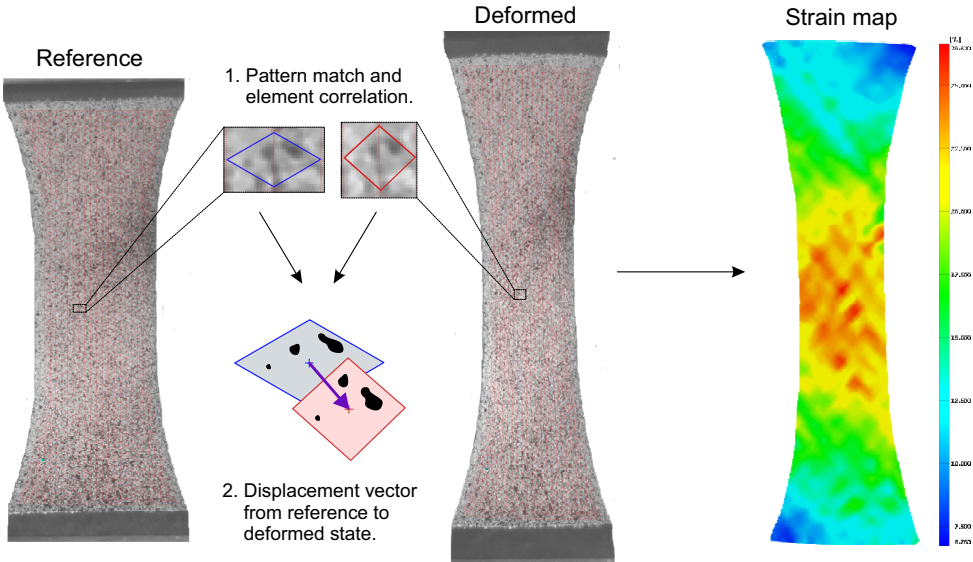


Figure 4.2: Schematic of the DIC working principle.

DIC is an advanced measurement technology that presents numerous advantages over traditional strain measurement methods, such as extensometers. Among them are the full-field representation of quantities in two and three dimensions, non-contact nature that does not require instrumentation of the sample and monitoring the behavior of both very large and microscopic components in split-second dynamic events and long quasi-static tests. Another important feature is that different strain formulations (engineering, logarithmic, Lagrange) can be obtained, which is especially useful in the case of finite strains [49]. For such reasons, DIC is becoming a trusted technique for aerospace applications. It has been successfully included in NASA’s Shell Buckling Knockdown Factor Project to characterize the full-field displacement behavior of launch-vehicle structures and validate buckling simulations [50], and also monitor the deformation of helicopter blades at high rotational speeds with sufficient accuracy for posterior aerodynamic analyses [51].

The aforementioned advantages and the inadequacy of other methods available prompt DIC to be the ideal option for strain measurement. However, The conventional DIC system in the research center exhibited some limitations for high frequency loadings and, hence, an alternative was required. Figure 4.3 summarizes various alternative strain measuring methods available and their limitations.

Since the main issue with the conventional DIC system was an insufficient speed to capture images in high frequency fatigue tests, the replacement of the camera should eliminate the problem. There are faster DIC cameras available in the market, but their high cost made it impossible to rely on that

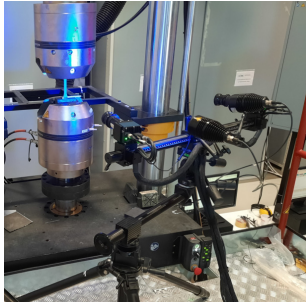

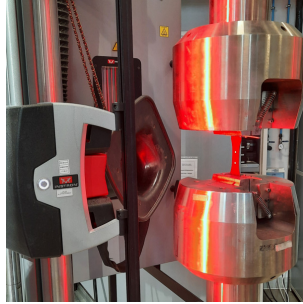
| TRADITIONAL DIC   | DYNAMIC EXTENSOMETER   | VIDEO EXTENSOMETER   |
|---|--|--|
|    |   |    |
| <ul style="list-style-type: none"> <li>✗ Does not capture enough frames per second;</li> <li>✗ Even at lower fps, some frames are dropped.</li> </ul> | <ul style="list-style-type: none"> <li>✗ Measurements limited to strains of 20% (not suitable for angle-ply);</li> <li>✗ At higher frequencies, slippage occurs, yielding wrong data.</li> </ul> | <ul style="list-style-type: none"> <li>✗ Bright red lights shining directly on the thermal camera, interfering with temperature measurements.</li> </ul> |

Figure 4.3: Strain measurement methods and their limitations.

option. Instead, in what concerns the image acquisition stage, there is no reason to exclude DIC from being performed using virtually any digital camera. There are reports of studies using low-cost systems with smartphones [52] and non-scientific graded digital single-lens reflex cameras (DSLR) for polymers undergoing large deformations [53] and for fatigue testing [54], but to the best of the author's knowledge, none of them explore the subject of high frame rates for sub-cycle measurements. As expected, the development of a new experimental procedure for DIC has its challenges and additional factors that need to be considered, as opposed to traditional systems that have calibration, control, acquisition and post-processing fully integrated in one interface. After carefully analyzing the influence of each factor in the implementation and the quality of results [55], the selected hardware and software parameters for the developed DIC system are stated in Table 4.1.

Table 4.1: DIC parameters.

|                       |                   |
|-----------------------|-------------------|
| Camera type           | Nikon D3400       |
| Lens                  | Nikkor 50mm f/1.8 |
| Image size (px×px)    | 1920 × 1080       |
| Video frame rate (Hz) | 59.94             |
| Aperture              | 1.8               |
| Shutter speed         | 1/500             |
| ISO                   | 800               |
| DIC software          | GOM Correlate Pro |
| Facet size (px)       | 22                |
| Point distance (px)   | 19                |

A diagram containing the main steps of the process is shown in Figure 4.4 and explained in further detail below.

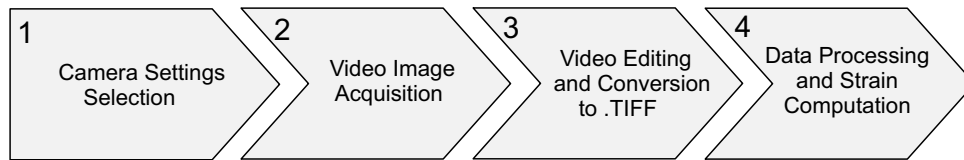


Figure 4.4: Schematic of the experimental DIC process.

1. The developed system consists of a DSLR camera with a fixed focal length lens, that ensures enough zoom to be placed at a reasonable distance from the specimen and minimal distortion. Also, the main advantage of this camera is that it records video at nearly 60 fps, which can give sub-cycle data points at the highest frequency test. In addition to a high frame rate, it is of the utmost importance that the shutter speed is fast enough to eliminate motion blur so the images are sharp and focused. However, with such shutter speeds, the image tends to be too dark and should be compensated with the minimum aperture value (more light entering the sensor) and increasing the ISO (sensitivity to light) if needed, having in mind that high ISO yields brighter but noisier images. With such precise data acquisition requirements, another detail is that the memory card should also have a high writing speed, or some frames might be undesirably dropped. Finally, the camera was set to shoot in gray-scale as it is traditionally used in DIC.

2. After carefully choosing the best parameters, the camera was mounted on a sturdy tripod and was not touched throughout the test, as any vibration might ruin the position and focus. From that moment on, the camera was controlled remotely using DigiCamControl software, to start and stop recording or to adjust some of the parameters.

3. Once the test is finished, the video files were edited in Adobe Premiere Pro. For most cases, only basic video editing tools were needed, such as straightening, cropping and cutting undesired frames. Nonetheless, it is also possible to make lighting adjustments to certain frames if the outside conditions change drastically (turning on/off the lights in the lab, a cloud blocking the sunlight, etc), since DIC is very sensitive while trying to match the pixels based on their gray levels. The last step is to export the video as a sequence of images, ideally .tiff or other uncompressed formats for maximum resolution.

4. Lastly, the exported images were uploaded to GOM Correlate Pro to perform DIC. Since the acquisition stage was not performed with this software, like the conventional DIC, no calibration took place. Instead, the user must define a reference length in the image so that the deformation measurements are accurately computed. The remaining steps for data processing were followed as per the software's user manual [56]. Full-field strain maps of the specimen's surface were obtained, as well as average values of strain in the loading and perpendicular directions.

#### 4.1.2 Thermal camera

As the temperature is present in the dissipation inequality (Eq. 2.26), its value must be measured during the fatigue test. For consistency, it should be obtained for the full-field of the specimen's surface, similar to strain. Thus, infrared thermography was chosen as the temperature measuring technique. It is defined as the use of a non-contact thermal imaging device to detect infrared radiation that is emitted

by an object and its display as a digital temperature map.

The equipment used comprises a FLIR X6580sc thermal camera with a 50 mm focal length lens. It can perform measurements at a maximum frame rate of 355 Hz, detecting temperature differences smaller than 20 mK with an accuracy of  $\pm 1$  mK. ResearchIR was chosen as the software used to control the acquisition process and analyse the thermal data.

Before starting the measurements, certain parameters must be carefully defined in the software according to the test specifications. Among them are:

- **Frame Rate:** number of images acquired per second and its selection was based on the test frequency;
- **Temperature Range:** the expected interval of temperatures to be measured during the test. If not selected correctly, the zones outside the range will be saturated and the temperature values would be wrong. Another important parameter is the integration time, which will result from the selected range, in conformity with the calibration curves provided in the manual [42];
- **Reflected Temperature:** temperature of the surroundings that is reflected by a non-blackbody specimen and captured by the camera. It can be determined by positioning a piece of aluminum (deemed as a perfect reflector) in the camera's field-of-view (FOV) and reading its apparent temperature;
- **Emissivity:** the value measured for the specimen under study (Section 3.3.2) should be input for accuracy.

Since the captured images contain the whole FOV, a region of interest (ROI) should be defined around the visible surface of the specimen so that the average temperature in the gauge length can be obtained.

### 4.1.3 Servo-hydraulic machine

For the fatigue tests, Instron 8803 and 8853 servo-hydraulic machines with a  $\pm 250$  kN load cell were used. The dynamic loads were imparted in load-control mode, as it is more representative of real-world problems. For synchronicity, the servo-hydraulic machine can be connected to the thermal camera and DIC, which starts the measurements in all equipment through an analog output signal when the target load is reached for the first time.

In what concerns fatigue testing, tuning is an imperative step. It is known as the process of adjustment of proportional-integral-derivative (PID) control parameters to obtain a proper mechanical response. This response is related to the stiffness of test specimens, which can vary over time. Regardless, the performance of the machine should not be affected in the course of a fatigue test. Usually, tuning can be performed by applying load amplitudes within the elastic domain to prevent irreversible damage to the material and is deemed valid for any loading conditions. Some difficulties were encountered for the AP specimens due to its low stiffness and low elastic limit. If the chosen load is much lower than the desired value for the actual test, the tuning is completed successfully, but the frequency

response in other conditions is not guaranteed. As a matter of fact, as soon as the load is increased, the stiffness of the AP specimen changes as it undergoes large plastic deformation and crack initiation, affecting the natural frequency and damping of the system. The values obtained previously are no longer suitable for the current state of the material, causing instability in the machine and eventually halting the test as a safety measure. For this reason, it was concluded after many approaches that it is best to use an extra specimen to perform the tuning at a load level closer to the intended maximum load of the fatigue test, and at the highest frequency. Once the optimal values of the PID controller were found, they were noted and input every time a test was conducted for the same material at loads of the same order of magnitude.

## 4.2 Test procedure

### 4.2.1 Load levels and frequencies

After the preliminary fatigue life tests reported in Section 3.3.4, the final loading conditions for each stacking sequence were chosen. Tests were performed in a combination of two frequencies and two maximum load levels, as indicated in Table 4.2, with two tests performed for each loading condition. The frequencies were selected as a low and a high value to access the time-dependent behavior of the material, while the loads are such that the difference is noticeable (in terms of fatigue life and/or mechanisms involved) and the test does not take more than one day to finish.

Table 4.2: Fatigue loading conditions.

|           |         | 2Hz | 10Hz |
|-----------|---------|-----|------|
| <b>AP</b> | 70% UTS | ✓   | ✓    |
|           | 80% UTS | ✓   | ✓    |
| <b>QI</b> | 85% UTS | ✓   | ✓    |
|           | 95% UTS | ✓   | ✓    |

### 4.2.2 Intervals for data acquisition

The dissipation inequality should be evaluated for the entire fatigue test. A common way of defining the time increments for integration is to divide it cycle by cycle, thus requiring a special focus on the intervals and parameters used for data capturing.

The mechanical work term is related to the stress-strain loading and unloading paths for each cycle. In order to have precise information about these paths, sub-cycle data points must be obtained. The limitations on the number of points were imposed by the DIC camera’s frame rate (60 fps), which allows for a maximum of six points per cycle in the 10Hz tests, as depicted in Figure 4.5. Furthermore, testing conditions that were expected to yield more than a thousand cycles to fail hindered the acquisition of data points for every cycle due to the overwhelming amount of data to store. Thus, measurements were

performed for every  $n = 500$  or  $n = 1000$  cycles, depending on the expected fatigue life inferred from the preliminary tests. Stress values were registered by the servo-hydraulic machine while strains were measured with DIC considering the referred intervals.

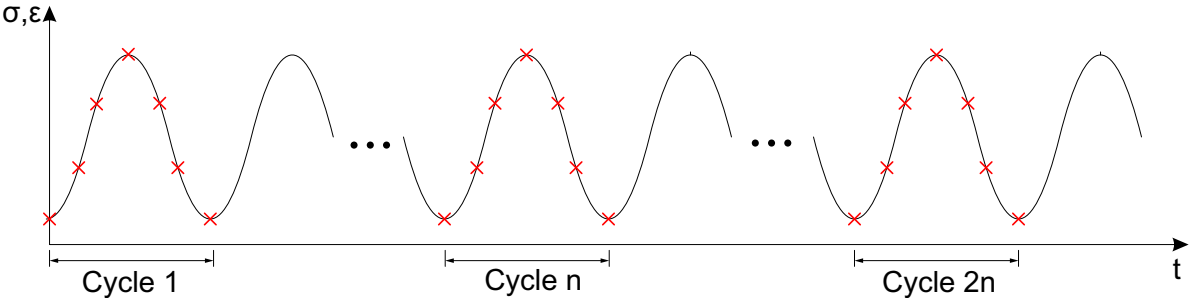


Figure 4.5: Time intervals for stress and strain data acquisition.

Contrarily to the stress-strain behavior, temperature is assumed to be constant in the time span of one cycle. Therefore, the thermal camera’s frame rate was set to be equal to the frequency of the test, capturing a single value per cycle.

### 4.3 Data processing procedure

Following the acquisition stage, data was processed according to Figure 4.6 to finally obtain the entropy generated per cycle,  $\gamma_N$ , and fracture fatigue entropy (FFE).

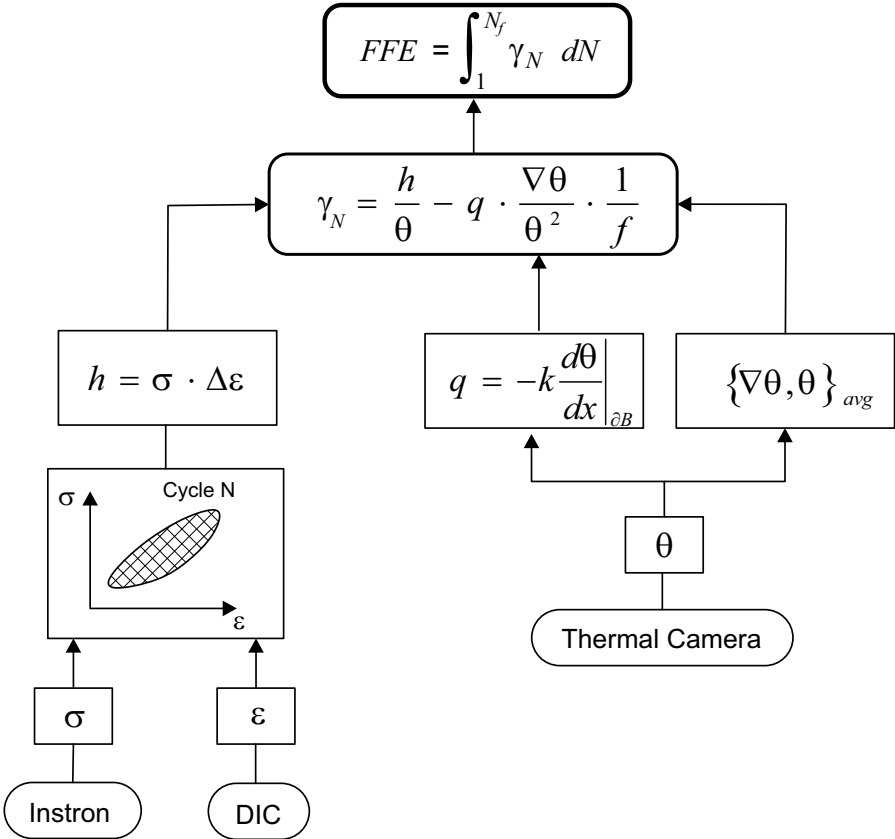


Figure 4.6: Schematic representation of the experimental data processing.

Strain ( $\varepsilon$ ), was measured with DIC, while stress ( $\sigma$ ) was given by the Instron servo-hydraulic machine. In MATLAB, the area within the stress-strain loading and unloading paths for each cycle was computed, corresponding to the hysteresis energy,  $h$ . The thermal camera provided full-field temperature measurements,  $\theta$ , that were used to compute the gradient along the longitudinal direction as well as the average temperature in the gauge section. The term related to heat flux was calculated, where  $k$  is the thermal conductivity and  $f$  is the test frequency, and together with the hysteresis term the entropy generated per cycle,  $\gamma_N$ , is calculated. By integrating the values of entropy calculated from measurements done in the intervals mentioned in Section 4.2.2, with respect to the fatigue life,  $N_f$ , the value of FFE is obtained.



# Chapter 5

## Results and Discussion

In the present chapter, a term-by-term analysis of Equation 2.43 is performed in order to assess their influence on the final entropy values, while providing insight into the mechanical behavior and thermal phenomena under fatigue for carbon fiber/PEKK.

### 5.1 Angle-ply

#### 5.1.1 Fatigue Behavior

Firstly, it is crucial to have a general understanding of the specimens' mechanical and thermal behaviors in fatigue under different loading conditions, in order to best interpret the subsequent entropy results. A qualitative and quantitative description of the phenomena encountered is done for every test case in the following paragraphs.

- **2Hz, 70% UTS**

Fatigue tests at this loading condition were characterized by a high number of cycles to failure (>50 000). During the test, a lack of visible damage for the majority of the fatigue life was noticed, while at later cycles, surface cracks along the fiber direction in the outer layer was observed in different locations. The specimen failed by fiber breakage at both  $\pm 45^\circ$  plies, as shown in Figure 5.1(a). A posterior analysis with optical microscopy revealed damage in the inner layers, mostly in the form of fiber-matrix debonding and matrix cracks. Table 5.1 quantifies the angle between the fibers in consecutive plies, schematically shown in Figure 5.1(b). There was a significant reorientation of the fibers, from the original angle of  $90^\circ$  characteristic of  $\pm 45^\circ$  laminates to a smaller value, as the fibers align towards the loading direction, thus contributing to a post-yield stiffening of the material

In the early stages of the fatigue life, there is an accentuated increase in the mean strain up to 20%, greatly reducing the cross-sectional area (necking). Afterwards, the strain presents a stabilization plateau for most of the life, followed by a sudden increase shortly before failure, as seen in Figure 5.2. The cyclic stress-strain behavior is shown in Figure 5.3a) and is represented by the hysteresis loops, which consist of loading and unloading paths for each cycle. A noticeable feature

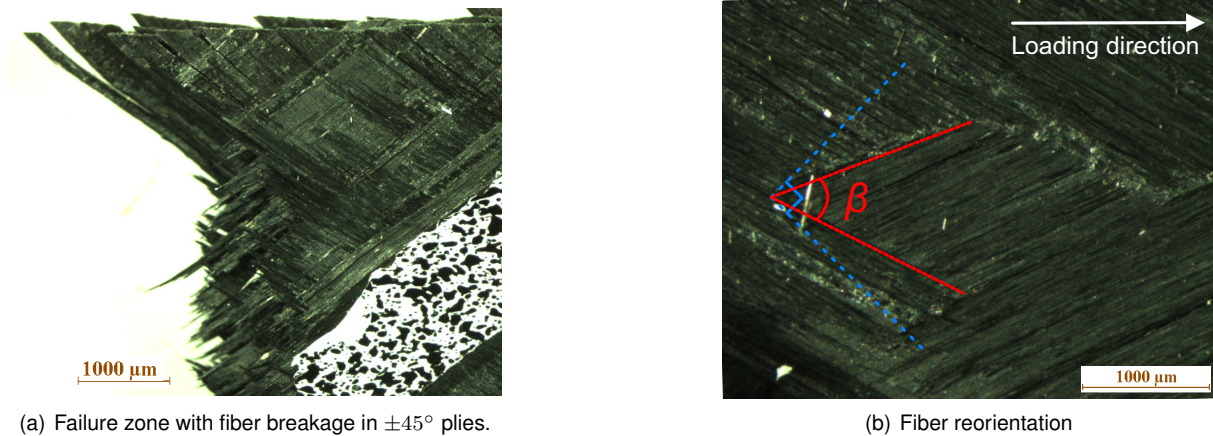


Figure 5.1: Post-mortem optical microscopy analysis in AP specimens.

Table 5.1: Fibers orientation\*,  $\beta$ , after fatigue.

|         | 2Hz | 10Hz |
|---------|-----|------|
| 70% UTS | 61° | 64°  |
| 80% UTS | 52° | 59°  |

\*original angle for a  $\pm 45^\circ$  laminate is  $90^\circ$ .

in all cases is that the loops present a continuous shifting along the x-axis. This phenomenon is called strain ratcheting or cyclic creep, and occurs when a material is subjected to an asymmetric cyclic load, where the non-zero mean stress causes a progressive accumulation of plastic strain. However, a decreasing ratcheting rate is observed, as the loops become almost overlapped after a certain amount of cycles and strain accumulation ceases (plastic shakedown), which is characteristic of a severely cyclic hardened material [57]. This hardening took place in the first cycles as the yield surface shifts in the stress space while the applied load gradually approaches the target value, meaning that higher stresses are needed to enter the plastic regime. Nonetheless, in the last stage of fatigue life, ratcheting starts increasing until failure, which may be related to damage accumulation and degradation of material properties. The behavior under these loading conditions resembles such of a polymer under creep, with well defined primary (transient), secondary (stationary) and tertiary (unstable) creep stages.

The hysteresis loops stem from the mechanisms beyond ideal linear elasticity, such as viscoelasticity and plasticity, leading to energy losses in the material (hysteresis) that can be quantified by the area enclosed within the loops. The evolution of dissipated energy alongside with the average temperature of the material is presented in Figure 5.4a). The large strain achieved during the first cycles translated into a high initial plastic-work induced dissipation that caused an increase in temperature to  $100^\circ\text{C}$ . Due to hardening, the energy generated due to irreversible deformations decreases during the material's lifetime, which coupled with the low loading frequency, allows for the material to exchange energy with the environment. This resulted in cooling followed by a thermal equilibrium maintained until failure.

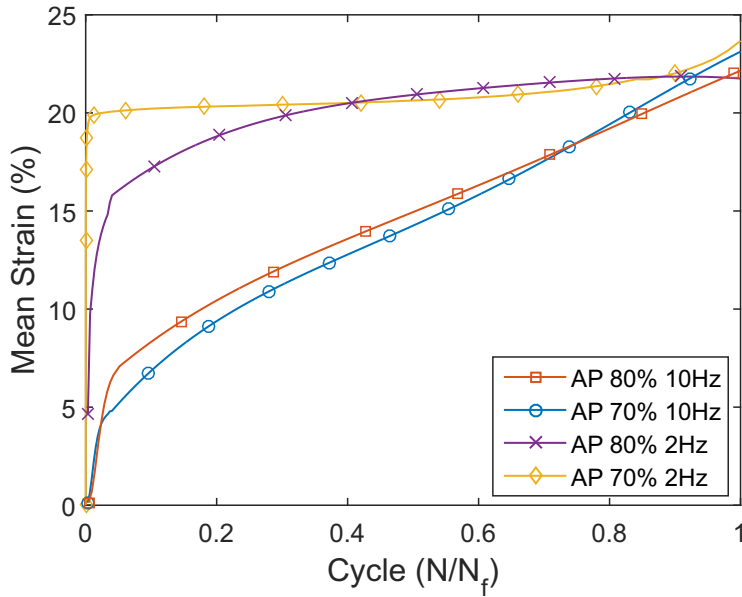


Figure 5.2: Mean strain evolution with normalized cycles for the different test conditions in AP specimens.

- **2Hz, 80% UTS**

By increasing the load level at the same frequency, a drastic reduction in fatigue life (to  $\approx 300$  cycles) was verified. In this case, the onset of damage occurred very early in the fatigue life and consisted of surface splitting. It was observed during the test that the density of cracks in the surface was steadily increasing until the moment of fiber breakage and failure. Furthermore, the higher load level led to more rotation of the fibers, as seen in Table 5.1.

The mean strain shown in Figure 5.2 presented a sharp initial rise followed by a gradually slower increase until failure. The absolute value of strain achieved at failure is lower than the 70% UTS case, which may be linked to the damaged induced short fatigue life that hindered the development of more strain. In fact, the mean strain stabilizes for a slightly higher value than the previous case, though it fails prematurely without presenting the typical tertiary stage of strain increase. For this reason, the shape and time evolution of the hysteresis loops in Figure 5.3b) are identical to the 70% UTS', with all the considerations about ratcheting and hardening holding true, except for the current absence of the last stage.

In what concerns the energy dissipation by hysteresis, it can be seen from Figure 5.4b) that a decreasing trend in energy generation per cycle is verified again. However, the value of cyclic dissipated energy is higher, mainly due to the larger stress and strain achieved but also caused by the increased damage generation rate. Lastly, the temperature evolution is identical to that of the first stage of the previous case, hitting the  $100^{\circ}\text{C}$  mark with failure occurring shortly afterwards. Such observation combined with the considerations about the stress-strain behavior confirms the likeness of the two cases at 2Hz, and damage accumulation as the differentiating factor and source of premature failure for the 80% UTS case.

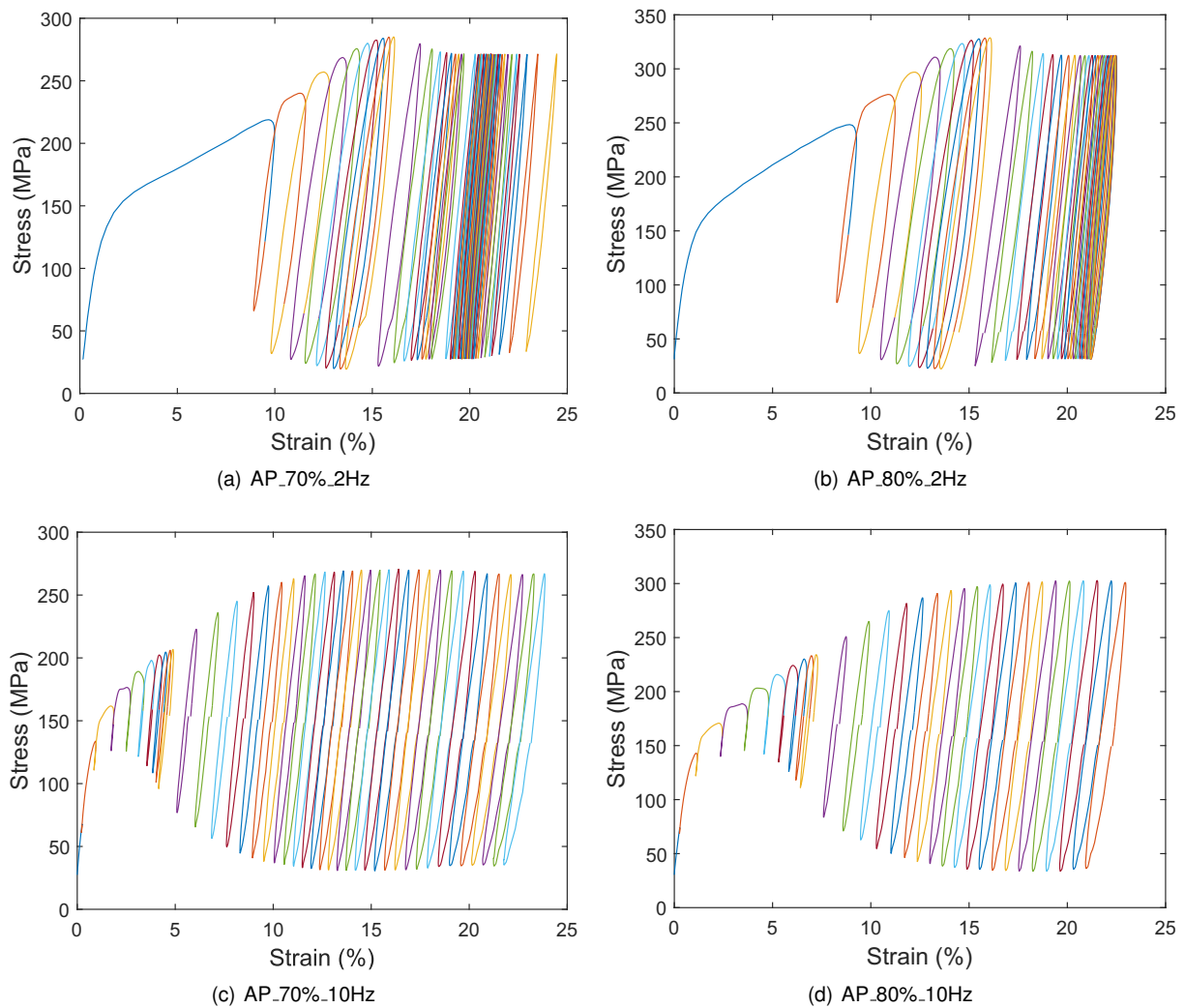


Figure 5.3: Hysteresis loops for the AP specimens (loops for the first 10 cycles and every 10 cycles are depicted).

- **10Hz, 70% UTS**

When compared to the fatigue test at the same load level but lower frequency, an abrupt reduction in fatigue life from 50 000 to 350 cycles was observed. Surface splitting initiated from the edges during the second half of fatigue life, and smoke coming from the specimen due to the fatigue-induced heating was detected at the onset of fracture. The fracture zone presented a brush-like pattern consisting of extensive delaminations, with more severe damage than the 2Hz specimens. Matrix cracking and fiber-matrix debonding were also detected as well as fiber breakage in the failure site. Moreover, fiber reorientations for the 10Hz tests are not as accentuated as the ones at a lower frequency (vide Table 5.1).

Referring to Figure 5.2, a difference in the strain behavior between 2Hz and 10Hz is noticeable. Although the final strain is within the same range, the accumulation of plastic strain occurs without a stabilization zone, happening at a high rate on an initial stage, followed by a slower increase until failure. This is characteristic of the previously mentioned ratcheting behavior, evidenced by the continuous shifting of the hysteresis loops in Figure 5.3c). Another prominent distinction between

the two frequencies lies in the stress-strain response of the first ten cycles. In this case, the response is more instantaneous with lower strains per cycle, resembling that of an elasto-plastic material. The observed difference between tests at a different frequency, is partially justified by the rate-dependent behavior of the PEKK matrix, since a higher loading rate translates in less time for the material to undergo deformation under the same applied stress level. Aside from that, the lower strains also stem from the low applied loads in the first cycles. For both cases, the loads do not reach the desired value as the test begins. Yet, the higher frequency aggravated the instabilities in the dynamic response of the servo-hydraulic machine, causing even lower stress levels and more time to readjust.

For the 10Hz frequency, the energy dissipation manifested by the loops area follows an opposite trend to the one observed for 2Hz, as seen in Figure 5.4c). Since plastic strain is accumulating at a constant rate and the stress amplitude is constant for most of the test, the increase in the hysteresis energy cannot be explained by dissipation due to plastic work alone. Instead, it is likely related to thermal effects since the high loading frequency combined with the low thermal conductivity of the PEKK prevents energy due to irreversible phenomena from dissipating to the environment, thus leading to adiabatic heating. The subsequent increase in temperature is stored in the system as internal energy that is also reflected in the hysteresis area as per Eq. 2.19. This hypothesis is supported by the linear temperature rise from start to failure, attaining average values around the glass transition temperature ( $T_g = 160^\circ\text{C}$ ). This excessive heating softens the matrix material, provoking a loss of stiffness and integrity of the material. At later stages, a slight decrease in the energy dissipation is noted, which is believed to arise from the change in physical properties and constitutive behavior of the material above  $T_g$  [19].

- **10Hz, 80% UTS**

The test and the highest frequency and stress level presented an expected reduction in fatigue life to  $\approx 200$  cycles. However, it was not as extreme as in the 2Hz case. All the occurrences mentioned in the [10Hz, 70%] case about damage and fiber reorientation were also verified for this loading condition.

Analogously to the relation between the two 2Hz scenarios, Figure 5.2 shows that the 80% case exhibits a similar evolution of mean strain to the 70%, presenting higher values throughout the test, though a lower failure strain was attained due to the shorter fatigue life. Naturally, the similarities extend to the ratcheting behavior and hysteresis loops depicted in Figure 5.3(d).

The dissipated energy follows an increasing trend like the previous case, as shown in Figure 5.4(d), with higher absolute values due to increased stress-strain and damage-induced dissipation. Furthermore, it does not exhibit the last declining stage since the specimen failed before reaching the glass transition temperature, although autogenous heating phenomena accompanied by a linear temperature rise are still present.

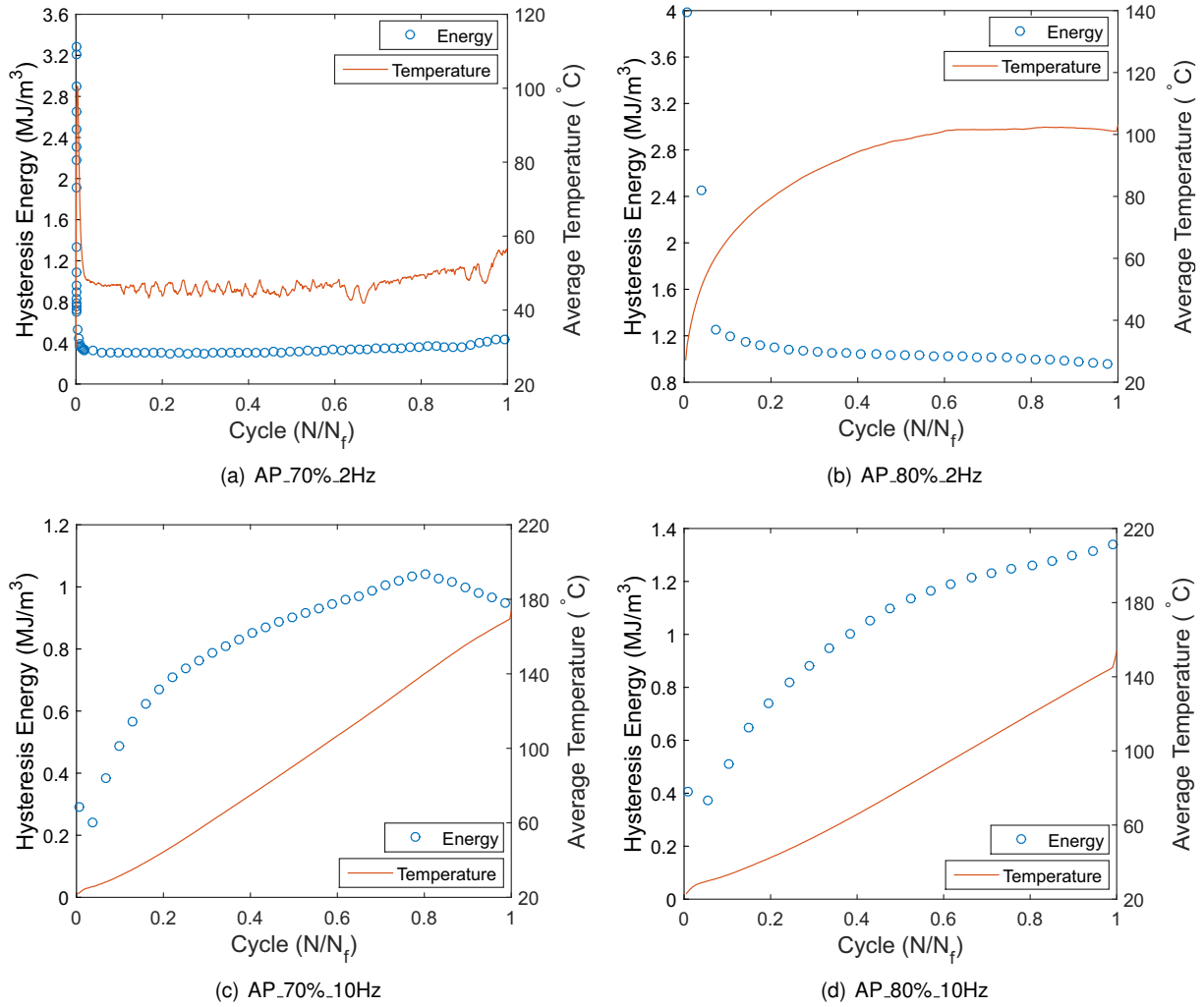


Figure 5.4: Hysteresis energy and temperature evolution for the AP specimens.

The main conclusion from this analysis can be summed up as the material exhibiting a considerable rate-dependent behavior, activating different dissipation mechanisms according to the loading frequency. Also, higher frequency proved to have a detrimental effect on fatigue life due to the self-heating phenomena. It is once again confirmed that the response of the AP specimens is dominated by the PEKK matrix, as it resembles a thermoplastic polymer rather than a typical fiber-reinforced material.

### 5.1.2 Hysteresis Entropy

In the present thesis and in line with the majority of FFE related literature, the viscoplastic work term in Eq. 2.25 is approximated by the hysteresis energy. Naturally, the dissipative phenomena related to hysteresis generate entropy and the analysis in Section 5.1.1 could be done for entropy likewise.

Figure 5.5(a) and (b) show the hysteresis entropy generation with cycles for the tests at 2Hz and 10Hz, respectively. Although the energy has been divided by temperature, the overall trend stays unchanged. The effect of frequency is noticeable once more, as there is an opposite entropy evolution trend between 2Hz and 10Hz. Also, less entropy is being generated each cycle in the 70% cases when compared to 80%, as expected.

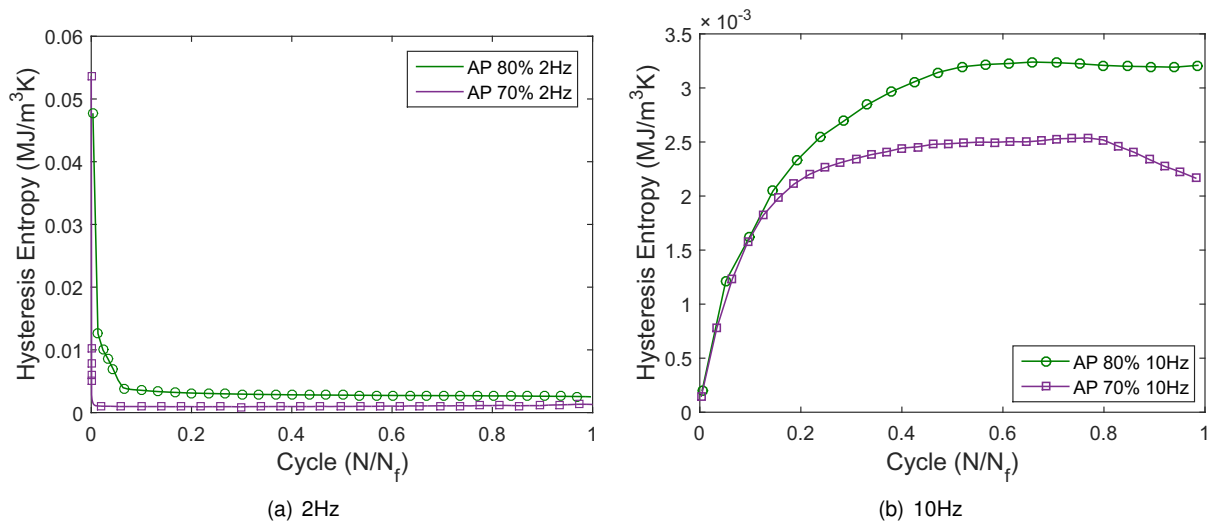


Figure 5.5: Entropy generated due to hysteresis in AP specimens.

### 5.1.3 Thermal Dissipation Entropy

During the fatigue test, heat flows from the specimen to the machine grips by conduction. Using Fourier's law, the heat flux per unit area  $q_k$  is quantified. The dependence of thermal conductivity with temperature is accounted for using the results from Section 3.3.1. Also, the temperature gradient is taken at the end of the gauge section, as the Clausius-Duhem inequality states that entropy is generated from heat crossing the system's boundaries. Figure 5.6 shows the temperature profile along the specimen for one cycle of the [10Hz, 70%] case, from which a function  $\theta = \theta(x)$  can be fitted and the respective gradient at  $x = L/2$  computed.

The evolution of entropy flow due to the heat flux is shown in Figure 5.7. However, this term can be assumed negligible since its order of magnitude ( $10^{-5}$ ) is lower than the hysteresis entropy's ( $10^{-3}$ ). For this reason, the results obtained in the previous section are considered to represent the total entropy generation, proving that hysteresis prevails over heat conduction for composites even with large temperature gradients.

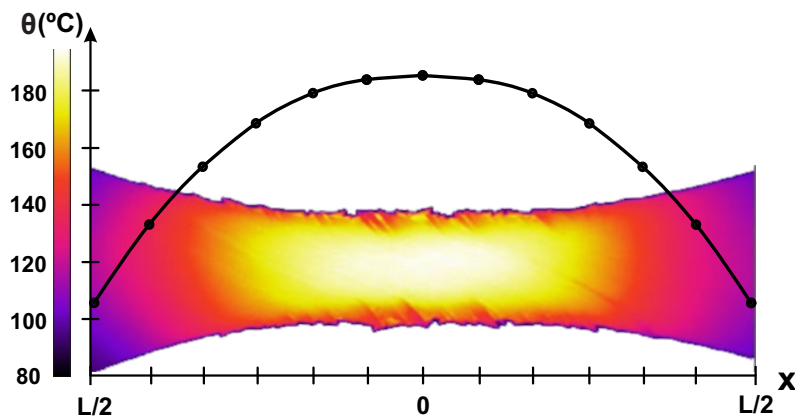


Figure 5.6: Temperature profile of the AP\_70%\_10Hz case for  $N/N_f=0.9$ .

Since the case chosen for this analysis is the one presenting higher temperatures, thermal dissipa-

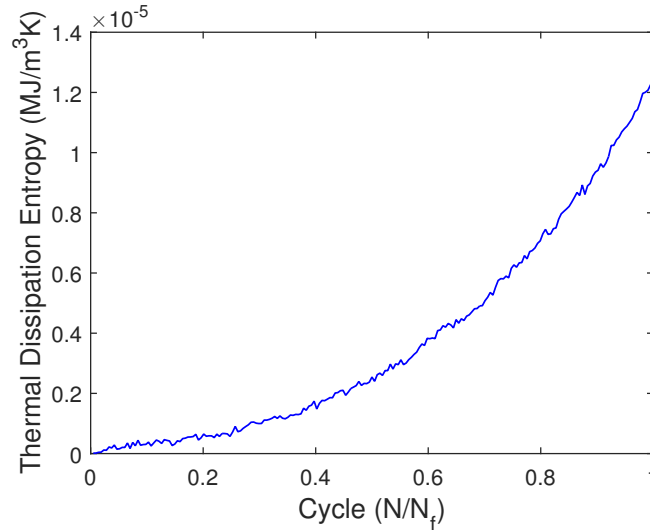


Figure 5.7: Entropy generated due to heat transfer for the AP\_70%\_10Hz case.

tion entropy can be confidently assumed to be negligible for the remaining cases with similar or lower temperatures, as less heat is dissipated by conduction.

#### 5.1.4 Accumulated Entropy

Finally, the accumulation of entropy throughout the test was determined by integrating the generated entropy in the fatigue life. The values at failure (FFE) as well as the fatigue life ( $N_f$ ) of all the performed tests are presented in Table 5.2.

Table 5.2: FFE (MJ/m<sup>3</sup>K) and fatigue life of AP specimens.

|     |       | 2Hz    |        | 10Hz   |        |
|-----|-------|--------|--------|--------|--------|
| 70% | FFE   | 52.52  | 58.98  | 0.7323 | 0.7414 |
|     | $N_f$ | 50 332 | 56 784 | 327    | 334    |
| 80% | FFE   | 0.9976 | 1.0421 | 0.6026 | 0.6224 |
|     | $N_f$ | 299    | 350    | 214    | 221    |

The foremost conclusion taken is that FFE is not constant across all loading conditions. For the majority of cases, the values of FFE present a negligible difference, which would replicate the conclusions drawn in the related literature. However, these cases also present a fatigue life in the same order of magnitude. When the fatigue life increases by over 150 times in the [2Hz, 70%] case, FFE also increases, although non-proportionally. The reason is there are more cycles contributing to the increase in FFE, while the entropy generated per cycle is not sufficiently lower to yield a constant value at failure. Naderi [58] stated that this method has not been investigated and validated for high-cycle fatigue, yet no theoretical limitations were imposed. While the [2Hz, 70%] case might not be consensually defined as high-cycle fatigue, it certainly presents some resemblance, such as the low plastic strain accumulation for most of the fatigue life. Nonetheless, the difference in the number of cycles to failure between this case and the remaining was considerable, which did not happen in the several studies performed by



Naderi where a constant FFE was said to be verified. Naturally, the absence of a universally constant value at failure denotes that the usefulness of FFE for fatigue life prediction in thermoplastic composites might be at stake.

In order to have a better understanding of the observed discrepancy in FFE, a plot of the accumulated entropy vs cycles for one test of each loading condition is shown in Figure 5.8. It can be inferred from the [2Hz, 80%] and [10Hz,70%] cases that more cycles do not always yield a higher FFE. Instead of a directly proportional relationship, there is rather a distinguishable trend in the evolution of the accumulated entropy. Tests performed at 2Hz present a negative curvature, i.e., a decreasing rate of entropy accumulation, while at 10Hz the opposite is verified. Also, the 80% UTS cases accumulate entropy at a higher rate for both frequencies. Different rates are a necessary condition to have a similar value at failure for different fatigue lives, which may derive from different stress- and strain-rates imposed by the loading frequency and stress level or phenomena associated with damage. For this material, however, the rates are not different enough to yield such results, evidencing the need for an approach that includes or excludes the contribution of other terms, as further discussed in Section 5.3.

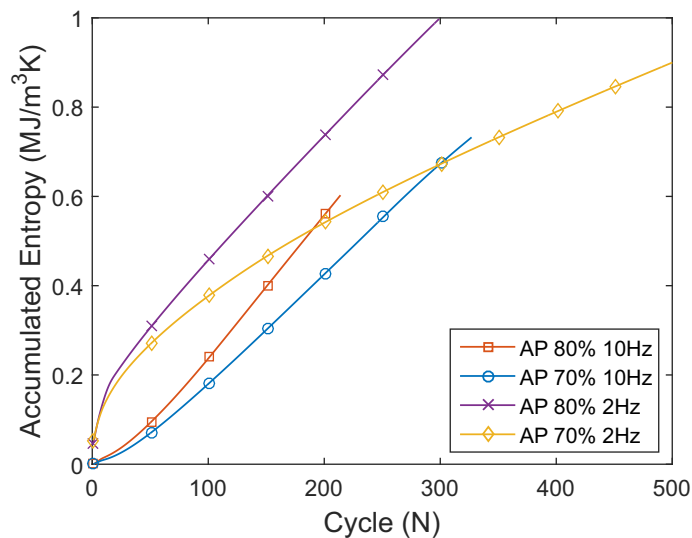


Figure 5.8: Accumulated entropy through the cycles in AP specimens.

Another factor that hinders the possibility of using FFE to predict the fatigue life of the AP laminate is the fact that the equation  $\frac{N}{N_f} = \frac{\gamma}{FFE}$  only holds true if the relationship between normalized life with normalized accumulated entropy is linear. It has already been proven to be the case for metals [58], but no evidence of such relationship in composites was given. In fact, it can be concluded from Figure 5.9 that it is far from being linear and not every test case follows the same trend.

### 5.1.5 Infinitesimal vs Finite Strain Theory

A remark should be made for the AP stacking sequence discussing the consequences of considering an infinitesimal strain formulation. As seen in the previous section, the material undergoes large plastic deformations of up to 25% at failure. Although such value is considered to be in the realm of finite strains,

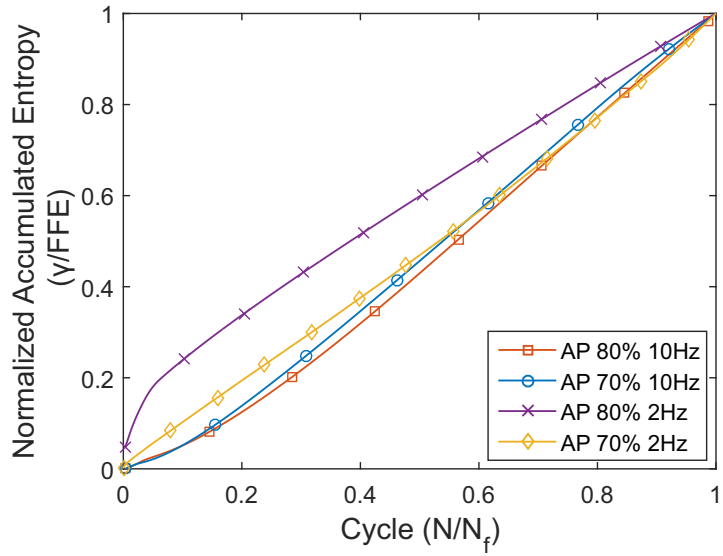


Figure 5.9: Normalized accumulated entropy through the fatigue life in AP specimens.

the strain amplitude per cycle does not surpass 2%, justifying the initial use of a small deformation approximation for simplicity.

For reference, Figure 5.10 shows the time evolution of the Green-Lagrange strain,  $\mathbf{E}$ , (finite) and its linearized version,  $\varepsilon$  (infinitesimal or engineering strain), which present an increasing divergence as larger strains are achieved. Furthermore, the strain calculated using the Lagrangian formula presents a larger amplitude (difference between the upper and lower values for each curve).

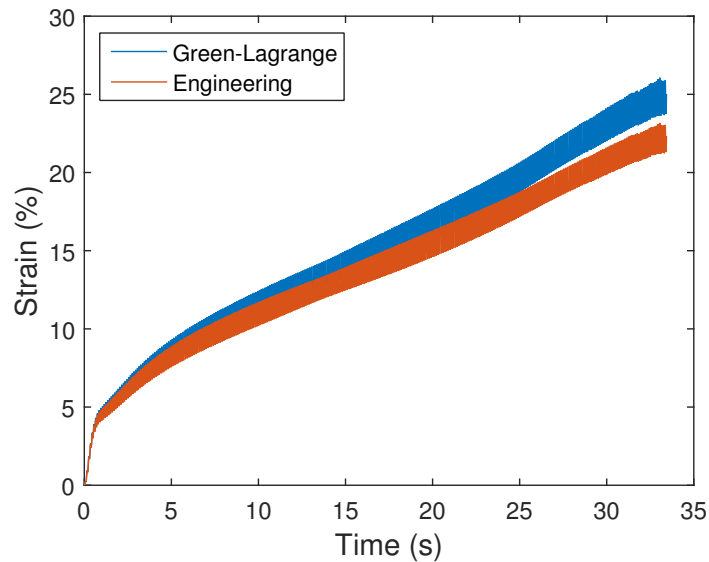


Figure 5.10: Time evolution of Green-Lagrange and engineering strain.

The entropy was recalculated using the formulation derived with finite strain theory in Eq. 2.25 and the new values of FFE ( $\mathbf{F}^{-1}\mathbf{P} \cdot \dot{\mathbf{E}}$ ) alongside the previous ones ( $\sigma \cdot \dot{\varepsilon}$ ) are presented in Table 5.3.

The FFE values of the loading conditions that yield a short fatigue life are not greatly affected by the infinitesimal approximation. However, the test that lasted 50 000 cycles shows a considerable difference

Table 5.3: FFE (MJ/m<sup>3</sup>K) calculated with infinitesimal vs finite strain theory.

|            |       | 2Hz                           |  | 10Hz                          |  |
|------------|-------|-------------------------------|--|-------------------------------|--|
|            |       | $\sigma \cdot \dot{\epsilon}$ | $\mathbf{F}^{-1}\mathbf{P} \cdot \dot{\mathbf{E}}$ | $\sigma \cdot \dot{\epsilon}$ | $\mathbf{F}^{-1}\mathbf{P} \cdot \dot{\mathbf{E}}$ |
| <b>70%</b> | FFE   | 52.52                         | 44.12  | 0.7323                        | 0.7321   |
|            | $N_f$ | 50 332                        |  | 327                           |  |
| <b>80%</b> | FFE   | 0.9976                        | 1.001  | 0.6026                        | 0.6023   |
|            | $N_f$ | 299                           |  | 214                           |  |

in FFE. This is due to the fact that the accumulation of error from the approximation propagated through a much higher number of cycles, translating into an inaccurate end result. Regardless, this source of error does not have an impact on the conclusions drawn about the non-constancy of FFE in the previous section and its usefulness. For the alternatives discussed further in Section 5.3, it might be worth taking the aforementioned remarks into account for higher accuracy, especially if an entropy-based criteria is to be implemented in computational simulations.

## 5.2 Quasi-isotropic

### 5.2.1 Fatigue Behavior

For the quasi-isotropic stacking sequence, the analysis of the fatigue behavior is to be done in a general sense rather than case-by-case, since few significant differences were observed.

The damage visible to the naked eye during the course of the tests was mostly in the form of delaminations towards the end of life and similar for all cases, in a rather stochastic fashion with no apparent correlation to specific mechanisms or test variables. Nonetheless, imaging by optical microscopy revealed that the 2Hz cases have more evenly distributed damage along the specimen, whereas for 10Hz, it is localized mostly in the failure zone. Also, it is worth mentioning that, contrary to the AP specimens that failed completely by separating into two pieces, the QI laminates remained as one. Such is explained by failure occurring due to the final fiber fracture only in the outer 0° plies. Also fiber breakage in the  $\pm 45^\circ$  laminae, failure of 90° plies by matrix cracking and delaminations were observed, as shown in Figure 5.11.

The effect of increased frequency for the QI laminate proved to be beneficial to fatigue life, in opposition to the findings for AP specimens. Lower frequencies yield shorter fatigue lives with more damage accumulation, as stated above. Similar results in the literature linked the beneficial effect of frequency with the blunting of crack tips caused by creep, halting their propagation [8]. However, the existence of a threshold frequency that would lead to the same problems encountered in AP specimens is expected, where autogenous heating would surpass the mentioned advantages.

Regarding the mean strain evolution, Figure 5.12 shows a similar trend for all cases with an accentuated rise in the very early stages of the fatigue life, to a posterior region of slow and steady increase, with higher values for the higher load level. Moreover, the higher magnitude of viscoplastic deformation

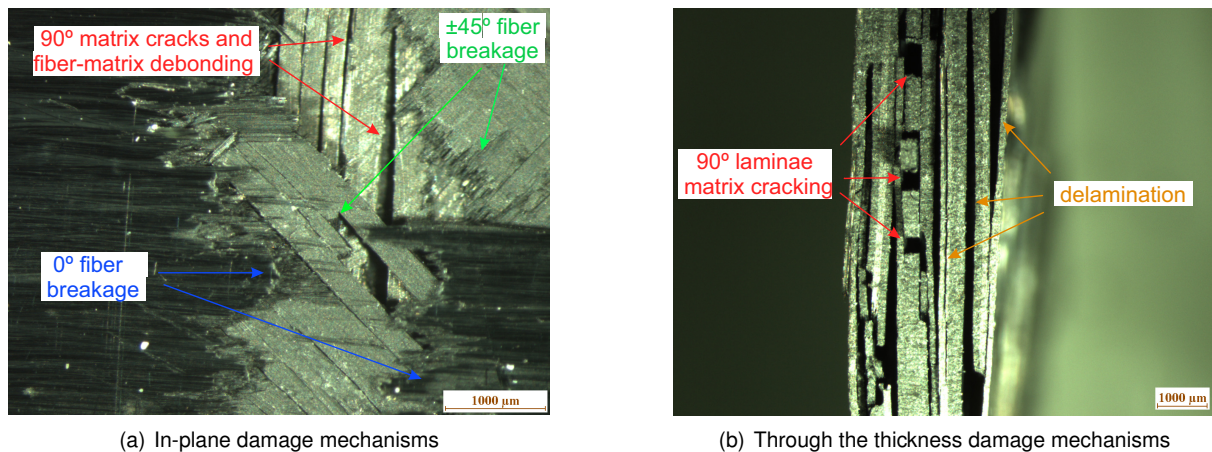


Figure 5.11: Post-mortem optical microscopy analysis in QI specimens.

accumulated during the first loading cycles for the 2Hz cases reveals the rate-dependent behavior of the laminate introduced by some of the off-axis plies in uniaxial loading. Nonetheless, the magnitude of strains attained for the QI is considerably smaller in comparison with the AP.

The hysteresis loops in Figure 5.13 are almost overlapping with a small shift in the x-axis throughout the entire test, indicating that non significant ratcheting occurs. Figure 5.14 shows the cyclic hysteresis energy and temperature evolution, which is identical for all cases. A decreasing trend independent of loading frequency and stress level with a steeper decay within the first stages of life can be observed. This initial evolution agrees well with the trends of stiffness and temperature evolution in polymer composites where matrix cracking is expected to be more pronounced. The subsequent stabilization of the hysteresis energy is characteristic of a plastic shakedown situation where the material underwent hardening, and the dissipation by irreversible deformation mechanisms tends to vanish. Although more plastic deformation is verified for the 2Hz cases, the magnitude of stabilized dissipated energy is higher for 10Hz. Since the average temperature is also higher for the latter, it may be an indication that internal friction may be the source of such additional energy generation. Lastly, the areas inside the hysteresis loops are smaller than the AP's, which indicates that most dissipation is originated in the matrix, and it is not as pronounced when fibers are being axially loaded.

## 5.2.2 Hysteresis Entropy

Similarly to the comments in Section 5.1.2 for the AP stacking sequence, the entropy generated due to hysteresis shown in Figure 5.15 follows the same trend as the hysteresis energy. Furthermore, the hierarchy of absolute values is maintained, with more entropy being generated per cycle for the higher load at the same frequency level, and for the higher frequency at the same load level. Still regarding the absolute values of energy, it is observed that QI specimens generate less entropy than their AP counterparts, which underlines the prevailing role of the matrix in dissipative phenomena.

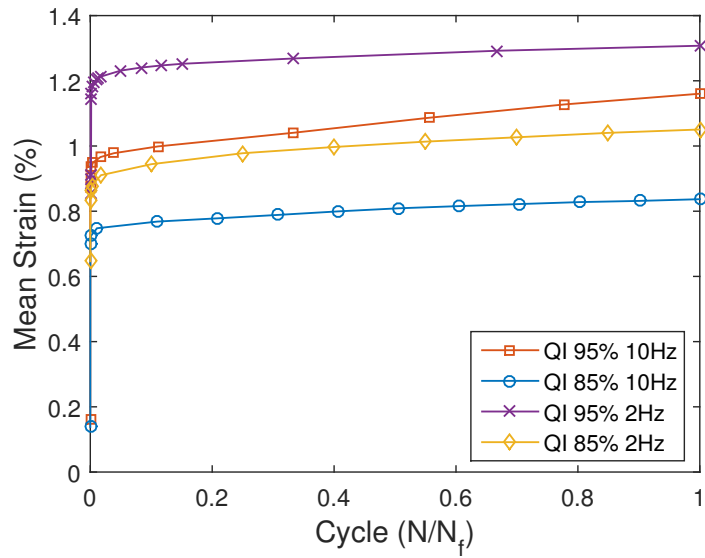


Figure 5.12: Mean strain evolution for the different test conditions in QI specimens.

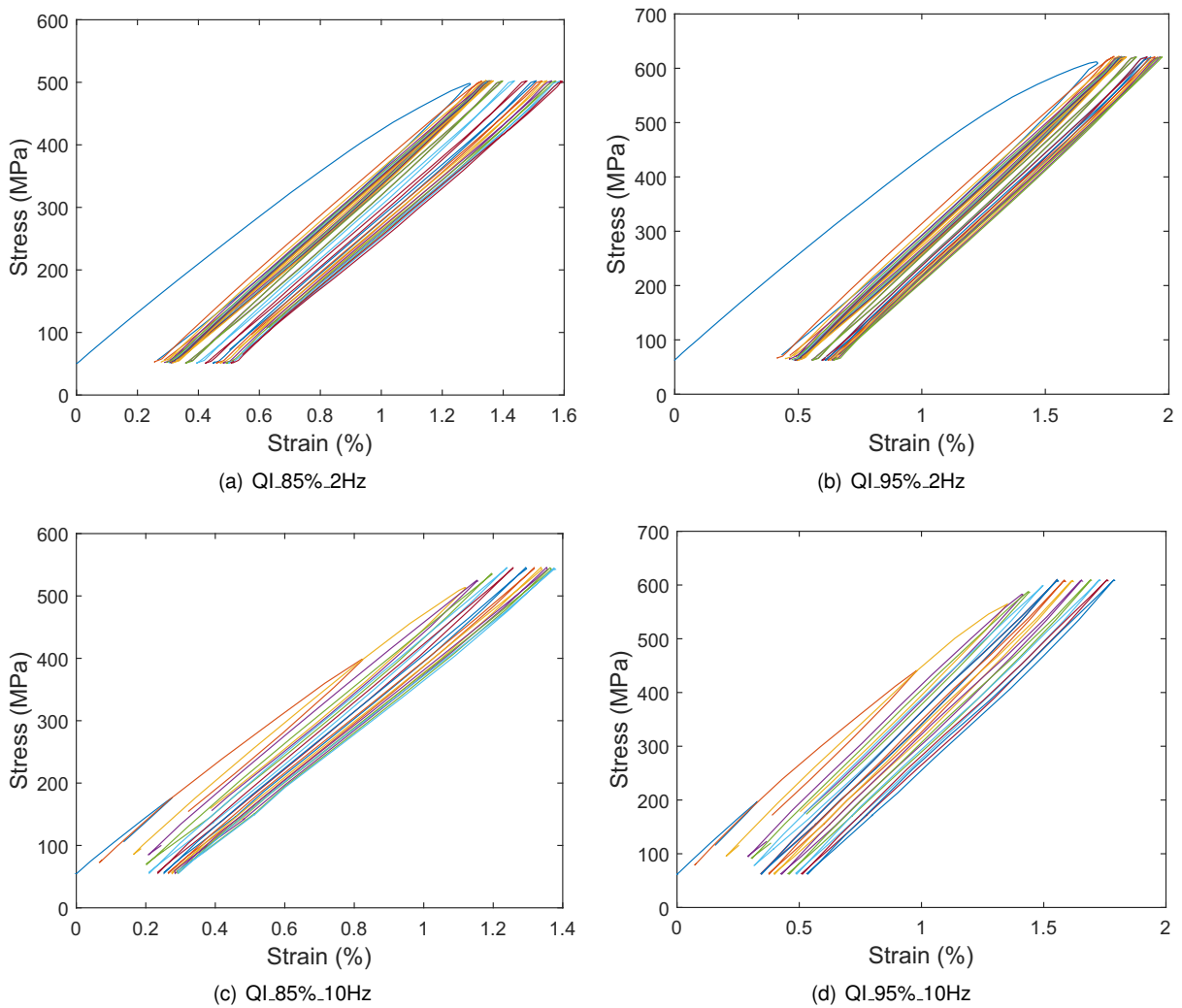


Figure 5.13: Hysteresis loops for the QI specimens.

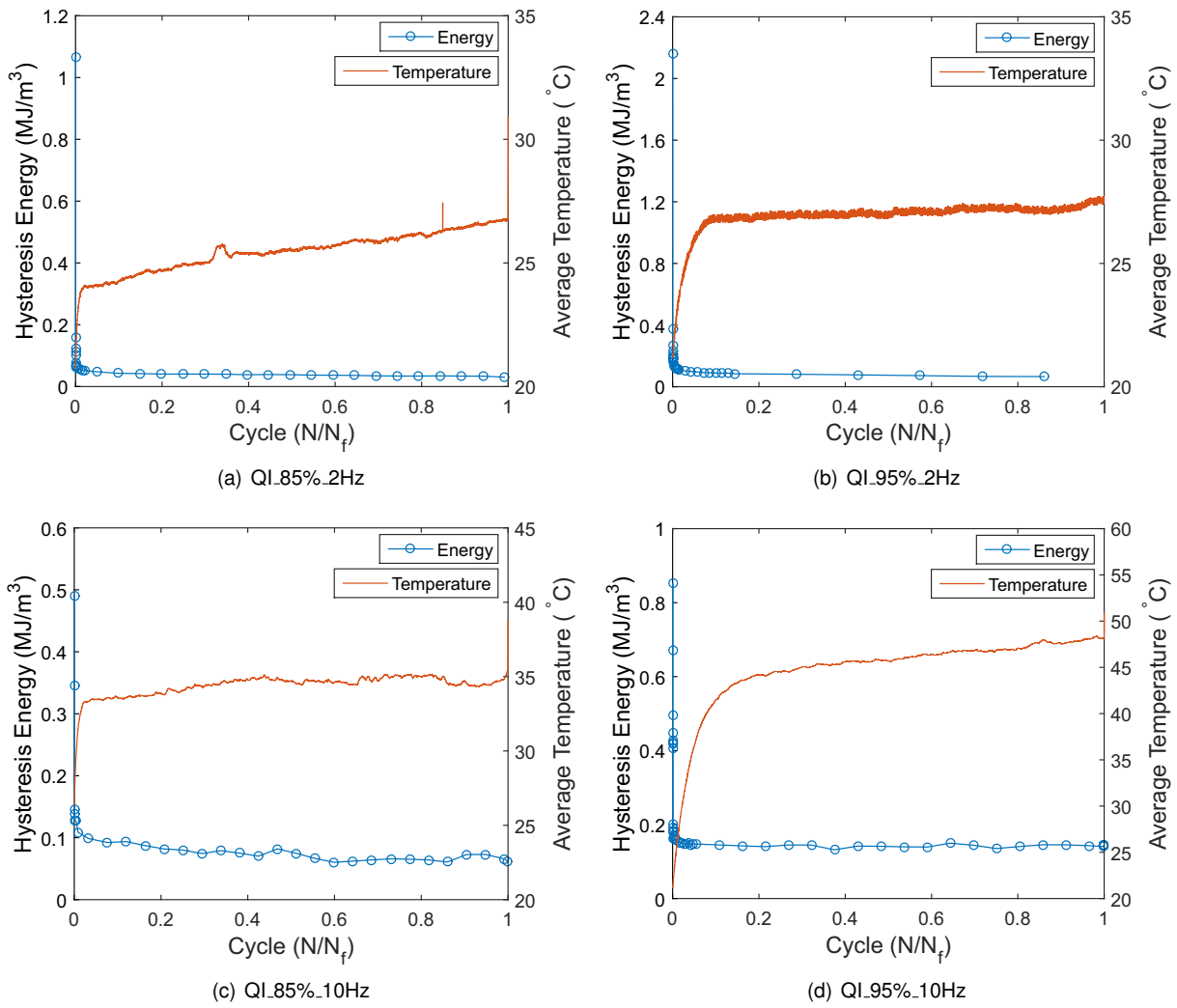


Figure 5.14: Hysteresis energy and temperature evolution for the QI specimens.

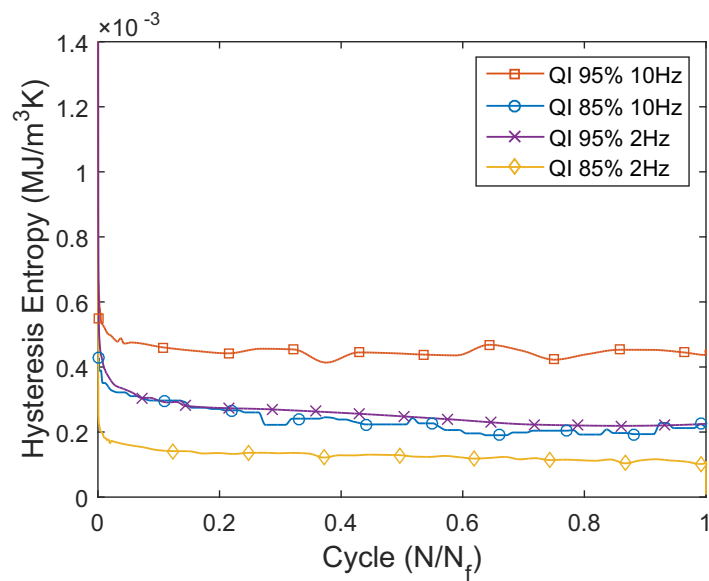


Figure 5.15: Entropy generated due to hysteresis in QI specimens.

### 5.2.3 Thermal Dissipation Entropy

For this stacking sequence, the assumption of negligible entropy due to heat transfer is not guaranteed since the hysteresis entropy is now one order of magnitude below the APs. By following the same procedure as Section 5.1.3, the temperature profile of the [10Hz, 95% UTS] case is shown in Figure 5.16 and the entropy production due to heat conduction is presented in Figure 5.17.

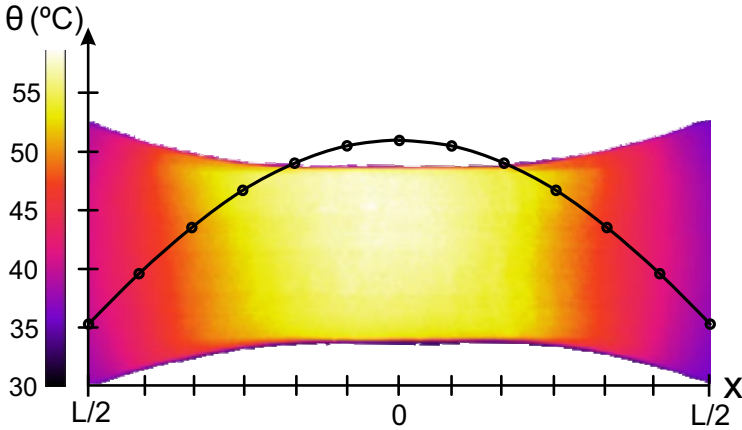


Figure 5.16: Temperature profile of the QI\_95%\_10Hz case for  $N/N_f=0.9$ .

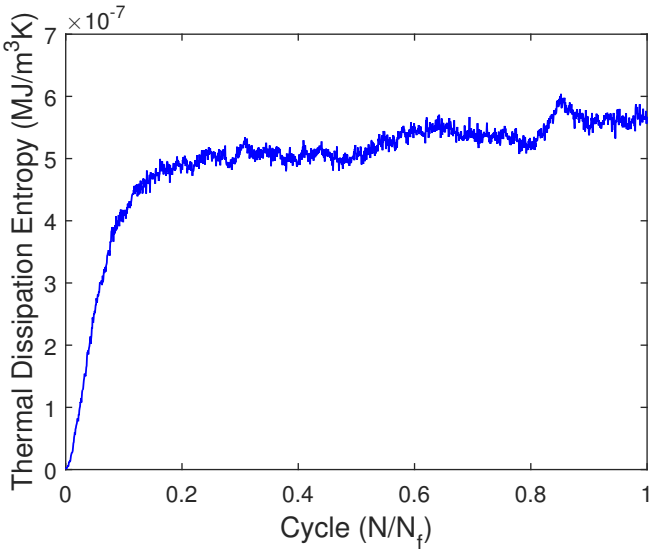


Figure 5.17: Entropy generated due to heat transfer in the QI\_95%\_10Hz case.

With the lack of autogenous heating phenomena, the temperature inside the specimen is distributed more evenly, leading to lower temperature gradients. Consequently, thermal dissipation entropy in QI specimens is also assumed to be negligible.

### 5.2.4 Accumulated Entropy

For the QI laminates, the values of FFE and fatigue life for all tests performed are displayed in Table 5.4. It can be concluded once again that FFE is not constant, even for a fiber-dominated stacking sequence.

Table 5.4: FFE (MJ/m<sup>3</sup>K) and fatigue life of QI specimens.

|     |       | 2Hz    |        | 10Hz   |        |
|-----|-------|--------|--------|--------|--------|
| 85% | FFE   | 5.172  | 6.905  | 20.87  | 22.85  |
|     | $N_f$ | 40 352 | 53 871 | 77 479 | 91 813 |
| 95% | FFE   | 0.5504 | 1.783  | 8.382  | 8.759  |
|     | $N_f$ | 2 285  | 6 969  | 18 564 | 19 614 |

However, FFE does not vary linearly with the number of cycles to failure, since tests with a higher fatigue life can present lower FFE. An example is the [2Hz, 85%] vs. [10Hz, 95%] cases, where such difference was expected taking into account the more pronounced dissipative phenomena described in Section 5.2.1 for the [10Hz, 95%] case.

In an effort to further understand this behavior of FFE, the accumulated entropy was plotted against the number of elapsed cycles. From Figure 5.18, a set of features that have never been mentioned in the related literature can be analysed. Firstly, each loading condition yields a different rate of entropy accumulation, with an increase in load and frequency resulting in a higher rate. However, it is still not enough of a difference to match the FFE values for different fatigue lives. For the repeated tests at the same loading condition, the entropy accumulation happens at the same rate, evidenced by the overlapped straight lines, though failure randomly occurs along that line. The two aforementioned findings emphasize the dependence of entropy on the strain-rate, as it is the only common aspect between tests performed under similar conditions that present different fatigue lives. For this reason, it proves that computing entropy and FFE from the hysteresis energy is not a suitable approach for this material, since it does not capture any information about the imminence of failure. Instead, and similar to the conclusion drawn for the AP laminate in Section 5.1.4, more terms in the entropy calculation should be included or removed in an attempt to correct these rates and have a unified FFE value.

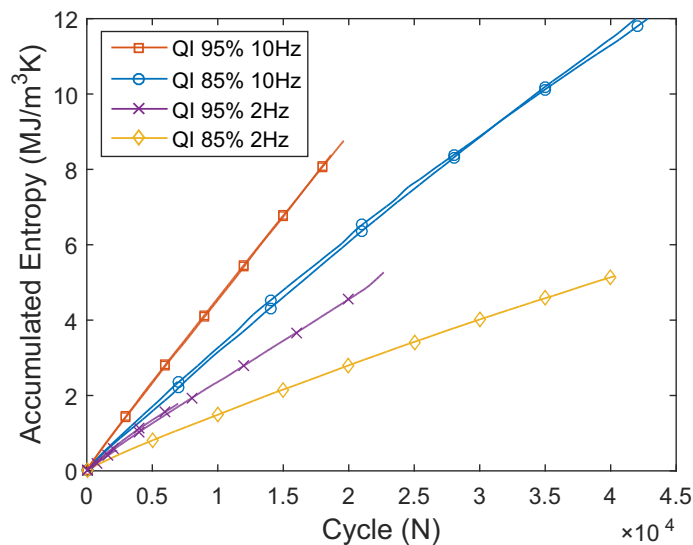


Figure 5.18: Accumulated entropy through the cycles in QI specimens.

Regarding the relationship between the normalized accumulated entropy and normalized cycles,



Figure 5.19 shows that its non-linearity is not as accentuated as in the AP specimens. Only the [10Hz, 95%] case presents a perfectly linear correlation that would allow the application of a failure criteria in the standard form derived in the literature  $\left(\frac{N}{N_f} = \frac{\gamma}{FFE}\right)$ . It is worth mentioning once again that its application would only be possible if a constant FFE is obtained by means of a different approach. For the remaining test cases, the trend is similar among them, though not exactly linear. If a constant FFE is achievable in future work and this trend is still verified, a modification to the failure criteria should be made, or errors would arise depending on the cycle chosen to evaluate the equation and predict the fatigue life. A suggestion is assuming a power-law correlation as  $\left(\frac{N}{N_f}\right)^n = \frac{\gamma}{FFE}$ , where  $n=0.85$  for the mentioned test cases.

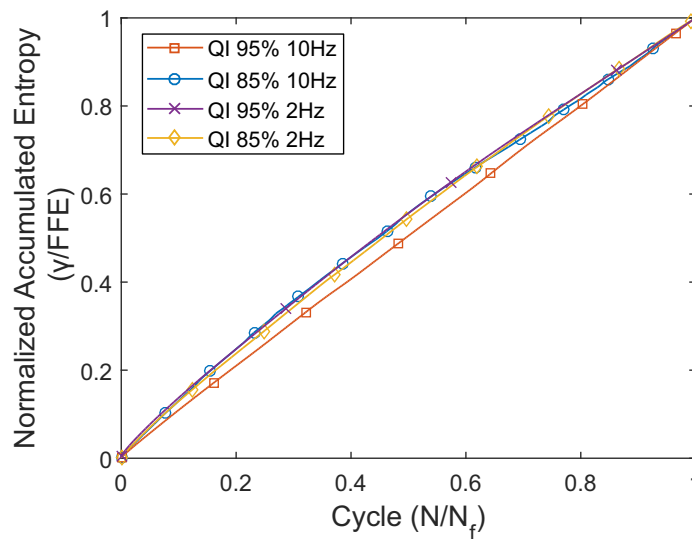


Figure 5.19: Normalized accumulated entropy through the fatigue life in QI specimens.

### 5.3 Entropy as a failure criterion

As it was verified in the previous sections, the entropy calculation approach based on the hysteresis energy and thermal dissipation (although negligible) is insufficient to prove the usefulness of entropy as a failure criterion. The FFE results of all tests performed are plotted against the fatigue life in Figure 5.20, and no constant value can be assumed to exist. This method was previously used in the literature concerning thermoset composites and FFE was considered to be constant, although some error could be noticed. The results of Naderi and Khonsari [23] are replicated in Figure 5.21, where a slight increasing trend of FFE with the number of cycles can be observed. Nonetheless, the FFE values are within a reasonable range, which can be mainly attributed to the similar order of magnitude of the fatigue lives between different cases ( $10^3$ - $10^4$ ), which was not verified in the present thesis. Recalling the comments in Section 5.1.4, Naderi [58] stated that the suitability of the hysteresis method and applicability of FFE has not been tested for high-cycle fatigue cases, not providing a full spectrum of number of cycles to failure. While not disregarding their results, the present work has been able to demonstrate that the proposed approach in [23] is not valid for thermoplastic composites. The root of such difference

with the aforementioned studies on epoxy-based composites can be attributed to the higher sensitivity of thermoplastics to the loading conditions, reflected on the disparate values of fatigue life and entropy generation between different test cases.

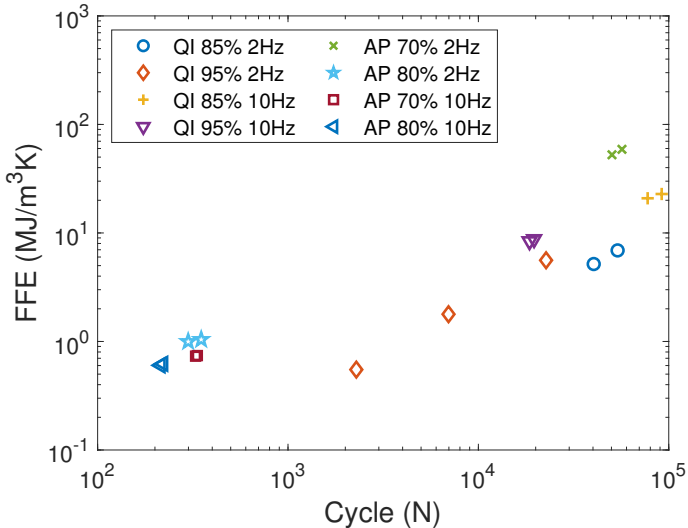


Figure 5.20: FFE vs. fatigue life of the performed tests.

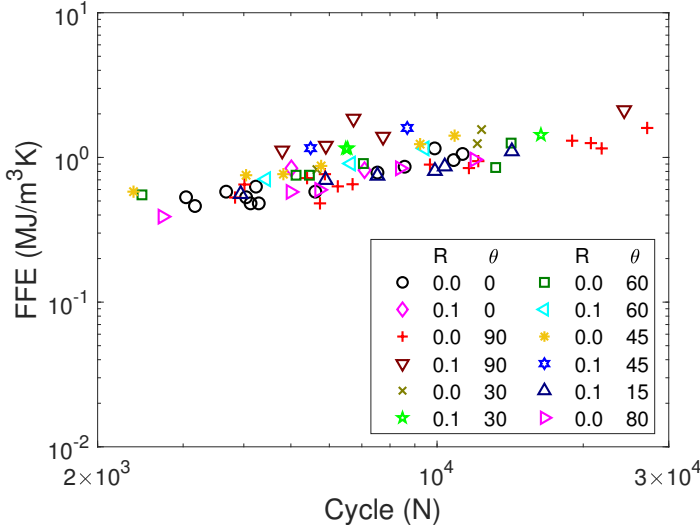


Figure 5.21: FFE vs. fatigue life of the tests performed by Naderi and Khonsari [23].

After the initial works using the hysteresis energy approach that claimed a constant value, advances in the formulation of FFE have been made. Referring to Section 1.3, it became unanimously accepted in the research community that internal friction (IF) is an important source of dissipation but should not be accounted for in the entropy generation as it does not induce damage or irreversible deformations. Only by removing it and considering exclusively the energy dissipated due to plastic flow, a constant value of FFE could be achieved in the related studies. It is known that internal friction, or damping, is manifested by stress-strain hysteresis, and the energy losses associated with it are included in the total hysteresis energy [59, 60]. Naturally, the hysteresis loops area calculated with the experimental stress

and strain values will not only contain the plastic work but also internal friction losses. Since most works that were successful in discarding internal friction contributions were conducted on metals, the shift to composite materials is not straightforward as the phenomena involved are essentially different. The following paragraphs discuss the alternatives to obtain an accurate FFE for thermoplastic composites.

### Internal friction measurement and removal

The rate of entropy accumulation calculated from the hysteresis area is going to be influenced by the energy generated due to internal friction. Removing the contribution of IF is a strategy that would correct the entropy accumulation rate and potentially yield constant FFE values. However, internal friction is a complex set of phenomena which are difficult to quantify and even qualify, more so in the case of composite materials. There are a plethora of ways in which internal friction can be manifested, such as anelasticity, viscous damping stemming from linear viscoelasticity, on the onset of plastic deformation and non-linear damping [59, 61]. Efforts and extensive literature review on the matter were made in order to find a suitable method for removing its contribution, but the overwhelming amount of phenomena related to IF makes it virtually impossible to quantify each one of them.

For metals, a successful example of internal friction removal is the solution proposed by Liakat and Khonsari [25]. The authors determined the phase angle between the applied stress and respective strain,  $\delta$ , which gives a measure of the fractional energy loss per cycle due to anelastic behavior with respect to the strain energy density. By removing the contribution of such energy loss, they were able to obtain a constant FFE. However, De Batist [61] affirmed that " $\delta$  is ill-suited for evaluating non-linear effects, ..., as it is based on the resonance response of the system, which will be distorted in the presence of non-linearity". For this reason, such approach constitutes a special case of IF applicable only to linear elastic materials, not considering the non-linear viscoelastic and viscoplastic nature of polymers. In fact, the procedure proposed by the referred authors was attempted only for the QI specimens, since they present a nearly linear elastic behavior with a well defined Young's Modulus, as opposed to the AP laminate. In that case, the energy dissipated due to IF,  $\Delta W$ , can be computed as per Eq. 5.1, where  $\sigma_0$  and  $\varepsilon_0$  are the stress and strain amplitudes, respectively [60].

$$\Delta W = \pi \sigma_0 \varepsilon_0 \tan \delta \quad (5.1)$$

The value of  $\delta$  was found to be constant for every cycle and the same for every loading condition, thus yielding a value of  $\Delta W$  dependent only on the stress and strain evolution, and consequently the strain-rate. Figure 5.22 compares the accumulated entropy for QI laminates before and after removing the internal friction, where the dashed lines are the corresponding cases from Figure 5.18). It can be observed that the effect of this removal is solely reflected in a proportional reduction of the entropy accumulation rate for all cases. A well-marked dependence on loading conditions is still verified, not affecting the trend of FFE results. Viscoelastic and non-linear effects, mainly due to plasticity, are missing from this formulation of IF energy, which need to be included for accurate results.

An attempt to remove internal friction in epoxy-based composites was made by Huang et al. [29],

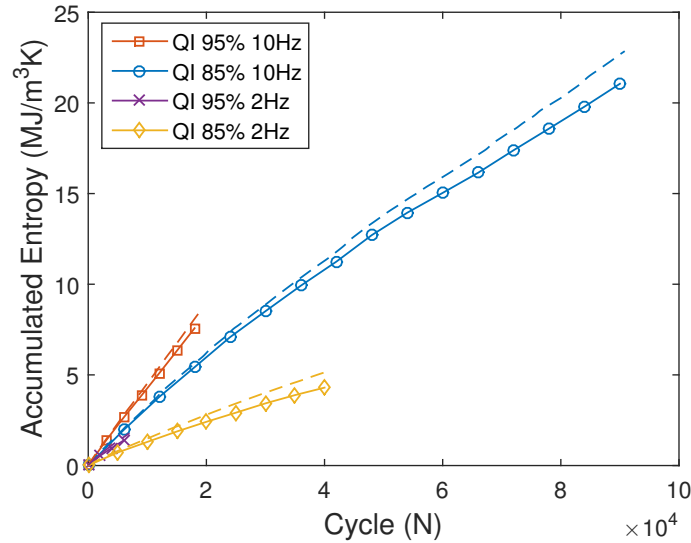


Figure 5.22: Accumulated entropy through the cycles in QI specimens with (dashed line) and without (solid line) the contribution of IF.

following an approach based on the first law of thermodynamics. By stopping the fatigue tests and calculating the temperature cooling rate, the energy dissipated due to internal friction was computed, under the assumption that there is a fatigue limit below which all dissipation is due to non-damaging processes. Also, a constant value of energy generation per cycle is assumed, depending exclusively on the stress level. The results obtained for an epoxy/carbon fiber AP laminate are reproduced in Figure 5.23, for four stress levels at 5Hz. The values of FFE for tests presenting fatigue lives of different orders of magnitude are within an acceptable range (shadowed area in Figure 5.23), though more data is required to fully validate the approach. Since their method is based on a single energy balance performed in the moment of test stoppage, the FFE is calculated directly, instead of a cycle-by-cycle entropy generation value at any stage of the fatigue life. As a matter of course, the usefulness of such approach is compromised since the apparent success in separating the internal friction is not transferable to the monitoring of entropy generation throughout the service life. In fact, the authors demonstrated that FFE could be used for a rapid evaluation of S-N curves, which entails the disadvantages of such fatigue life prediction method in composite materials. Moreover, the practicality might also be at stake, since a set of several preliminary tests is required to determine the fatigue limit and internal friction energy for different stress levels, and presumably for different frequencies in the study of rate-dependent materials.

### Plastic work determination

Since quantifying and removing internal friction phenomena is an extremely difficult task, an alternative is the direct determination of energy dissipation due to irreversible deformations. This can be done by means of a cyclic plasticity model to predict plastic strain evolution or plastic strain energy, instead of the experimental hysteresis area calculated with the total strain. For metals, there are several models available that can accurately describe plasticity in fatigue scenarios. An example is Morrow's cyclic plastic energy dissipation formula [62], implemented by Naderi and Khonsari [34] for the real-time

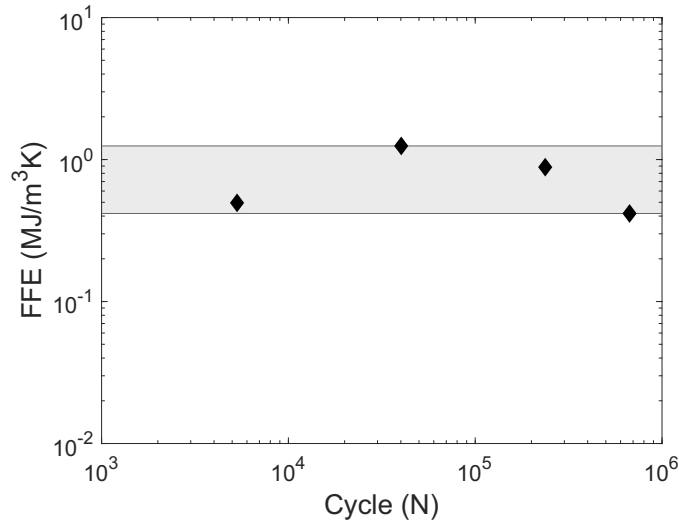


Figure 5.23: FFE vs. fatigue life of the tests performed by Huang et al. [29].

monitoring of entropy and fatigue life prediction to prevent failure, which provided satisfactory results. For composites, the challenge lies in the lack of models that account simultaneously with cyclic loads, viscoelasticity, hardening and eventually large deformations. Also, if the model is validated and adjusted to fit the experimental results using the measured stress and strain, the effect of the total strain-rate dependence might not be fully eliminated, and potentially internal friction effects could still be present. Only a very tailored model for this purpose could yield the desired results, whose complexity is reflected in the sheer amount of cyclic plasticity models for composite materials developed since the beginning of the century.

### Inclusion of other dissipative terms

Another possible source of error is the over-simplification of the Clausius-Duhem inequality. For metals, it is accepted that entropy related to damage phenomena is negligible compared to the plastic work term. However, for composites it has been proven that the evolution of internal variables represents 30% to 50% of entropy generation [30]. While the experimental hysteresis area is an attractive approach due to its simplicity, a more complete method should be used for materials that exhibit accentuated rate-dependent behavior, such as thermoplastic matrix composites.

The inclusion of damage parameters could be important to correct FFE, since the difference in fatigue life is mainly explained by different damage accumulation rates. As a consequence of the degradation of composite materials under cyclic loading, the relation between stress and strain is not single-valued and the stress-strain curves change throughout the fatigue life. Hwang and Han [63] proposed the concept of fatigue modulus to model the degradation of material properties induced by damage. Fatigue modulus is defined as the slope of a line connecting the origin and the peak applied stress in the cyclic stress-strain loops, as illustrated in Figure 5.24. It is assumed to be a function of the number of cycles  $F = F(N)$ ,

and damage can be parametrized as,

$$D(N) = 1 - \frac{F(N)}{F_0}. \quad (5.2)$$

This method assumed isotropic damage and relies on data collected during each fatigue test which greatly simplifies its implementation.

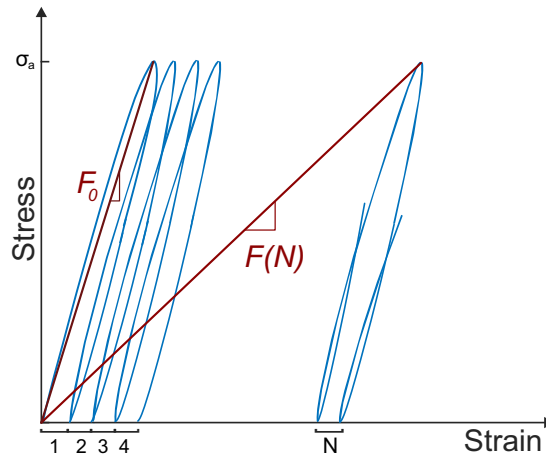


Figure 5.24: Fatigue modulus concept.

The evolution of the fatigue modulus for a representative test case of both AP and QI specimens is shown in Figure 5.25. An inverse power law relation  $F(N) = \left( \frac{1}{aN^b + c} \right)$  is verified across all loading conditions, where  $a$ ,  $b$ , and  $c$  are test case dependent coefficients.

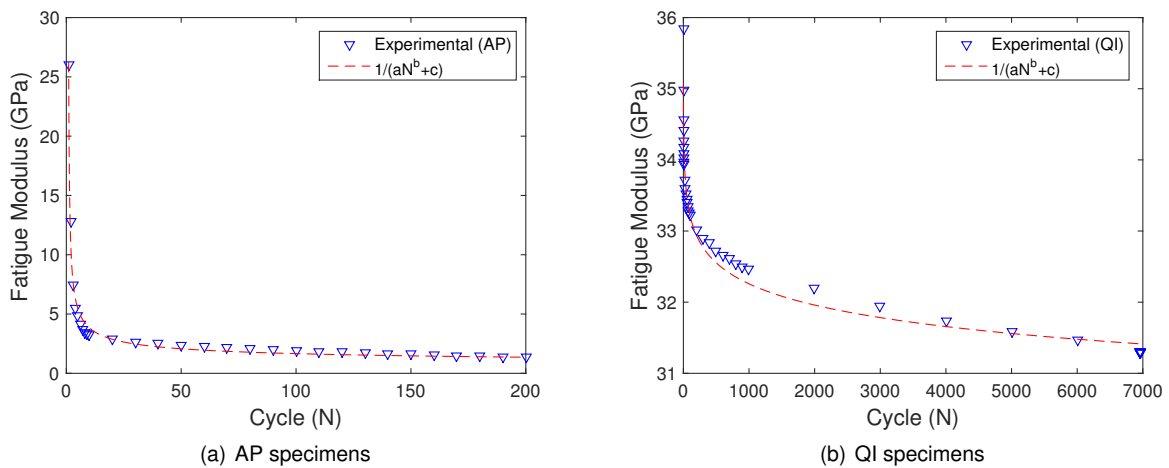


Figure 5.25: Fatigue modulus evolution with cycles.

Motivated by the lack of adequate methods to quantify entropy on a viscoelastic-viscoplastic material, an extensive theoretical formulation was derived in Section 2.4 so that every term in the dissipation inequality is considered. By proposing a new constitutive law based on the Helmholtz free energy, both viscous, thermal, damage and hardening phenomena can be modeled to yield an accurate representation of the material's behavior. Further investigation and experimental campaigns are needed to obtain the constitutive constants for a chosen material, extending beyond the scope of this thesis.

# Chapter 6

## Conclusions

The present thesis aimed to study the entropy generation and fracture fatigue entropy for a thermo-plastic matrix composite under different loading conditions and configurations. The main achievements and conclusions are stated in the following paragraphs.

### 6.1 Achievements

Regarding the experimental stage of this thesis, the difficulties encountered on the data acquisition stage motivated the development of a low-cost DIC system. Full-field sub-cycle strain measurements in high-frequency testing of specimens undergoing large deformations were successfully obtained for the first time with a non scientific-graded system.

By performing tests under different loading conditions, it was possible to observe that frequency had a detrimental effect on fatigue life in a matrix-dominated configuration. Autogenous heating phenomena and sharp temperature rises up to the glass transition temperature were verified, which is in accordance with related literature on thermoplastics. On the other hand, for fiber-dominated QI specimens, frequency proved to have a beneficial effect in the fatigue life, with a negligible temperature rise, which was also inferred in works dealing with other PMCs. The present thesis contributes to the literature by providing a description of the fatigue behavior of PEKK under different loading conditions and configurations, since the amount of works dealing with PEKK in this regard is still limited.

This thesis followed a similar approach to the one proposed in the original works to determine entropy from experimental data. However, a constant value of FFE was not verified for thermoplastic composites, as it was observed for other materials. Also, a detailed study on the effects of the loading conditions on the generated and accumulated entropy was provided, suggesting that the accentuated material's rate-dependence affects entropy generation to a great extent.

Finally, a discussion on the possible causes for a non-constant FFE with the used approach was presented. Attempts to remove non-damaging phenomena from the entropy generation were made, in line with existing works for metals. Such proved to be insufficient to obtain unified FFE values in composite materials, precluding the implementation of entropy as a failure criterion and a fatigue life

prediction method for thermoplastics. Motivated by the lack of entropy formulations that account with other dissipative terms other than mechanical work and heat transfer, a constitutive law based on the Helmholtz free energy that accounts for viscous, hardening and damage parameters was proposed to serve as a starting point in future work.

## 6.2 Future Work

While the evidence shows that the FFE concept might not be applicable to thermoplastics due to their rate-dependent behavior, the ability to obtain a universally constant value is not discarded. There is still room for improvement in the approach used for calculating entropy, for which a set of ideas is given:

- **Calculation of FFE using the remaining terms in the dissipation inequality** by means of the developed constitutive law. This includes performing material characterization tests to obtain the necessary properties to define the constitutive law;
- **Development of a cyclic plasticity model** that accounts for viscosity to calculate the plastic work term instead of using the experimental hysteresis energy. Such would be particularly useful if the implementation of fatigue failure criteria in computational simulations is intended;
- **Implementation of a damage parameter** that accurately reflects the damage evolution in the material during fatigue. The damage evolution law could be based on the degradation of fatigue modulus according to the inverse power law formulation proposed in Section 5.3. Alternatively, non-destructive testing techniques such as acoustic emission could be considered in future experimental campaigns to monitor the real time damage generation at the cost of additional equipment setup complexity and data post-processing.
- **Reformulation of the constitutive law for large deformations** and recalculation of FFE using the balance laws with the finite strain approach. Given that the magnitude of the viscoelastic deformations can be considered negligible with respect to the viscoplastic deformations, a hypoelastic constitutive law might need to be formulated;
- **Validation of the methodology for additional test cases**, such as a wider range of frequencies and stress levels, and different stacking sequences. An idea could be testing UD specimens and other off-axis configurations to quantify and compare the contribution of the matrix in the general fatigue behavior and entropy generation.



# Bibliography

- [1] K. Chawla. *Composite materials: science and engineering*. Springer Science & Business Media, 3rd edition, 2012. ISBN 978-0-387-74365-3.
- [2] P. Irving and C. Soutis(Eds.). *Polymer composites in the aerospace industry*. Woodhead Publishing, 2nd edition, 2020. ISBN 978-0-08-102679-3.
- [3] E. B. Harris. *Fatigue in composites: science and technology of the fatigue response of fibre-reinforced plastics*. Woodhead Publishing, 2003. ISBN 0-203-48371-5.
- [4] G. Gardiner. Thermoplastic composites gain leading edge on the A380: breakthrough manufacturing process produces lightweight, affordable glass-reinforced PPS J-nose on the worlds largest commercial aircraft wing. *High Performance Composites*, 14(2):50, 2006.
- [5] J. VanIngen, A. Buitenhuis, M. vanWijngaarden, and F. Simmons. Development of the Gulfstream G650 induction welded thermoplastic elevators and rudder. In *Proceedings of the international SAMPE symposium and exhibition, Seattle, WA, USA*, 2010.
- [6] The next generation multifunctional fuselage demonstrator — leveraging thermoplastics for cleaner skies. [www.cleansky.eu/the-next-generation-multifunctional-fuselage-demonstrator-leveraging-thermoplastics-for-cleaner](http://www.cleansky.eu/the-next-generation-multifunctional-fuselage-demonstrator-leveraging-thermoplastics-for-cleaner). (accessed on May 26th 2022).
- [7] T. Siddiqui. *Aircraft materials and analysis*. McGraw-Hill Education, 2015. ISBN978-0-071-83113-0.
- [8] E. A.P. Vassilopoulos. *Fatigue life prediction of composites and composite structures*. Woodhead Publishing, 2nd edition, 2020. ISBN 978-0-08-102575-8.
- [9] C. Saff. Effect of load frequency and lay-up on fatigue life of composites. *Long-Term Behavior of Composites. ASTM International*, 1983.
- [10] D. Curtis, D. Moore, B. Slater, and N. Zahlan. Fatigue testing of multi-angle laminates of CF/PEEK. *Composites Evaluation*, pages 40–50, 1987. Butterworth-Heinemann.
- [11] C. Lee and M. Jen. Fatigue response and modelling of variable stress amplitude and frequency in AS-4/PEEK composite laminates, Part 1: Experiments. *Journal of Composite Materials*, 34(11): 906–929, 2000.

- [12] E. Gamstedt and L. Berglund. Fatigue of thermoplastic composites. In *Fatigue in composites*, pages 359–387. Woodhead Publishing, 2003.
- [13] P. Curtis. Tensile fatigue mechanisms in unidirectional polymer matrix composite materials. *International Journal of Fatigue*, 13(5):377–382, 1991.
- [14] E. Gamstedt and R. Talreja. Fatigue damage mechanisms in unidirectional carbon-fibre-reinforced plastics. *Journal of Material Science*, 34(11):2535–2546, 1999.
- [15] K. L. Reifsnider, W. W. Stinchcomb, and T. K. O'Brien. Frequency effects on a stiffness-based fatigue failure criterion in flawed composite specimens. *Fatigue of Filamentary Composite Materials, ASTM STP 636*, pages 171–184, 1977. K. L. Reifsnider and K. N. Lauraitis, Eds., American Society for Testing and Materials.
- [16] C. Sun and W. S. Chan. Frequency effect on the fatigue life of a laminated composite. *Composite Materials: Testing and Design (Fifth Conference), ASTMSTP 674*, pages 418–430, 1979. S. W. Tsai, Ed., American Society for Testing and Materials.
- [17] S. Lin, C. Ma, N. Tai, S. Wu, J. Wu, and J. Lin. Effect of frequency on the fatigue behavior of [+/-45]<sub>4s</sub> laminate of carbon fiber reinforced polyetheretherketone (PEEK) composites under tension-tension loading. *Journal of Polymer Research*, 2(3):171–178, 1995.
- [18] M. Eftekhari and A. Fatemi. On the strengthening effect of increasing cycling frequency on fatigue behavior of some polymers and their composites: Experiments and modeling. *International Journal of Fatigue*, 87:153–166, 2016.
- [19] B. Vieille, W. Albouy, and L. Taleb. About the creep-fatigue interaction on the fatigue behaviour of off-axis woven-ply thermoplastic laminates at temperatures higher than T<sub>g</sub>. *Composites Part B: Engineering*, 58:478–486, 2014.
- [20] Z. Hashin and A. Rotem. A fatigue failure criterion for fiber reinforced materials. *Journal of Composite Materials*, 7(4):448–464, 1973.
- [21] M. Shokrieh and F. Taheri-Behrooz. A unified fatigue life model based on energy method. *Composite Structures*, 75(1–4):444–450, 2006.
- [22] M. Naderi, M. Amiri, and M. Khonsari. On the thermodynamic entropy of fatigue fracture. *Proceedings of the Royal Society A: Mathematical, Physical and Engineering Sciences*, 466(2114): 423–438, 2010.
- [23] M. Naderi and M. Khonsari. A comprehensive fatigue failure criterion based on thermodynamic approach. *Journal of Composite Materials*, 46(4):437–447, 2012.
- [24] M. Naderi and M. Khonsari. Thermodynamic analysis of fatigue failure in a composite laminate. *Mechanics of Materials*, 46:113–122, 2012.

- [25] M. Liakat and M. Khonsari. On the anelasticity and fatigue fracture entropy in high-cycle metal fatigue. *Materials & Design*, 82:18–27, 2015.
- [26] J. Jang and M. Khonsari. On the evaluation of fracture fatigue entropy. *Theoretical and Applied Fracture Mechanics*, 96:351–361, 2018.
- [27] A. Nourian-Avval and M. Khonsari. Rapid prediction of fatigue life based on thermodynamic entropy generation. *International Journal of Fatigue*, 145:106105, 2021.
- [28] M. Mehdizadeh, A. Haghshenas, and M. Khonsari. On the effect of internal friction on torsional and axial cyclic loading. *International Journal of Fatigue*, 145:106113, 2021.
- [29] J. Huang, C. Li, and W. Liu. Investigation of internal friction and fracture fatigue entropy of CFRP laminates with various stacking sequences subjected to fatigue loading. *Thin-Walled Structures*, 155:106978, 2020.
- [30] E. K. Gamstedt, O. Redon, and P. Brøndsted. Fatigue dissipation and failure in unidirectional and angle-ply glass fibre/carbon fibre hybrid laminates. *Key Engineering Materials*, 221:35–48, 2002. Trans Tech Publications Ltd.
- [31] M. Naderi and M. Khonsari. On the role of damage energy in the fatigue degradation characterization of a composite laminate. *Composites Part B: Engineering*, 45(1):528–537, 2013.
- [32] B. Mohammadi and A. Mahmoudi. Developing a new model to predict the fatigue life of cross-ply laminates using coupled CDM-entropy generation approach. *Theoretical and Applied Fracture Mechanics*, 95:18–27, 2018.
- [33] B. Mohammadi, B. Fazlali, and D. Salimi-Majd. Development of a continuum damage model for fatigue life prediction of laminated composites. *Composite Part A: Applied Science and Manufacturing*, 93:163–176, 2017.
- [34] M. Naderi and M. Khonsari. Real-time fatigue life monitoring based on thermodynamic entropy. *Structural Health Monitoring*, 10(2):189–197, 2011.
- [35] H. L. Lee. Elastic-plastic deformation at finite strains. *Journal of Applied Mechanics*, 36(1):1–6, 1969.
- [36] H. L. Lee. Some comments on elastic-plastic analysis. *Journal of Solids and Structures*, 17(9):859–872, 1981.
- [37] B. D. Coleman. Thermodynamics of materials with memory. *Archive for Rational Mechanics and Analysis*, 17(1):1–46, 1964.
- [38] *Toray Cetex TC1320 Product Data Sheet*. Toray Advanced Composites, 2019.
- [39] *ISO 22007-2 - Plastics - Determination of thermal conductivity and thermal diffusivity - Part 2: Transient plane heat source (hot disc) method*. International Organization for Standardization, 2008.

- [40] M. Villière, D. Lecoite, V. Sobotka, N. Boyard, and D. Delaunay. Real-time fatigue life monitoring based on thermodynamic entropy. *Composites Part A: Applied Science and Manufacturing*, 46: 60–68, 2013.
- [41] R. Marques. Remaining useful life prediction of laminated composite materials using thermoelastic stress analysis. Master's thesis, Instituto Superior Técnico, 2017.
- [42] *User's manual FLIR X6580sc series*. FLIR.
- [43] E. S. Lee and R. N. Forthofer. *Analyzing complex survey data*. Sage Publications, 2nd edition, 2006. ISBN 0-7619-3038-8.
- [44] *ASTM D3039/D3039M - Standard Test Method for Tensile Properties of Polymer Matrix Composite Materials*. ASTM International, .
- [45] *ASTM D3479/D3479M, Standard Test Method for Tension-Tension Fatigue of Polymer Matrix Composite Materials*. ASTM International, .
- [46] I. DeBaere, W. VanPaepegem, M. Quaresimin, and J. Degrieck. On the tension–tension fatigue behaviour of a carbon reinforced thermoplastic part I: Limitations of the ASTM D3039/D3479 standard. *Polymer Testing*, 30(6):625–632, 2011.
- [47] *ASTM D638 - Standard Test Method for Tensile Properties of Plastics*. ASTM International, .
- [48] I. A. Al-Hmouz. The effect of loading frequency and loading level on the fatigue behavior of angle-ply carbon/peek thermoplastic composites. Master's thesis, Concordia University, 1997.
- [49] M. Sutton, J. Orteu, and H. Schreier. *Image correlation for shape, motion and deformation measurements: basic concepts, theory and applications*. Springer Science & Business Media, 2009. ISBN 978-0-387-78747-3.
- [50] N. W. Gardner, M. W. Hilburger, W. T. Haynie, M. C. Lindell, and W. A. Waters. Digital image correlation data processing and analysis techniques to enhance test data assessment and improve structural simulations. In *AIAA/ASCE/AHS/ASC Structures, Structural Dynamics, and Materials Conference*, 2018.
- [51] J. Sirohi and M. Lawson. Measurement of helicopter rotor blade deformation using digital image correlation. *Optical Engineering*, 51(4), 2012.
- [52] N. Wang, K. Ri, H. Liu, and X. Zhao. Structural displacement monitoring using smartphone camera and digital image correlation. *IEEE Sensors Journal*, 18(11):4664–4672, 2018.
- [53] A. A. C. Pereira and J. R. M. D'Almeida. Development of a low-cost digital image correlation system to evaluate the behavior of polymers at large deformation. *Chemical Engineering Transactions*, 74: 1081–1086, 2019.
- [54] J. Rupil, S. Roux, F. Hild, and L. Vincent. Fatigue microcrack detection with digital image correlation. *The Journal of Strain Analysis for Engineering Design*, 46(6):492–509, 2011.

- [55] E. M. C. Jones and M. A. Iadicola(Eds.). *A Good Practices Guide for Digital Image Correlation*. International Digital Image Correlation Society, 2018.
- [56] *GOM Correlate Professional V8 SR1 Manual Basic*. GOM mbH, 2015.
- [57] S. K. Paul. A critical review of experimental aspects in ratcheting fatigue: microstructure to specimen to component. *Journal of Materials Research and Technology*, 8(5):4894–4914, 2019.
- [58] M. Naderi. *Thermodynamic Approach to Fatigue Failure Analysis in Metals and Composite Materials*. PhD thesis, Louisiana State University, 2011.
- [59] M. S. Blanter, I. S. Golovin, H. Neuhäuser, and H. R. Sinning. *Internal Friction in Metallic Materials - A Handbook*. Springer Berlin Heidelberg, 2007. ISBN 978-3-540-68758-0.
- [60] A. S. Nowick and B. S. Berry. *Anelastic Relaxation in Crystalline Solids*. Academic Press, Inc., 1972. ISBN 978-0-12-522650-9.
- [61] R. DeBatist. 1.3 Non Linear Dissipative Mechanisms. In *Materials Science Forum*, volume 366, pages 74–94. Trans Tech Publications Ltd., 2001.
- [62] J. Morrow. Cyclic plastic strain energy and fatigue of metals. In *Internal friction, damping, and cyclic plasticity*. ASTM International, 1965.
- [63] W. Hwang and K. S. Han. Fatigue of composites — fatigue modulus concept and life prediction. *Journal of Composite Materials*, 20(2):154–165, 1986.

